Universität Bremen

Analysis of the chaperone-mediated remodeling of the amyloid protein Huntingtin

Dissertation zur Erlangung des akademischen Grades des Doctor rerum naturalium (Dr. rer. nat.)

eingereicht im Fachbereich 02 Biologie/Chemie

der Universität Bremen

vorgelegt von

Yasmin Richter

September 2023

Examiners:

1. Examiner: Prof. Dr. Janine Kirstein
2. Examiner: Prof. Dr. Olivia Masseck
3. Examiner: Prof. Dr. Mark Hipp

Examination Committee:

Chairperson: Prof. Dr Barbara Reinhold-Hurek

Co-Examiners: Prof. Dr. Janine Kirstein
Prof. Dr. Olivia Masseck
Dr. Christian Arend

Other non-voting members: Regina Nahrstedt
Gurleen Kaur Kalsi

The thesis defense colloquium took place at the 02. November 2023 at the University of Bremen.

Table of Contents

0. Summary

Huntington´s disease (HD) is a neurodegenerative disease that is autosomal-dominant inherited. HD is a polyglutamine (polyQ) disease, which is caused by an expanded CAG trinucleotide repeat in the huntingtin gene that results in an expanded polyglutamine stretch in the huntingtin protein (HTT). Aberrant splicing and proteolytic cleavage lead to N-terminal fragments including the first Exon of the protein. Those N-terminal fragments with an elongated polyQ stretch were shown to spontaneously self-assemble into insoluble amyloid aggregates resulting in motor, cognitive and behavioral impairments.

How the amyloid formation is affected by molecular chaperones was addressed in this thesis. A trimeric chaperone complex consisting of DNAJB1, Hsc70 and Apg2 was previously found to suppress huntingtin exon1 aggregation and disaggregate preformed HTT fibrils in an ATP dependent manner. Here the binding mechanism between HTT Exon1 (HTTEx1) and DNAJB1 was investigated revealing the necessity of hydrogen bond formations stabilizing the DNAJB1/HTTEx1 binding.

As DNAJB1 was found to be the rate limiting factor in the modulation of Huntingtin aggregation by the trimeric chaperone complex *in vitro,* here the overexpression of the J-protein on the aggregation propensity of HTTEx1 *in vivo* was investigated. Overexpression of DNJ-13 (the *C. elegans* ortholog of DNAJB1) in a Huntington´s disease *C. elegans* strain was resulting in an increased aggregate formation of HTTEx1 in the nematodes. When the binding site for the DNJ-13 was deleted from HTTEx1 the aggregation propensity did not change significantly upon overexpression of DNJ-13. Indicating that in a multicellular organism with distinct tissues additional factors play a role.

Moreover, the effect of DNAJB1 and Hsc70 on the formation of liquid condensates and subsequent liquid-to-solid phase transition of HTTEx1 was investigated. While DNAJB1 and Hsc70 could suppress liquid-to-solid phase transition of HTTEx1 this effect was not observed when the binding site for DNAJB1 was deleted from HTTEx1.

0.1 Zusammenfassung

Die Huntington-Krankheit ist eine neurodegenerative Erkrankung, die autosomal-dominant vererbt wird. Sie ist eine Polyglutamin-(PolyQ)-Krankheit, die durch eine verlängerte CAG-Trinukleotid-Wiederholung im Huntingtin-Gen verursacht wird, welche auf Proteinebene zu einem verlängertem Polyglutamin-Stretch führt. Durch alternatives Spleißen und proteolytische Spaltung entstehen N-terminale Fragmente, welche das erste Exon des Proteins enthalten. Es wurde gezeigt, dass diese N-terminalen Fragmente mit einem verlängerten PolyQ-Stretch spontan aggregieren und Amyloid-Fibrillen bilden, was zu motorischen und kognitiven Einschränkungen führt.

In dieser Arbeit wurde untersucht, wie die Amyloidbildung durch molekulare Chaperone beeinflusst wird. Es wurde bereits gezeigt, dass ein trimerer Chaperonkomplex bestehend aus DNAJB1, Hsc70 und Apg2 die Aggregation von Huntingtin-Exon1 (HTTEx1) verlangsamt und HTT-Fibrillen wieder disaggregieren kann. Hier wurde nun die Bindungsstelle zwischen HTTEx1 und DNAJB1 untersucht und dabei die Notwendigkeit der Bildung von Wasserstoffbrückenbindungen zur Stabilisierung der DNAJB1/HTTEx1-Bindung festgestellt.

Da gezeigt werden konnte, dass DNAJB1 *in vitro* der geschwindigkeitsbestimmende Faktor bei der Modulation der Huntingtin-Aggregation durch den trimeren Chaperonkomplex ist, wurde hier der Effekt der Überexpression des J-Proteins auf die Aggregation von HTTEx1 *in vivo* untersucht. In einem Huntington-Krankheits Modell in *C. elegans* führte die Überexpression von DNJ-13 (dem *C. elegans*-Ortholog von DNAJB1) zu einer erhöhten Aggregation von HTTEx1. Wenn die Bindungsstelle für DNJ-13 in HTTEx1 nicht vorhanden war, änderte sich die Aggregationsneigung bei Überexpression von DNJ-13 nicht signifikant. Dies weist darauf hin, dass in einem mehrzelligen Organismus mit unterschiedlichen Geweben zusätzliche Faktoren eine Rolle spielen.

Darüber hinaus wurde die Wirkung von DNAJB1 und Hsc70 auf die Bildung flüssiger Kondensate von HTTEx1 und deren anschließenden Phasenübergang von flüssig zu fest untersucht. Während DNAJB1 und Hsc70 den Phasenübergang von HTTEx1 von flüssig zu fest unterdrücken konnten, wurde dieser Effekt nicht beobachtet, als die Bindungsstelle für DNAJB1 nicht vorhanden war.

1. Disclaimer

I. The here presented work was done under the supervision of Prof. Dr. Janine Kirstein in her working group at the University of Bremen. Parts of my work were done in collaboration with other PhD students of my working group or other collaboration partners at the university. Experiments were colleagues of mine contributed are marked in the results section and are mentioned here. Including those results in this thesis is necessary as they are required to understand the context of the pursued experiments.

Merve Özel (Kirstein lab) performed the ATPase and luciferase assays for the DNAJB1^{H32Q} and DNAJB1$^{H32Q\text{-}H244A}$ mutations and the luciferase assays for DNAJB1^{H244Q}. Additionally we generated the plasmid for the DNAJB1$^{H32Q\text{-}H244A}$ mutant together.

I.L. Grothaus, S. Köppen and L. Colombi Ciacchi (University of Bremen) performed the *in silico* analysis regarding the HTTEx1/DNAJB1 interaction.

Franziska Hirsch (Kirstein lab) provided the FLIM data for the mScarlet control of the 7 days old nematodes.

II. Furthermore, I would like to mention the students that contributed to certain experiments or projects and were supervised by me in the lab.

Mohamed ElBediwi was performing the experiments with the DNAJB1^{H244F} mutant during his master thesis.

Irina Barac worked with me on the fecundity assays during her lab rotation/internship.

Gregor Langemeier established the turbidity assay with me during his lab rotation/internship.

2. Introduction

Protein aggregates are a hallmark of neurodegenerative diseases like Alzheimer´s disease, Amyotrophic lateral sclerosis, Parkinson´s (Nussbaum and Ellis, 2003; Ross and Poirier, 2004) and Huntington´s disease (Scherzinger *et al.*, 1999). Compared to many other neurodegenerative diseases, Huntington´s disease is a monogenic disease and is fully penetrant, which makes it a good model neurodegenerative disorder to study (Ross and Poirier, 2004).

2.1 Huntington´s disease

Huntington´s disease (HD) is a neurodegenerative disease that is autosomal-dominant inherited and initially leads to neuronal death in the striatum, causing motor, cognitive and psychiatric impairments (Walker, 2007; Roos, 2010; Ross and Tabrizi, 2011). HD was clinically first described in 1872 by George Huntington (George Huntington, 1872; Vale and Cardoso, 2015). The incidence of HD varied in different epidemiological studies between 0.42 to 17.2 cases per 100,000 (Kay, Hayden and Leavitt, 2017; Harding and Tong, 2018). As a neurodegenerative disease, HD is a late onset disease with a mean onset between the age of 30 to 50 years (Roos, 2010). In rare cases also early/juvenile onsets can be observed with the earliest onset being described for a patient at the age of 2 to very late onsets at the age of 85. HD is a polyglutamine (polyQ) disease, which is caused by an expanded CAG trinucleotide repeat in the Huntingtin gene (Macdonald, 1993). Extension of this CAG repeat of ≥36 results in HD whereas CAG repeats ≤35 do not. Upon a polyQ stretch of over 40 glutamines it is considered to be highly penetrant (Bates *et al.*, 2015). The length of the polyglutamine stretch correlates with the onset of the disease, so that longer repeats cause earlier onset and also an increased rate of pathogenesis (Andresen *et al.*, 2007; Lee *et al.*, 2012). The elongated polyQ stretch at the N-terminus of Huntingtin (HTT) results in a toxic gain of function (Taylor, Hardy and Fischbeck, 2002) and leads to cytotoxicity and a number of biochemical dysfunctions. It was shown to impair the proteostasis network in cell culture experiments (Kim *et al.*, 1999) by dysregulating

transcription factors (Seredenina and Luthi-Carter, 2012), inducing mitochondrial toxicity (Reddy and Shirendeb, 2012; Johri, Chandra and Flint Beal, 2013) and causing cellular energy imbalance (Ju, Lin and Chern, 2012). Furthermore it can be linked to synaptic dysfunction (Nithianantharajah and Hannan, 2013) and axonal transport impairment (Reddy and Shirendeb, 2012). These are all hallmarks of neurodegenerative diseases (Wilson *et al.*, 2023) (Fig. 2.1).

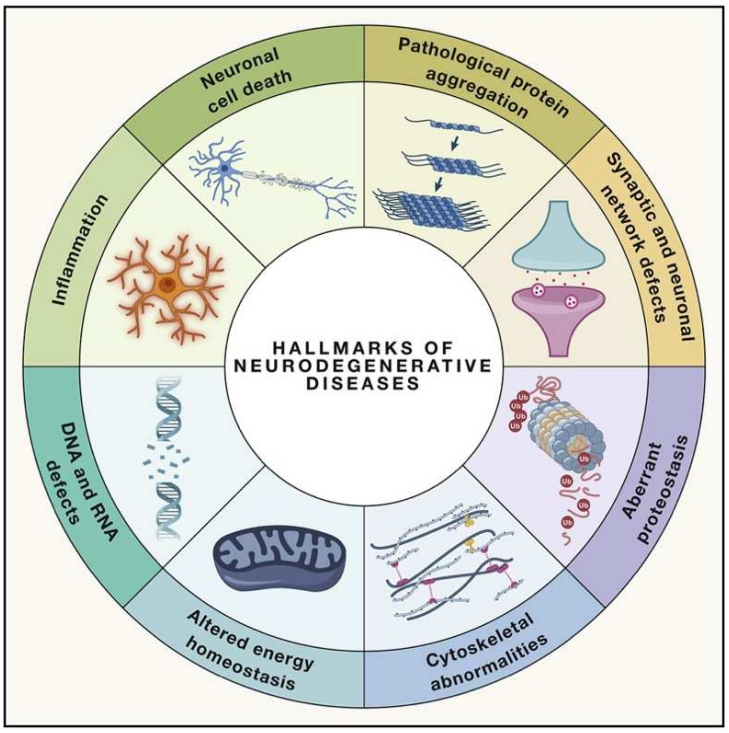

Figure 2.1: Hallmarks of neurodegenerative diseases

Illustration of the eight hallmarks of neurodegenerative diseases: pathological protein aggregation, synaptic and neuronal network dysfunction, aberrant proteostasis, cytoskeletal abnormalities, altered energy homeostasis, DNA and RNA defects, inflammation, and neuronal cell death (Figure from Wilson *et al.*, 2023).

2.1.1 Huntingtin protein (HTT)

The *HTT* gene contains 67 exons and is translated into the HTT protein. It is ubiquitously expressed in all body tissues but the highest expression levels were found in the neurons of the central nervous system (Bhide *et al.*, 1996; Marques Sousa and Humbert, 2013). It is located mainly in the cytoplasm of cells and to a lesser extend also in the nucleus (Saudou and Humbert, 2016). Full length HTT is a large protein with 3144 amino acids and a molecular weight of approximately 350 kDa. The physiological role of HTT is not fully understood yet, but it has been shown to be essential in embryogenesis and central nervous system development (Duyao *et al.*, 1995; Nasir *et al.*, 1995; Dragatsis, Levine and Zeitlin, 2000; McKinstry *et al.*, 2014; Liu and Zeitlin, 2017) including axonal transport (Cattaneo, Zuccato and Tartari, 2005; Vitet, Brandt and Saudou, 2020).

Besides the full length HTT, there are different isoforms that are generated by alternative splicing, including one isoform only containing HTTExon1 (HTTEx1) (Gipson *et al.*, 2013; Sathasivam *et al.*, 2013; Hughes *et al.*, 2014; Ruzo *et al.*, 2015; Neueder *et al.*, 2017; Krach *et al.*, 2022).

The full length HTT is predicted to contain 36 HEAT and HEAT-like repeats distributed over the whole protein that are interspaced by several disordered regions (Palidwor *et al.*, 2009; Guo *et al.*, 2018). HTT is cleaved by multiple proteases on cleaving sites called PEST (proline (P); aspartic acid (E) or glutamic acid (D); serine (S); threonine (T)) domains which are located in the disordered regions of HTT (Zuccato, Valenza and Cattaneo, 2010; Saudou and Humbert, 2016). Proteolytic processing of HTT containing a physiological length of the polyQ stretch is discussed to modify its cellular functions (Goldberg *et al.*, 1996; El-Daher *et al.*, 2015). An elongated polyQ stretch (mHTT) increases the proteolytic processing, resulting in higher levels of toxic N-terminal fragments of mHTT (Li *et al.*, 2000; Zhou *et al.*, 2003; Ratovitski *et al.*, 2007). So, both splicing and proteolytic cleavage can result in N-terminal fragments of mHTT.

2.1.2 Huntingtin Exon1

While the structure of HTT could be solved by cryo-electron microscopy, it did not include the first exon, since it is extremely flexible (Guo *et al.*, 2018). The first N-terminal exon of HTT consists of three distinguishable regions. At the N-terminus there are 17 amino acids, which are defined as the N17 region followed by the polyQ stretch and the proline rich domain (PRD) which contains two proline stretches of 11 and 10 subsequent prolines with a proline rich sequence in between (Fig.2.2).

As HTTEx1 contains the elongated disease causing polyQ stretch, its structure was extensively studied, but no defined conformation was obtained so far. The N17 region was found to form an amphipathic α-helix, which is physiologically important for membrane interactions and as a nuclear export signal (Atwal *et al.*, 2007; Kim *et al.*, 2009; Maiuri *et al.*, 2013). In non-fibrillized HTTEx1, the polyQ stretch is highly flexible and can adopt different structures (Miller, Rutenber and Muchowski, 2009; Giorgini, 2013). The proline rich domain also exhibits high flexibility, but can also form a relatively rigid poly-L-proline type II (PPII) helix (Darnell *et al.*, 2007, 2009; Miller, Rutenber and Muchowski, 2009).

Figure 2.2: Schematic representation of HTTEx1

Schematic representation of HTTEx1 showing the N17 region consisting of the first 17 amino acids of the N-terminus with the adjacent PolyQ stretch and the proline rich domain (PRD) with the first proline stretch (P11) and the second proline stretch (P10).

2.1.3 Aggregation mechanisms of HTTEx1

As described earlier, N-terminal fragments of HTT are generated by aberrant splicing and proteolytic cleavage. Those N-terminal fragments with an elongated polyQ stretch

were shown to spontaneously self-assemble into insoluble amyloid aggregates (Scherzinger *et al.*, 1997, 1999; Rochet and Lansbury, 2000; Poirier *et al.*, 2002; Pieri *et al.*, 2012; Vieweg *et al.*, 2016). Amyloid aggregates are defined as highly stable fibrillar structures with cross-β-sheet formation (Sunde and Blake, 1997; Wagner *et al.*, 2018). This fibril formation is considered to be a multi-step process (Morris, Watzky and Finke, 2009).

The process of fibril assembly can be divided into two phases, the initial lag phase, in which little to no fibrils are formed and the fibril growth phase, where extensive fibril formation takes place (Cohen *et al.*, 2012; Gillam and MacPhee, 2013).

The lag phase is considered to be caused by the slow and rate limiting process of primary nucleation (Fig. 2.3), where interacting monomers are thought to form kinetically unstable oligomers, which then grow into larger stable ß-sheet structures (Ferrone, 1999). Here, the rate of aggregation depends on the protein concentration and the length of the polyQ stretch, so that primary nucleation is more likely to occur with longer polyQ stretches and at high concentrations (Kar *et al.*, 2011; Meisl *et al.*, 2016; Chen and Wolynes, 2017). In the fibril growth phase, secondary processes take place, which allow faster fibril formation. Secondary processes include secondary nucleation, where monomers are directly attached to existing fibrils (Cohen *et al.*, 2012, 2013), fragmentation (Xue, Homans and Radford, 2008; Knowles *et al.*, 2009) and fibril branching (Andersen *et al.*, 2009).

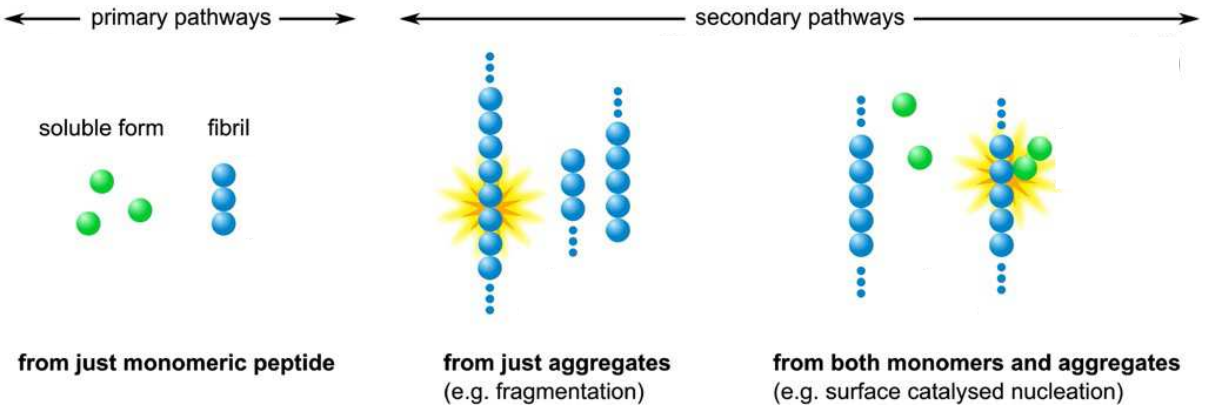

Figure 2.3: Mechanisms of protein aggregation

Left, primary nucleation pathway, aggregates derive from soluble monomers. Middle, secondary process of monomer independent aggregation by fragmentation. Right, secondary pathway of monomer dependent secondary nucleation (Figure adapted from Cohen *et al.*, 2012)

For HTTEx1, it has been shown that the aggregation mechanism involves primary nucleation as well as secondary pathways with formation of non-fibrillar and fibrillar oligomers and subsequent formation of large fibrils (Poirier *et al.*, 2002; Dahlgren *et al.*, 2005; Thakur *et al.*, 2009; Vitalis and Pappu, 2011; Crick *et al.*, 2013; Duim *et al.*, 2014; Sahoo *et al.*, 2016). In addition to the monomer-dependent secondary pathway depicted in Fig.2.3, HTTEx1 was shown to form larger fibrils by nucleated fibril branching, where new branches grow at the surface of already existing fibrils that remain attached to the initial fibril, creating large fibril bundles (Wagner *et al.*, 2018).

The flanking regions of the polyQ stretch of HTTEx1 affect the aggregation. The N17 region is discussed to facilitate fibril formation by adopting an amphipathic α-helical structure bringing multiple HTTEx1 molecules together through coiled-coil interactions and thereby also bringing the polyQ stretches into close proximity (Thakur *et al.*, 2009; Jayaraman *et al.*, 2012; Zhang *et al.*, 2017). This would lead to enhanced interactions of the polyQ regions facilitating β-sheet formation and subsequent fibril formation (Wetzel, 2012; Kokona, Rosenthal and Fairman, 2014; Kang *et al.*, 2017; Pandey *et al.*, 2018). The proline rich domain on the other hand is discussed to delay aggregation by adopting a poly-L-proline type II (PPII) helix, which structurally also affects the polyQ stretch and thereby inhibits β-sheet formation and subsequent fibril formation (Bhattacharyya *et al.*, 2006; Darnell *et al.*, 2007, 2009; Isas, Langen and Siemer, 2015). In line with this, the proline rich domain has been shown to be protective and decrease fibril formation in yeast and *C. elegans* (Dehay and Bertolotti, 2006; Duennwald *et al.*, 2006; Pigazzini *et al.*, 2021).

A special case of aggregation that is discussed to facilitate fibril formation is liquid-liquid phase separation (LLPS) and subsequent liquid-to-solid phase transition. For proteins, to undergo LLPS, the protein-protein interaction has to be energetically favored over the protein-water/solvent interaction. Structural factors that favor LLPS are intrinsically disordered regions and low complexity domains, where specific amino

acids are overrepresented (Harmon *et al.*, 2017; Martin and Mittag, 2018; Alberti, Gladfelter and Mittag, 2019). A high number of interaction partners can also promote LLPS properties since proteins with many interaction partners tend to assemble into larger oligomers or polymers, which lowers their solubility and thereby facilitating phase separation (Banani *et al.*, 2017). These “risk factors” are structural properties of many proteins associated with neurodegenerative diseases and over the last years, multiple of them have been shown to undergo LLPS. For example, FUS, tau, alpha-synuclein and also HTT (Patel *et al.*, 2015; Peskett *et al.*, 2018; Kanaan *et al.*, 2020; Ray *et al.*, 2020). For HTTEx1 LLPS and subsequent liquid-to-solid phase transition has been observed *in vitro* and HEK cells (Peskett *et al.*, 2018).

In Huntington´s disease LLPS of HTTEx1 could lead to increased rates of nucleation and subsequent fibril formation. How the polyQ flanking regions effect this process is not clear yet.

2.2 Proteostasis network

A functional proteome is crucial for the maintenance of physiological cellular functions. Proteins have to be correctly folded and protein levels have to be tightly regulated. This balanced state of the proteome is defined as proteostasis (Balch *et al.*, 2008; Hipp, Kasturi and Hartl, 2019).

Proteins are synthesized at the ribosome and have to fold into their unique three-dimensional structure to be biological functional (Balchin, Hayer-Hartl and Hartl, 2016). Although the specific protein folding is determined by the amino acid sequence (Anfinsen, 1973) and small proteins up to 100 amino acids can fold into their native conformation spontaneously *in vitro*, larger proteins require molecular chaperones to adopt their native state. *In vivo,* molecular crowding further impedes correct folding as the high protein concentration of 300 to 400 mg/ml in the cytosol leads to an increased tendency of intermediates to misfold and subsequently aggregate (Ellis, 2006; Kim *et al.*, 2013). In mammalian cells, over 2000 proteins are associated with the proteostasis network (Klaips, Jayaraj and Hartl, 2018). The proteostasis network is assisting in *de novo* folding of the nascent chain, takes part in protein refolding and disaggregation as well as proteolytic clearance via e.g. autophagy and the ubiquitin-proteasome system, thereby maintaining a balanced protein homeostasis (Wolff, Weissman and Dillin, 2014; Kaushik and Cuervo, 2015).

The proteostasis network has been shown to decline in an age-dependent manner resulting in age-related cellular dysfunctions and degenerative diseases (Min *et al.*, 2008; Rubinsztein, Mariño and Kroemer, 2011; Taylor and Dillin, 2011; Labbadia and Richard I Morimoto, 2015; Klaips, Jayaraj and Hartl, 2018; Hipp, Kasturi and Hartl, 2019). The neurons as post-mitotic and long-lived cells are especially vulnerable for an accumulation of misfolded proteins (Sala, Bott and Morimoto, 2017). Additionally, the expression level of inducible ATP-dependent chaperones is declining with aging in human neurons, which further promotes aggregation (Brehme *et al.*, 2014). Once a certain threshold is reached, aggregation-prone proteins can be no-longer kept soluble, leading to pathological protein aggregation and further aberrant proteostasis creating a positive feedback loop (Hipp *et al.*, 2012; Hipp, Park and Hartl, 2014).

2.2.1 Molecular chaperones

Molecular chaperones were first described in the context of heat shock response and hence termed heat-shock proteins, which then were further categorized by their molecular weight into different families. The small heat shock proteins, which are ATP-independent with a molecular weight of 12 to 43 kDa, Hsp40/J-domain proteins, Hsp60/chaperonins, Hsp70, Hsp90, Hsp100 and Hsp110 (Hartl, 1996; Hartl, Bracher and Hayer-Hartl, 2011; Kim *et al.*, 2013; Balchin, Hayer-Hartl and Hartl, 2016). Heat shock proteins are not only expressed upon heat stress, but can be also constitutively expressed for example Hsc70, which is constitutively expressed under physiological conditions (Kim *et al.*, 2013). Hsp70s are universal chaperones and participate in several cellular processes, including *de novo* folding, suppression of aggregation and disaggregation. In combination with members of the Hsp40 family and Hsp100 family, namely Hsp104 in *Saccharomyces cerevisiae* and ClpB in *E. coli* they have been shown to effectively resolubilize aggregated proteins (Parsell *et al.*, 1994; Mogk, 1999). Hsp104 and ClpB as disaggregases belong to the triple ATPase complex protein family (AAA+), which also contains AAA+ proteases targeting disaggregation products to degradation (Kirstein *et al.*, 2009). Those Hsp100 chaperones are nonexistent in the cytosol of eucaryotic cells. Here, disaggregation is archived by a trimeric chaperone complex consisting of members of the Hsp70, J-domain protein and Hsp110 chaperone families (Shorter, 2011; Rampelt *et al.*, 2012). These chaperone complexes were shown to be able to suppress aggregation and disaggregate amorphous aggregates like luciferase as well as disease associated fibrillar protein aggregates of α-synuclein and mHTT (Rampelt *et al.*, 2012; Gao *et al.*, 2015; Nillegoda *et al.*, 2015; Kirstein *et al.*, 2017; Scior *et al.*, 2018).

2.2.2 The canonical model of Hsp70

Structurally, Hsp70s can be divided into two distinct domains, the N-terminal nucleotide binding domain (NBD) and a substrate binding domain (SBD), which are connected via a hydrophobic flexible linker region (Kumar *et al.*, 2011; Mayer, 2013). The NBD itself consists of four subdomains, which form two lobes, creating a cleft in-

between them. In this cleft, binding and hydrolysis of ATP takes place (Flaherty, DeLuca-Flaherty and McKay, 1990; Mayer and Gierasch, 2019). The SBD can be divided into two subdomains, the α-helical domain (SBDα) and the ß- sandwich domain (SBDß) with the SBDß binding to the substrate while the SBDα forms a lid (Mayer, 2013). Hsp70 recognizes and binds to a hydrophobic five amino acid motif with adjacent positively charged amino acids which becomes exposed in misfolded proteins (Fourie, Sambrook and Gething, 1994; Rüdiger, Buchberger and Bukau, 1997).

The canonical model is a multi-step model and depends on the ATPase activity of Hsp70. In the ATP-bound state, the SBDß and the SBDα are in close proximity, resulting in a highly dynamic substrate association and dissociation. This leads to an overall low affinity to the substrate. In addition, this conformational state also slows down the intrinsic ATPase activity of Hsp70 (Kityk *et al.*, 2015; Rosenzweig *et al.*, 2019). For that reason, a J-domain protein is required as co-chaperone.

J-domain proteins are considered to drive the specificity of the trimeric chaperone complex. In humans there are 49 members of the J-domain family (Hageman and Kampinga, 2009; Craig and Marszalek, 2017; Ayala Mariscal and Kirstein, 2021). J-domain proteins are defined by their name giving J-domain, which is highly conserved and consists of 70 amino acids and always contains a Histidine-Proline-Aspartate (HPD) motif that is essential for the acceleration of the ATP hydrolysis of Hsp70 (Tsai and Douglas, 1996; Greene, Maskos and Landry, 1998). Those J-domain proteins can be divided into three different classes, class A, B and C depending on the structural modules they contain. Class A J-domain proteins contain a N-terminal α-helical J-domain, a glycine-phenylalanine-rich (G/F-rich) region, a C-terminal domain formed by two β-barrel domains (CTDI and CTDII) and a dimerization domain (DD). In Class A J-domain proteins, the CTDI also contains a cysteine-rich region or zinc finger-like region (ZFLR). This is missing in Class B J-domain proteins. Class C type J-domain proteins are all remaining proteins, that contain a J-domain, but do not fall into class A or B (Nillegoda *et al.*, 2017; Ayala Mariscal and Kirstein, 2021).

In the canonical model, the J-domain proteins bind initially to the client protein and recruit Hsc70. The J-domain protein accelerates the ATP hydrolysis activity of Hsc70 and thereby induces a conformational change of Hsp70 from an open ATP-bound

conformation to a closed ADP-bound conformation keeping the substrate bound to Hsp70 (Laufen *et al.*, 1999; Kampinga and Craig, 2010). Substrate release is then mediated by nucleotide exchange factors (NEF) like Bcl-2 associated anthanogene (BAG) or Hsp110 (HSPA4/Apg2 in humans or HSP-110 in *C. elegans*), which are releasing ADP from Hsp70 allowing it to subsequently bind to ATP, changing to the open conformation and releasing the substrate (Laufen *et al.*, 1999; Raviol *et al.*, 2006; Rampelt *et al.*, 2012). After this, the substrate is either refolded into its native state or can re-enter the cycle (Fig. 4.2).

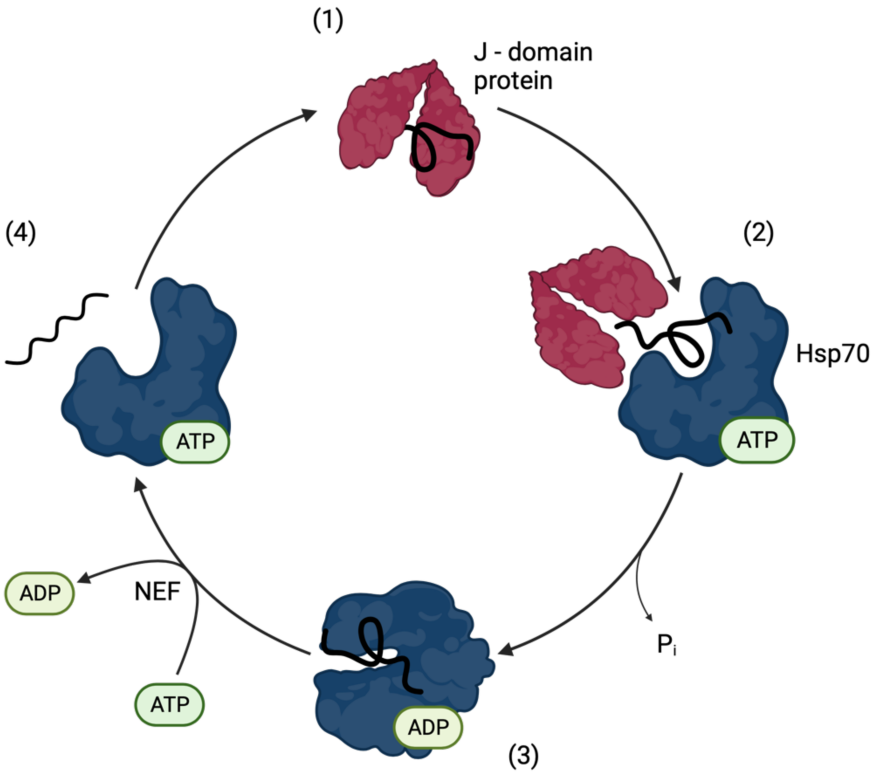

Figure 2.4: Allosteric protein refolding cycle of Hsc70 and its co-chaperones

The J-domain protein (red) binds to the the unfolded substrate (1), it recruits the unfolded substrate to Hsp70 (blue) (2) and induces ATP hydrolysis, which stabilizes the binding between Hsc70 and the unfolded protein (3). A nucleotide exchange factor (NEF) induces substitution of ADP with ATP, decreasing the substrate affinity of Hsc70, which results in substrate release (4). The released substrate is either refolded into its native state or re-enters the cycle.

2.2.3 The trimeric complex

A specific trimeric chaperone complex consisting of Hsc70 as member of the Hsp70 family, DNAJB1 as J-domain protein and Apg2 as nucleotide exchange factor was found to interact with multiple proteins involved in neurodegenerative diseases. The trimeric chaperone complex was shown to suppress Aβ aggregation and disassemble tau fibrils (both proteins are involved in the pathology of Alzheimer´s disease) (Nachman *et al.*, 2020; Ayala Mariscal *et al.*, 2022) while it was also able to disassemble preformed α-synuclein fibrils (a protein linked to Parkinson´s disease pathology) *in vitro* and reduce α-synuclein pathology *in vivo* by overexpression of the NEF (Gao *et al.*, 2015; Taguchi *et al.*, 2019). For HTTEx1, it was found that the trimeric chaperone complex was able to suppress aggregation as well as resolubilizing preformed fibrils. Fibril formation of HTTEx1 was followed by a FRET (Förster Resonance Energy Transfer) based aggregation assay, where FRET efficiency was increasing with the formation of fibrils while disaggregation was analyzed by filter retardation assays and TEM (Transmission Electron Microscopy). Notably, not only the human chaperones could suppress aggregation but also their *C. elegans* orthologues were able to suppress HTTEx1 aggregation and disaggregate preformed fibrils (Scior *et al.*, 2018).

Recently, the binding sites of DNAJB1 (and Hsc70) were mapped to the second poly proline stretch of the PRD in HTTEx1 by cross-linking mass spectrometry (Fig. 2.5) (Ayala Mariscal *et al.*, 2022) allowing further analysis of the binding mechanism.

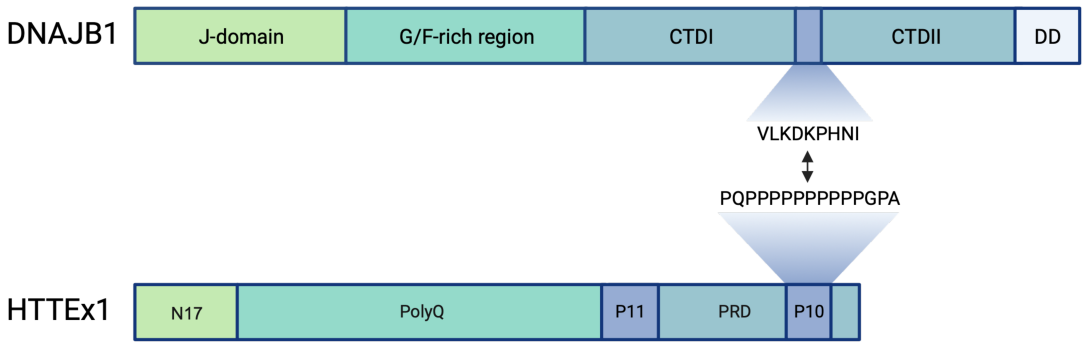

Figure 2.5: HTT binding site of DNAJB1

Schematic representation of the binding site between the CTD of DNAJB1 (residue 238 to 246) and second proline stretch of the PRD of HTTEx1 (residue 92 to 106) found by cross-linking mass spectrometry.

2.3 *C. elegans* as model organism for *in vivo* experiments

C. elegans was established as model organism in 1974 by S. Brenner (Brenner, 1974). It is a small nematode with a length of roughly 1 mm as an adult, which still contains distinct tissues like muscle, neurons, intestine, excretory system, gonads, glands, and a hypodermis (Sulston and Horvitz, 1977). This allows to study individual tissues and tissue interactions. The whole genome of *C. elegans* was sequenced in 1998 (The C. elegans Sequencing Consortium*, 1998). *C. elegans* contains six chromosomes with five autosomes and one gonosome as a hermaphrodite, while males contain only five chromosomes, missing the gonosome. The genome encodes for more than 19,000 genes. Only 0.1 % of the population are male under normal culture conditions, but the ability to generate males allows genetic crosses in *C. elegans* (Brenner, 1974).

In the lab, the nematodes can be kept on NGM-Agar plates and feed on *E. coli* making it an easy to maintain model system. Additionally, *C. elegans* has a short life cycle allowing to study aging on the time scale of a month. *C. elegans* has a high reproduction rate, as healthy nematodes can lay up to 300 eggs during their reproductive phase. After hatching from the egg, the nematodes are in their first larvae stage (L1) and go through three more larvae stages (L2, L3 and L4) before reaching adulthood after 3.5 days (at 20 °C). Upon starvation (or other stresses), L1 larvae can enter a into a dauer state and survive several months. Once the environmental conditions improve, the larvae develop into the L4 stage and further into adult animals (Byerly, Cassada and Russell, 1976; Altun, Z.F., 2023).

Approximately 80% of the nematode's proteome have a human ortholog (Lai *et al.*, 2000) and although the nematodes do not necessarily express orthologues of proteins linked to neurodegenerative diseases, they can still function as model organism as diseases often affect evolutionary conserved pathways (Sengupta and Samuel, 2009; Markaki and Tavernarakis, 2010).

C. elegans also can serve as a model organism for polyQ diseases. In nematodes expressing polyQ in muscle or neuronal cells, it has been shown that an increase of polyQ repetitions correlates with higher polyQ aggregation and toxicity (Faber *et al.*, 1999; Morley *et al.*, 2002). Recently, a new Huntington's disease *C. elegans* model

was established expressing sub-stoichiometrically fluorescently labelled HTTEx1 pan-neuronally under the control of the *rgef-1* promotor (Pigazzini *et al.*, 2021). The same *C. elegans* strains will be employed in this thesis.

2.4 Objectives

It was found that the trimeric chaperone complex consisting of Hsc70, DNAJB1 and Apg2 was able to suppress HTTEx1 aggregation and disaggregate preformed HTTEx1 fibrils, however the exact mechanism remained unclear (Scior *et al.*, 2018). Now, that the binding interface between DNAJB1 and HTTEx1 could be determined by cross-linking mass spectrometry, I pursued the following aims in my thesis:

I. Mechanistic characterization of the interaction between DNAJB1 and HTTEx1.

II. What is the role of the trimeric chaperone complex and in particular DNAJB1 on the LLPS properties of HTTEx1?

III. Analysis of the role of the homologous J-domain protein, DNJ-13, on HTTEx1 in the aging model system *C. elegans*.

3. Results

3.1 DNAJB1 - HTTEx1 interaction

It has been previously demonstrated that a trimeric chaperone complex consisting of Hsc70, Apg2 and DNAJB1 is able to suppress HTTEx1 aggregation and to even disaggregate HTTEx1Q_{48} fibrils. While DNAJB1 and Hsc70 were found to directly interact with HTTEx1Q_{48} fibrils, this could not be shown for Apg2 (Scior *et al.*, 2018), suggesting that Apg2 is recruited by Hsc70/DNAJB1 to HTTEx1Q_{48}. Hence, Hsc70/DNAJB1 initiates the binding to HTTEx1Q_{48}. To map the binding sites of DNAJB1 and Hsc70 with HTTEx1Q_{48} cross-linking mass-spectrometry was performed by colleagues in our lab. Both chaperones were found to interact with the second proline stretch of the proline rich domain of HTTEx1. Notably, the interaction between Hsc70 and HTTEx1Q_{48} was only observed in the presence of DNAJB1, whereas DNAJB1 interacted on its own with HTTEx1Q_{48}. The binding site for DNAJB1 was mapped to a conserved 9 amino acid stretch located in its C-terminal domain between the C-terminal domain I and the C-terminal domain II.

3.1.1 Effect of mutations in the HTT binding motif of DNAJB1 on the suppression of HTTEx1 aggregation

The HTT binding site of DNAJB1 contains two highly conserved amino acids, K242 and H244 (Fig. 3.4a). Introduction of a histidine to alanine mutation completely abolished the ability of the trimeric chaperone complex to suppress Huntingtin aggregation (Ayala Mariscal *et al.*, 2022). To investigate, if the H244A mutation had an effect on the structure or stability of DNAJB1, circular dichroism (CD) measurements over a temperature range from 20 – 90 °C were performed (Fig. 3.1 top). The CD spectra of DNAJB1^{wt} and DNAJB1^{H244A} were similar, indicating no major structural differences. Also, the melting temperature of DNAJB1^{wt}= 67.78 °C and DNAJB1^{H244A}= 64.74 °C were close to each other. These results support the

conclusion that the structure and stability of DNAJB1 was not affected by the H244A mutation. Furthermore, DNAJB1^{H244A} showed no defect in its functionality towards other substrates like luciferase or Aβ_{1-42} (Ayala Mariscal *et al.*, 2022).

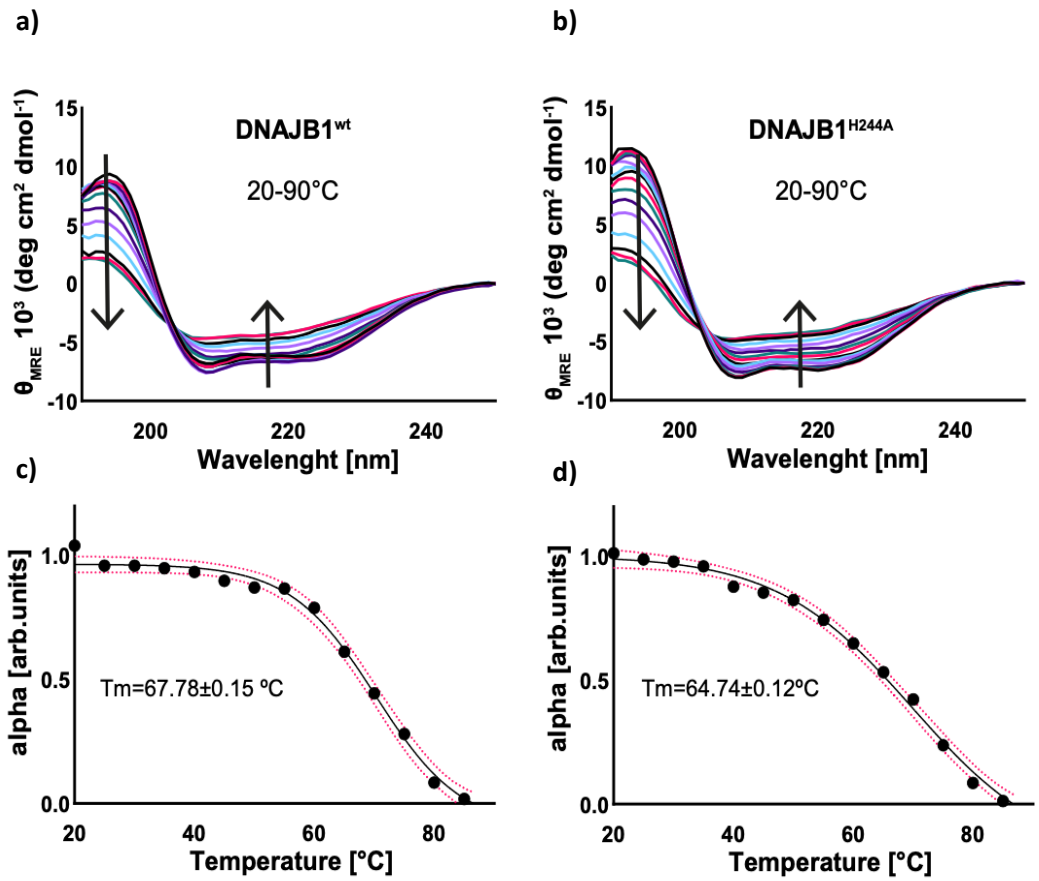

Figure 3.1: Structural integrity analysis of DNAJB1^{H244A}

At the top, CD spectra of DNAJB1^{wt} (a) and DNAJB1^{H244A} (b) over a temperature range of 20 - 90 °C are shown. Downward arrows indicate a decrease and upward arrows an increase over the temperature range. At the bottom the calculation of the melting temperature (Tm) is shown. Tm is defined as α = 0.5 (c and d) (Figure adapted from Ayala Mariscal et al., 2022)

The observation that the H244A mutation of DNAJB1 completely abolished the ability of the trimeric chaperone complex to suppress aggregation of specifically HTTEx1Q$_{48}$, demonstrates the importance of H244. To better understand the underlying mechanism, H244 was substituted with other amino acids. Substitution of H244 with arginine (experiments performed by Sara Ayala Mariscal, published in Ayala Mariscal *et al.*, 2022), another positively charged amino acid, partially recovered the ability to

suppress HTTEx1 aggregation. This observation posed the question whether a polar and/or positively charged residue is sufficient at position 244.

To address this question, I mutated H244 to glutamine, a polar amino acid with the ability to form hydrogen bonds. To investigate HTTEx1Q$_{48}$ aggregation a FRET based assay was employed (Scior *et al.*, 2018). HTTEx1Q$_{48}$-CyPet and HTTEx1Q$_{48}$-YPet were mixed in equimolar ratios. Upon aggregation the fluorophores come close to each other and allow detection of a FRET signal. For quantification, the half-life time (T ½) of the aggregation was determined. Compared to the other tested H244 mutations, the H244Q mutation achieved the best suppression of HTTEx1Q$_{48}$ aggregation (Fig. 3.2b yellow curve/bar) with $T_{½}$= 24.6 h but still did not reach the same value as the wild type (Fig. 3.2b red curve/bar) with $T_{½}$= 27.0 h. In the luciferase refolding activity of heat denatured luciferase, this mutant showed no defect (Luciferase assays were performed by Merve Özel (Kirstein lab)) (Fig. 3.2a).

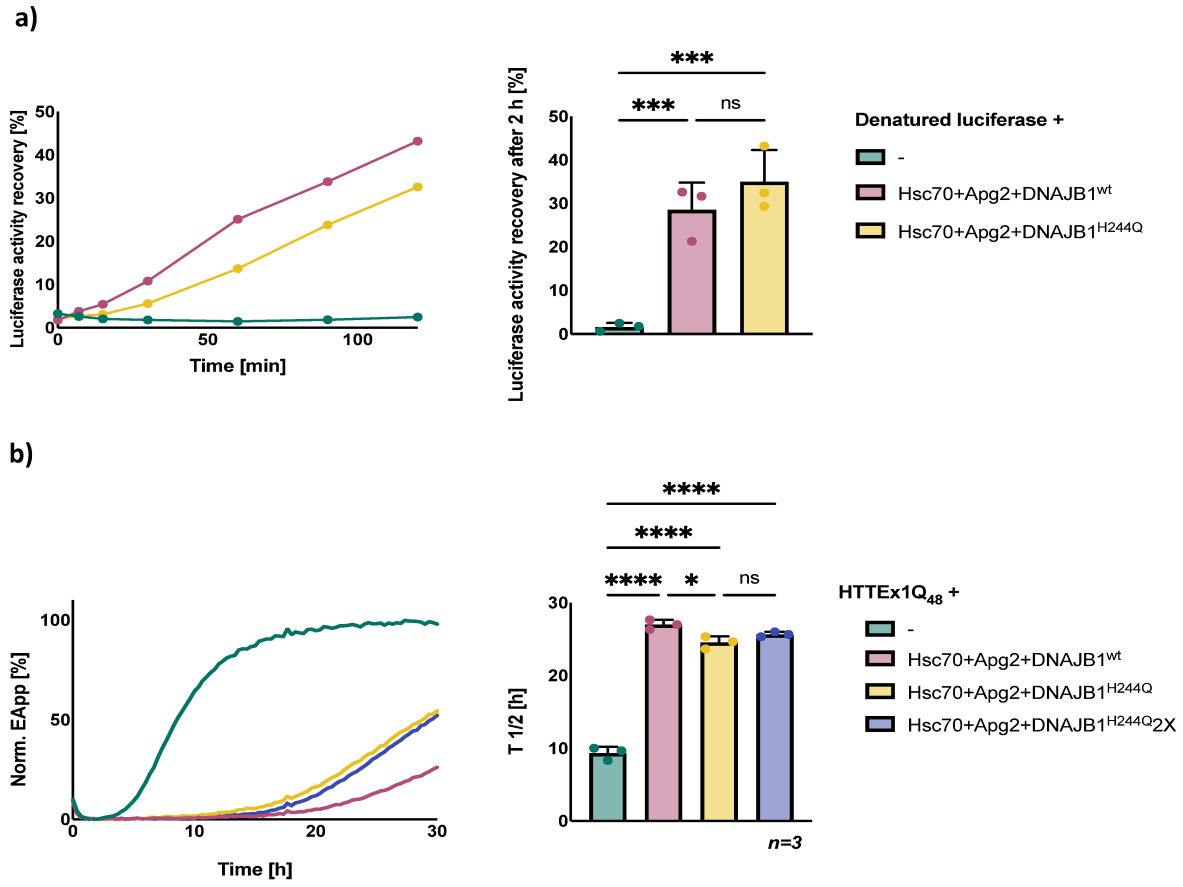

Figure 3.2: Luciferase refolding activity and suppression of HTTExon1Q$_{48}$ aggregation by DNAJB1^{H244Q}

a) Heat-denatured luciferase was refolded by Hsc70, Apg2 and DNAJB1^{wt} (red) or DNAJB1^{H244Q} (yellow). To measure refolding efficiency, luminescence emission of the refolded enzyme was measured over time. The graph on the left depicts a representative result of three independent experiments. The bar graph on the right depicts the mean values for the final luciferase activity recovery after 2 h with error bars corresponding to the SD. Data were analyzed by a one-way ANOVA. ***p ≤ 0.001; ns not significant. **b)** HTTExon1Q$_{48}$ aggregation was followed by FRET measurements where an increase in FRET efficiency corresponds to HTTExon1Q$_{48}$ fibril formation. The graph on the left is a representative result of three independent experiments and shows the normalized apparent FRET efficiency over time of HTTExon1Q$_{48}$ alone (green) + Hsc70 + Apg2 + DNAJB1^{wt} (red), DNAJB1^{H244Q} (yellow) or DNAJB1^{H244Q} 2x (blue). The right graph shows the half-life ($T_{1/2}$) of HTTExon1Q$_{48}$ aggregation for each individual experiment. Data were analyzed by a one-way ANOVA. *p≤ 0.05; ****p ≤ 0.0001; ns not significant.

This observation further posed the question whether a polar and/or positively charged residue is sufficient at position 244. To investigate whether a substitution of H244 by a non-polar amino acid would hence interfere with the binding of HTTEx1Q$_{48}$, I mutated H244 to phenylalanine to introduce a non-polar ring-structured amino acid of similar size. The ability to suppress HTTEx1Q$_{48}$ aggregation was as impaired as for the H244A mutation (Fig. 3.3b). Hsc70, Apg2 and DNAJB1^{wt} were able to suppress HTTEx1Q$_{48}$ fibrilization with $T_{½}$= 25.6 h (Fig. 3.3b red curve/bar) while with Hsc70, Apg2 and DNAJB1^{H244F} $T_{½}$= 10.4 h (Fig. 3.3b yellow curve/bar) which was not significantly different from HTTEx1Q$_{48}$ alone ($T_{½}$ =8.6 h Fig. 3.3b green curve/bar). Increasing the concentration of DNAJB1^{H244F} to double the amount of the chaperone, did not improve the ability to suppress HTTEx1Q$_{48}$ fibrilization ($T_{½}$ = 10.6 h Fig. 3.3b purple curve/bar). Notably, its ability to refold heat denatured luciferase was not impaired. Both Hsc70, Apg2, DNAJB1^{wt} or DNAJB1^{H244F} showed a luciferase refolding efficiency of 45.0 / 41.8 % (Fig 3.3a), indicating that hydrophilic amino acids at position 244 are required for efficient HTTEx1Q$_{48}$ interaction and suppression of aggregation.

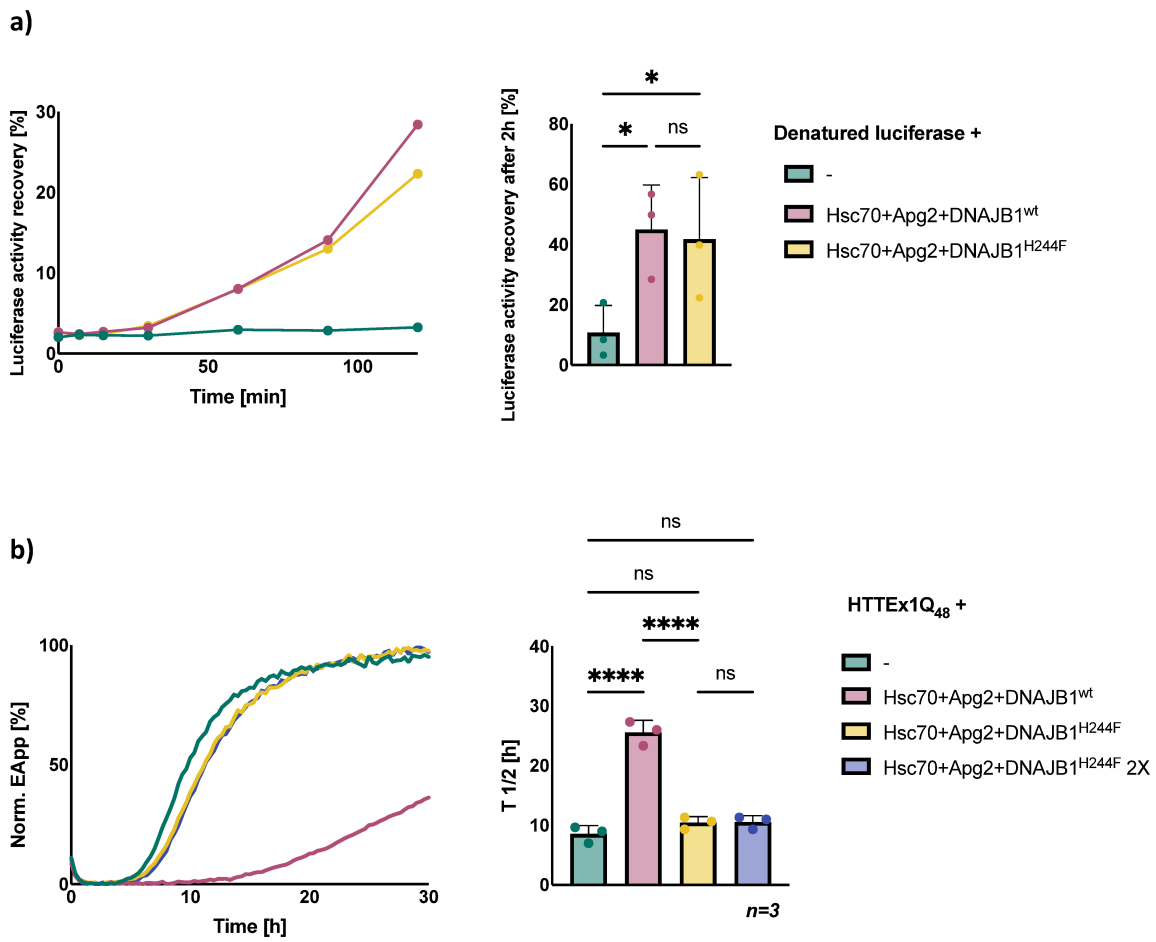

Figure 3.3: Luciferase refolding activity and suppression of HTTExon1Q$_{48}$ aggregation by DNAJB1^{H244F}

a) Heat-denatured luciferase was refolded by Hsc70, Apg2 and DNAJB1^{wt} (red) or DNAJB1^{H244F} (yellow). To measure refolding efficiency, luminescence emission of the refolded enzyme was measured over time. The graph on the left depicts a representative result of three independent experiments. The bar graph on the right depicts the mean values for the final luciferase activity recovery after 2 h with error bars corresponding to the SD. Data were analyzed by a one-way ANOVA. *p ≤ 0.05; ns not significant. **b)** HTTExon1Q$_{48}$ aggregation was followed by FRET measurements where an increase in FRET efficiency corresponds to HTTExon1Q$_{48}$ fibril formation. The graph on the left is a representative result of three independent experiments and shows the normalized apparent FRET efficiency over time of HTTExon1Q$_{48}$ alone (green) + Hsc70 + Apg2 + DNAJB1^{wt} (red), DNAJB1^{H244F} (yellow) or DNAJB1^{H244F} 2x (blue). The right graph shows the half-life ($T_{1/2}$) of HTTExon1Q$_{48}$ aggregation for each individual experiment. Data were analyzed by a one-way ANOVA. ****p ≤ 0.0001; ns not significant.

3.1.2 Effect of conserved amino acids adjacent to the HTT binding motif of DNAJB1 on the suppression of HTTEx1 aggregation

The binding motif that was found by cross-linking mass spectrometry consisted of 9 amino acids. Taking a look at the amino acids directly adjacent to the binding motif revealed three more highly conserved residues, D234, F247 and R249 (Fig. 3.4a). This posed the question if these residues also affect binding and suppression of HTTEx1Q_{48} aggregation. To test this, these residues were mutated to alanine individually. The generated mutants were tested for their general activity first. An ATPase assay was performed to test if the mutants were still able to induce the ATP hydrolysis activity of Hsc70 (Fig. 3.4b). The ATPase activity of Hsc70 and DNAJB1 or the respective mutants were normalized to the intrinsic ATPase hydrolysis activity of Hsc70. DNAJB1^{D234A} (yellow), DNAJB1^{F247A} (blue) and DNAJB1^{R249A} (purple) were still able to induce the ATPase activity of Hsc70 similarly to DNAJB1^{wt} (red). Additionally, these mutants showed no defect in the refolding of heat denatured luciferase compared to DNAJB1^{wt} (Figure 3.4c, same color coding) indicating, that the protein function in general was not impaired by the D234A, F247A or R249A mutation.

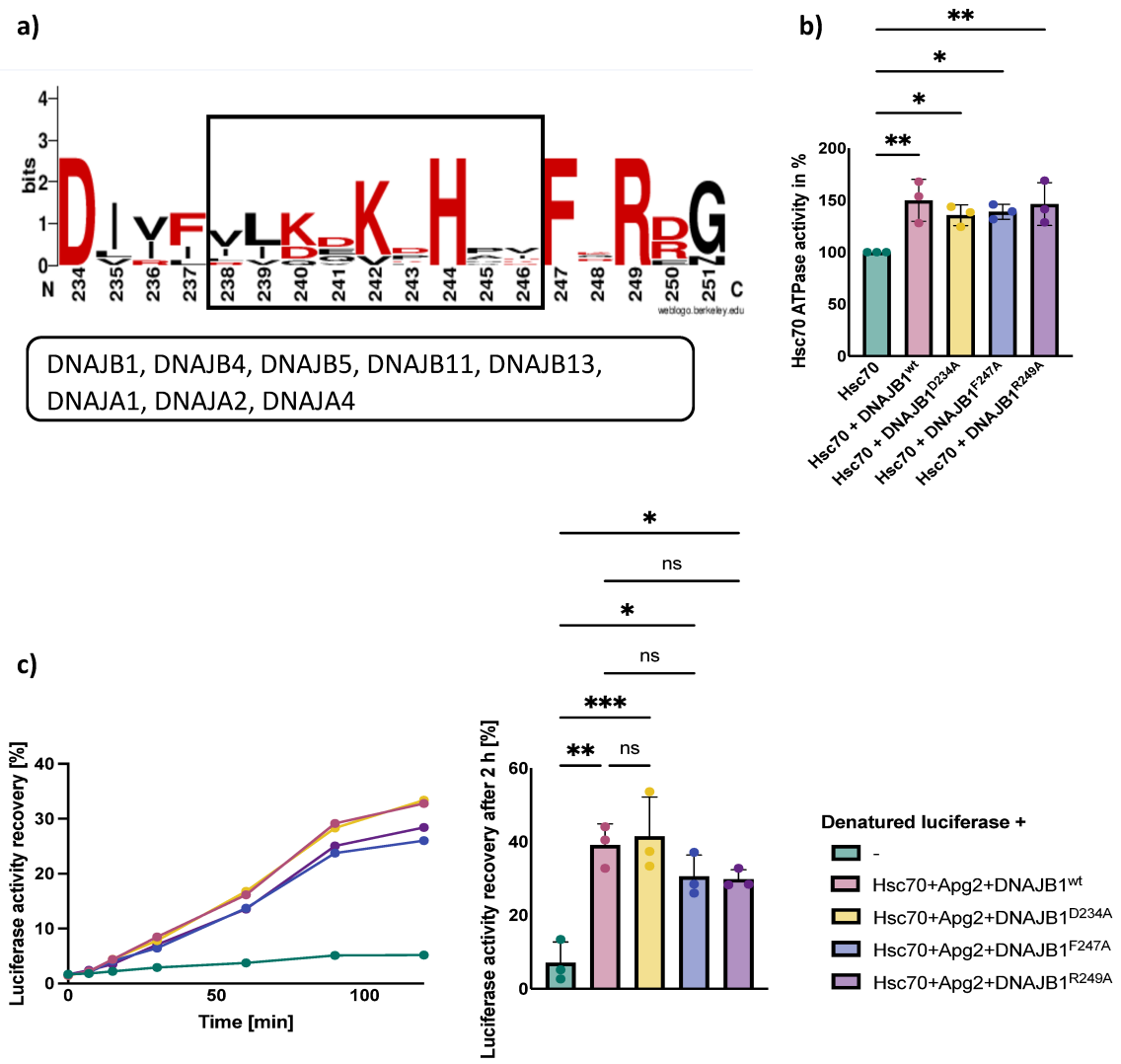

Figure 3.4: Stimulation of the Hsc70 ATPase activity and Luciferase refolding activity by DNAJB1^{D234A}, DNAJB1^{F247A} and DNAJB1^{R249A}

a) Sequence logo of the Huntingtin binding motif (black frame) and flanking amino acids. Red colored amino acids indicate highly conserved and charged residues in the motif. Underneath shown J-domain proteins were used for sequence comparison. **b)** Comparison of the ATPase activity of only Hsc70 and upon addition of DNAJB1^{wt}, DNAJB1^{D234A}, DNAJB1^{D247A} or DNAJB1^{R249A}. The ATPase activity of Hsc70 + J-protein was normalized to the intrinsic ATPase activity of Hsc70. The graph shows the means of three independent experiments with error bars corresponding to the SD. Data were analyzed by one-way ANOVA. *p≤ 0.05; ** p≤ 0.01. **c)** Heat-denatured luciferase was refolded by Hsc70, Apg2 and DNAJB1^{wt} (red), DNAJB1^{D234A} (yellow), DNAJB1^{D247A} (blue) or DNAJB1^{R249A} (purple). To measure refolding efficiency, luminescence emission was measured over time. The graph on the left depicts a representative result of three independent experiments. The bar graph on the right depicts the mean values for the final luciferase activity recovery after 2 h with error bars corresponding to the SD. Data were analyzed by a one-way ANOVA. *p≤ 0.05; ** p≤ 0.01; ***p ≤ 0.001; ns not significant.

However, the mutants showed defects in the suppression of HTTEx1Q$_{48}$ aggregation (Fig 3.5). For the R249A mutation, the effect was most severe with $T_{½}$= 13.0 h and $T_{½}$= 16.3 h for R249A 2x (Fig. 3.5 teal and pink curve/bar). The other mutations were less impaired, with $T_{½}$= 21.3 h for F247A and $T_{½}$= 23.8 h for F247A 2x (Fig. 3.5 purple and orange curve/bar). D234A was barely impaired with $T_{½}$= 26.7 h and $T_{½}$= 28.0 h for D234A 2x (Fig. 3.5 yellow and blue curve/bar) which was close to the $T_{½}$ of DNAJB1^{wt} with $T_{½}$= 33.9 h. Interestingly, the positively charged residue was most important for the ability of DNAJB1 to interact with HTTEx1Q$_{48}$ and suppress its aggregation in this situation as well. From this I conclude that the conserved amino acids adjacent to the HTT binding motif play a role in HTT interaction and suppression of aggregation as well. Mutating these amino acids did not have an as severe impact compared to the H244A and H244F mutations. For this reason, the subsequent analyses focused on H244 and the H244A mutation.

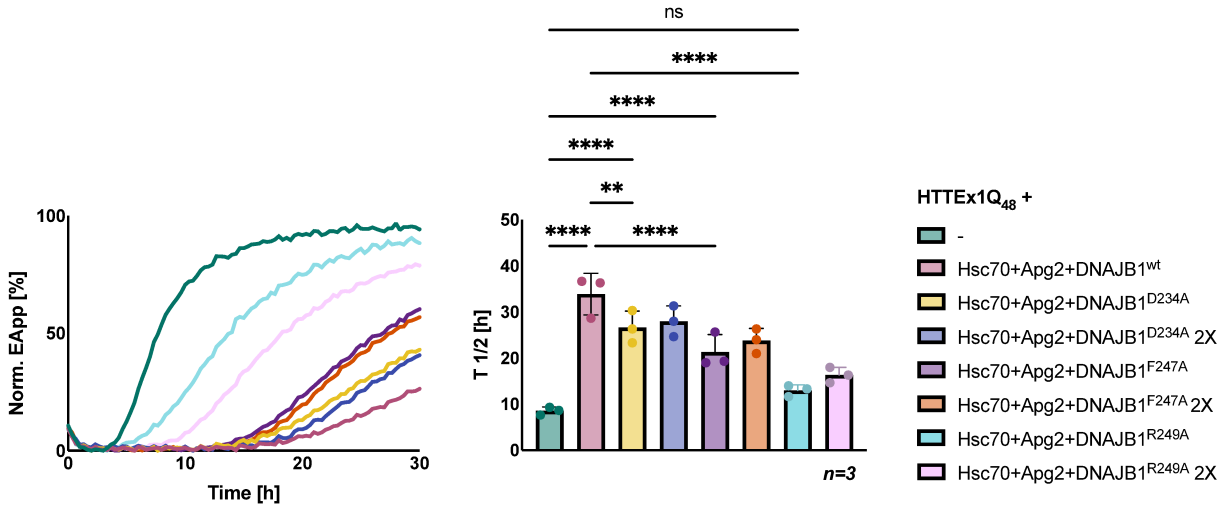

Figure 3.5: Effect of DNAJB1^{D234A}, DNAJB1^{F247A} and DNAJB1^{R249A} on the suppression of HTTEx1Q$_{48}$ aggregation

HTTExon1Q$_{48}$ aggregation was followed by FRET measurements where an increase in FRET efficiency corresponds to HTTExon1Q$_{48}$ fibril formation. The graph on the left is a representative result of three independent experiments and shows the normalized apparent FRET efficiency over time of HTTExon1Q$_{48}$ alone (green) + Hsc70 + Apg2 + DNAJB1^{wt} (red), DNAJB1^{D234A} (yellow), DNAJB1^{D234A} 2x (blue), DNAJB1^{F247A} (purple), DNAJB1^{F247A} 2x (orange), DNAJB1^{R249A} (teal), DNAJB1^{R249A} 2x (pink). The right graph shows the half-life ($T_{1/2}$) of HTTExon1Q$_{48}$ aggregation for each individual experiment. Data were analyzed by a one-way ANOVA. **p≤ 0.01; ****p ≤ 0.0001; ns not significant.

3.1.3 *In silico* modelling revealed further amino acids involved in HTT binding

Since it became clear from the experiments performed so far that a hydrophilic amino acid is required at position 244 for efficient HTTEx1Q$_{48}$ interaction the question was how the histidine residue is involved in proline binding as proline is a non-charged and non-polar amino acid. To address that question our lab collaborate with I.L. Grothaus, S. Köppen and L. Colombi Ciacchi (Universität Bremen) who performed *in silico* analyses using molecular dynamics simulations. Based on these results I performed further experiments to gain a better understanding of how DNAJB1 is interacting with the proline rich domain.

First DNAJB1 was modelled alone. The model was constructed from the crystal structure and simulated in solution over a time of 500 ns. From those simulations a contact map was created (Fig. 3.6) showing interactions from amino acids of the Huntingtin binding motif with amino acids of the CTDI and the CTDII for DNAJB1^{wt} (Fig. 3.6 middle section top part, dark blue squares indicate strong interaction). Upon introduction of the H244A mutation the contact map showed changes, especially the interaction between H244 and E173 changed from a strong interaction in the wt to no interaction in the H244A mutation (Fig. 3.6 highlighted by the red arrows). Taking a closer look on that interaction revealed, that H244 forms a continuous hydrogen bond with E173. This formation of a hydrogen bond was no longer possible when H244 was mutated to alanine, since alanine misses the hydrogen bonding donors to interact with E173.

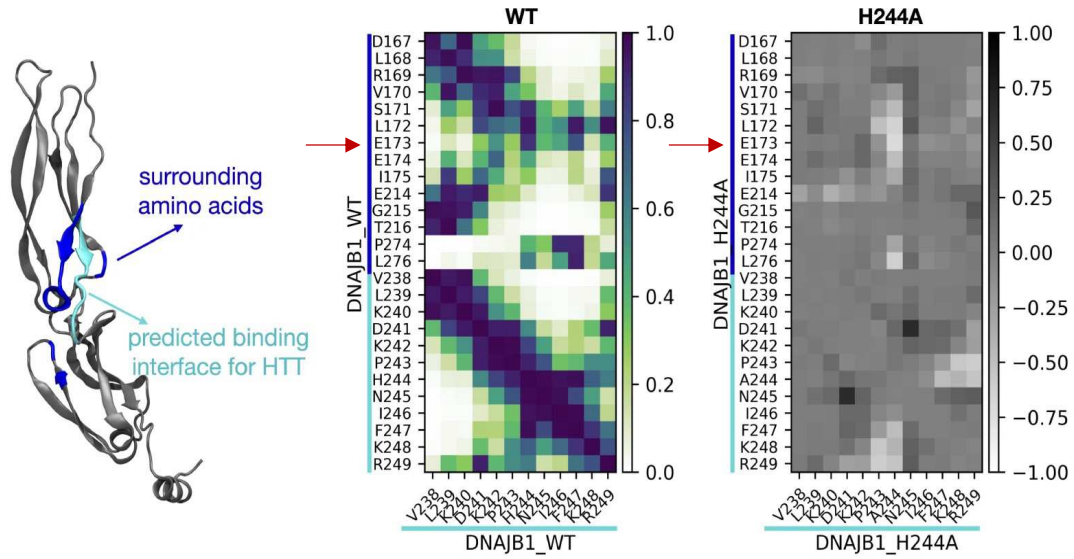

Figure 3.6: Contact map of DNAJB1^{wt} and DNAJB1^{H244A}

The atomic structure of monomeric DNAJB1^{wt} is shown on the left. Based on this, a contact map was generated representing contacts of the HBM and the surrounding amino acids (middle image). Upon introduction of the H244A mutation, the contact map changes as shown on the right. Positive values indicate an increase and negative values a decrease in interaction. Residue E173 is highlighted by red arrows in both contact maps. (Figure adapted from Ayala Mariscal *et al.*, 2022)

The question then was if the H244-E173 interaction is vital for the activity of DNAJB1 to suppress HTTEx1Q$_{48}$ aggregation and the reason for the detrimental effect of H244A mutation on HTTEx1Q$_{48}$ suppression of aggregation. E173 is highly conserved among class A and B J-domain proteins, which contain a Huntingtin binding motif. Directly adjacent to E173 is a second glutamic acid E174, which is also highly conserved. I mutated both amino acids separately to alanine, to impair hydrogen bond formation with H244. First, the newly generated mutants E173A and E174A were tested for their general chaperone activity. The function to induce ATPase activity of Hsc70 was not impaired (Fig. 3.7a). Both DNAJB1^{E173A} (yellow) and DNAJB1^{E147A} (blue) did not differ from DNAJB1^{wt} (red) in their ability to induce the ATPase activity of Hsc70. Luciferase refolding activity of heat denatured luciferase was not impaired either (Fig. 3.7b same color scheme). From that I conclude that DNAJB1^{E173A} and DNAJB1^{E174A} were structurally intact proteins.

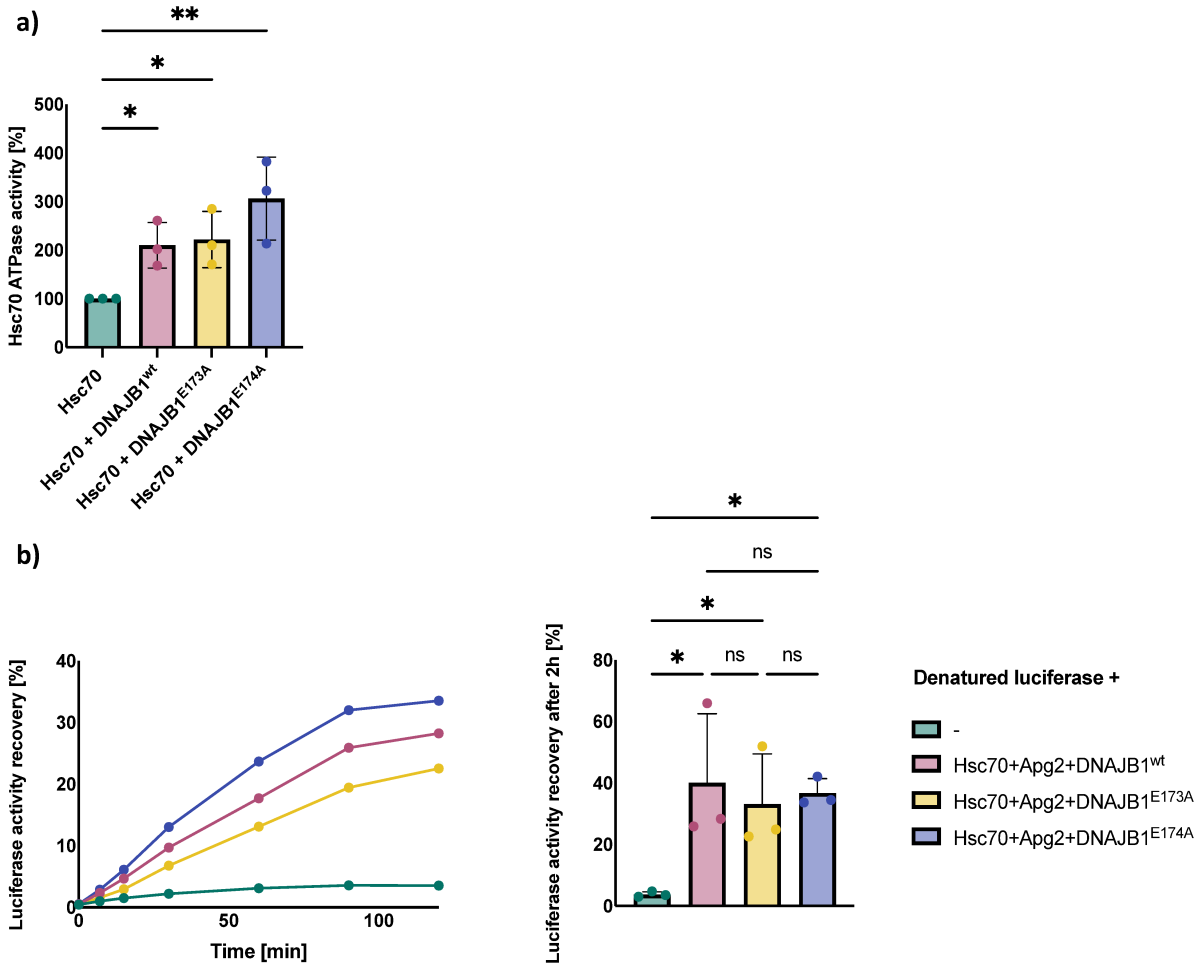

Figure 3.7: Stimulation of the Hsc70 ATPase activity and Luciferase refolding activity by DNAJB1^{E173A} and DNAJB1^{E174A}

a) Comparison of the ATPase activity of Hsc70 alone and upon addition of DNAJB1^{wt}, DNAJB1^{E173A} or DNAJB1^{E174A}. The ATPase activity of Hsc70 + J-protein was normalized to the intrinsic ATPase activity of Hsc70. The means of three independent experiments are shown in the graph with error bars corresponding to the SD. Data were analyzed by one-way ANOVA. *p≤ 0.05; **p≤ 0.01. **b)** Heat-denatured luciferase was refolded by Hsc70, Apg2 and DNAJB1^{wt} (red), DNAJB1^{E173A} (yellow) or DNAJB1^{E174A} (blue). To measure refolding efficiency, luminescence emission was measured over time. The graph on the left depicts a representative result of three independent experiments. The bar graph on the right depicts the mean values for the final luciferase activity recovery after 2 h with error bars corresponding to the SD. Data were analyzed by a one-way ANOVA. *p≤ 0.05; **p≤ 0.01; ns not significant.

Next, I assessed the ability of E173A and E174A to suppress HTTEx1Q$_{48}$ aggregation together with Hsc70 and Apg2. Interestingly, the E173A mutation behaves like the wt with $T_{½}$= 30.7 h (Fig. 3.8 yellow curve/bar). This indicates that the intramolecular

hydrogen bond between H244 and E173 is not crucial for its function to interact with HTTEx1Q$_{48}$. However, when the adjacent E174 was mutated to alanine, the ability of the trimeric chaperone complex to suppress HTTEx1Q$_{48}$ aggregation was completely abolished $T_{½}$= 12.3 h (Fig. 3.8 blue curve/bar), which resembles the phenotype of the H244A/F mutations. Also increasing the concentration of DNAJB1^{E174A} had no effect $T_{½}$= 12.3 h (Fig. 3.8 purple curve/bar). However, E174 is not part of the Huntingtin binding site of DNAJB1. Although, E174 seems not to be directly involved in substrate recognition here, it was found that it forms a stable hydrogen network with S171, C179 and K181, which was shown to interact with Hsc70 by NMR experiments (Jiang, Rossi and Kalodimos, 2019). For this reason, it is likely that the E174A mutation disturbs this hydrogen bond network and consequently the ability of the trimeric chaperone complex to suppress HTTEx1Q$_{48}$ aggregation.

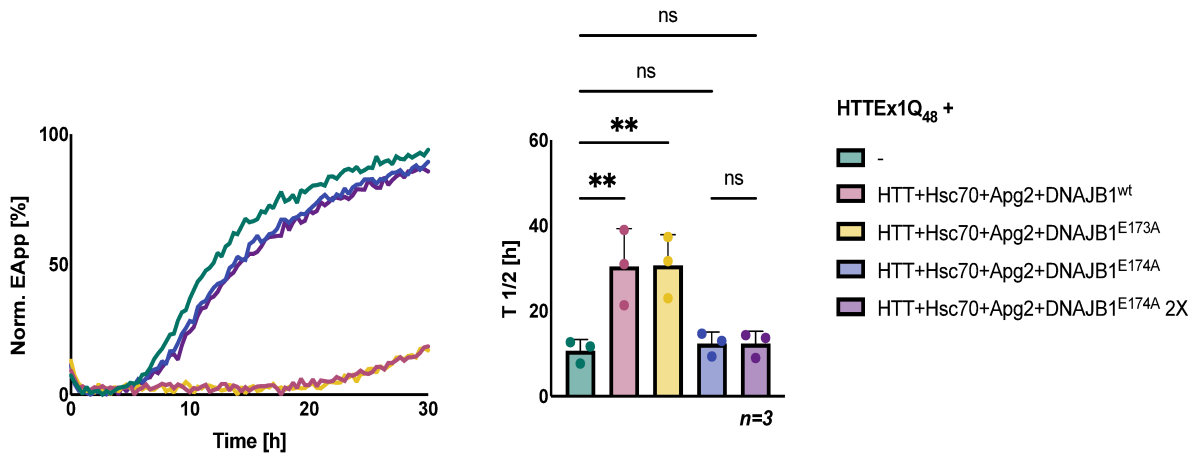

Figure 3.8: Effect of DNAJB1^{E173A} and DNAJB1^{E174A} on the suppression of HTTExon1Q$_{48}$ aggregation

HTTExon1Q$_{48}$ aggregation was followed by FRET measurements where an increase in FRET efficiency corresponds to HTTExon1Q$_{48}$ fibril formation. The graph on the left is a representative result of three independent experiments and shows the normalized apparent FRET efficiency over time of HTTExon1Q$_{48}$ alone (green) + Hsc70 + Apg2 + DNAJB1^{wt} (red), DNAJB1^{E173A} (yellow), DNAJB1^{E174A} (blue) or DNAJB1^{E174A} 2x (purple). The right graph shows the half-life ($T_{1/2}$) of HTTExon1Q$_{48}$ aggregation for each individual experiment. Data were analyzed by a one-way ANOVA. *p≤ 0.05; **p ≤ 0.01; ns not significant.

As the hydrogen bond between H244 and E173 seemed not crucial for DNAJB1 to interact with HTTEx1Q$_{48,}$ the question why H244 is so important for HTTEx1Q$_{48}$ binding remained and why mutating E173 to alanine and thereby removing the predicted binding partner of H244 showed no effect on the suppression of HTTEx1Q$_{48}$.

To address these questions and to gain further mechanistic insight into how the Huntingtin binding motif interacts with the proline rich domain of HTTEx1Q$_{48}$, docking simulations were performed by collaboration partners I.L. Grothaus, S. Köppen and L. Colombi Ciacchi. For HTTEx1Q$_{48}$, five clusters were identified and docked to DNAJB1. In subsequent molecular dynamics simulations only two of them formed a stable complex with DNAJB1 over a simulation time of 500 ns (Ayala Mariscal *et al.*, 2022). In the simulations the residues P243, H244, N245, I246 and K248 of DNAJB1 were those who formed major contacts with the second proline stretch of the proline rich domain (Fig. 3.9 top contact map for DNAJB1^{wt}).

As described earlier, H244 forms a hydrogen bond with E173, thereby only the backbone atoms of H244 were interacting with the proline rich domain (Fig. 3.9 top molecular model for DNAJB1^{wt}). In the H244A mutant this hydrogen bond did no longer exist, which allowed the side chain of residue 244 to rotate outwards disrupting the binding of the backbone and HTTEx1Q$_{48}$. For that reason, the clusters detached and moved away, which also shows in the faint contact map (Fig. 3.9 contact map for DNAJB1^{H244A}). Interestingly, the contact maps for DNAJB1^{E173A} and DNAJB1^{E174A} did not differ that much from the one for DNAJB1^{wt}. D241, P243, H244 and N245 still remained in close contact to the proline residues (Fig. 3.9 contact map for DNAJB1^{E173A} and DNAJB1^{E174A}). Although in both simulations for the mutants, the hydrogen bond between H244 and E173 was no longer formed. In the simulations for DNAJB1^{E173A} the side chain of H244 was rotating outwards but instead of disrupting the binding of the proline stretch, it formed a hydrogen bond with the backbone atoms of the prolines. In the simulations for DNAJB1^{E174A}, E173 formed a hydrogen bond with N245 instead of H244, which then again rotated outside and formed a hydrogen bond with the backbone atoms of the proline stretch (Fig. 3.9 bottom molecular model for DNAJB1^{E174A}).

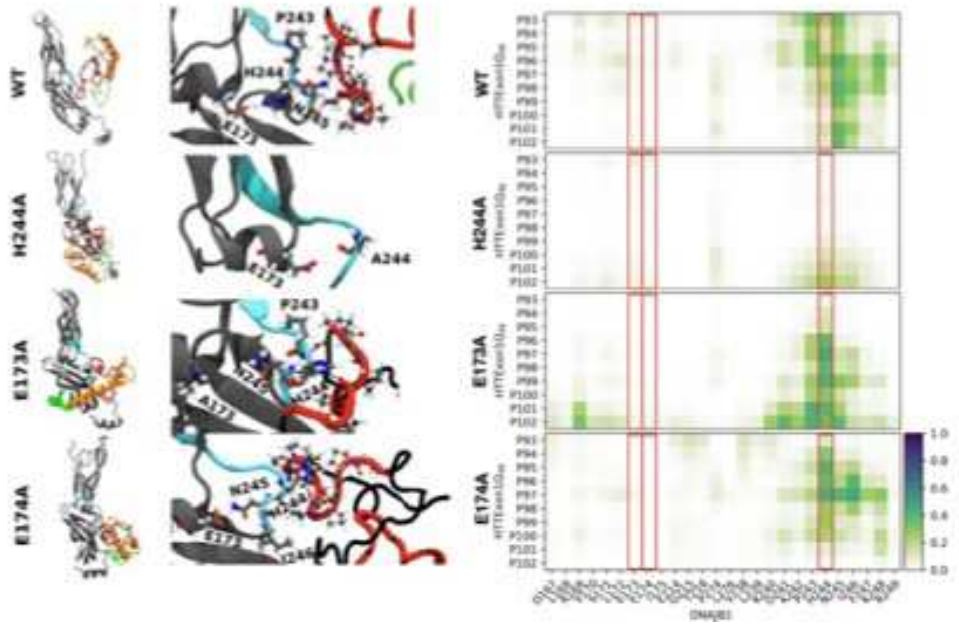

Figure 3.9: Molecular dynamics simulations of DNAJB1^{wt}, DNAJB1^{H244A}, DNAJB1^{E173A} and DNAJB1^{E174A}

On the left, molecular dynamic snapshots of DNAJB1^{wt} or the respective DNAJB1 mutant monomer in complex with HTTExon1Q$_{48}$ are shown. DNAJB1 is shown in grey with highlighted amino acids color coded according to the atom types: hydrogen (white), carbon (cyan), oxygen (red), nitrogen (blue). The HTT binding motif of DNAJB1 is shown in cyan and HTTExon1Q$_{48}$ is color coded by domains: PolyQ (orange), PRD (P1 and P2: red; residues between P1 and P2: black), N17 (green). Hydrogen bonds are indicated by dotted lines. Although for simplicity only monomeric DNAJB1 is shown, simulations were performed with DNAJB1 dimers. On the right, contact maps of DNAJB1^{wt} or the respective DNAJB1 mutant and HTTExon1Q$_{48}$ are shown. Focusing on the HTT binding motif and the P2 domain. E173, E174 and H244 are shown in red boxes. (Figure adapted from Ayala Mariscal *et al.*, 2022)

These *in silico* modelling results support the mass spectrometry findings of the binding sites being located between residues 238 and 246 of DNAJB1 and the second proline stretch in the proline rich domain. Where H244 is a key amino acid, that stabilizes the interactions by the formations of hydrogen bonds. This model also gives an explanation why the H244A mutation is so impaired in its function of binding to HTTEx1, since alanine can no longer form hydrogen bonds and therefore destabilizes the complex. Also, this model is in line with the experimental data that were obtained for the H244Q mutant, indicating how glutamine is able to functionally replace histidine and why phenylalanine fails to functionally substitute histidine.

3.1.4 Suppression of HTTEx1 aggregation requires Hsc70-DNAJB1 interaction

Next, I investigated the Hsc70 dependency of the process by using a DNAJB1 mutant that has a mutation in the HPD motif where H32 is replaced by glutamine impairing its interaction with Hsc70. Additionally, a double mutant of DNAJB1 with two amino acid exchanges, H32Q and H244A was created. For both the mutants, DNAJB1^{H32Q} and DNAJB1$^{H32Q\text{-}H244A}$ an ATPase assay was performed by Merve Özel (Kirstein lab). DNAJB1^{H32Q} and DNAJB1$^{H32Q\text{-}H244A}$ were not able to induce the ATPase activity of Hsc70 anymore (Fig. 3.10a). There was no significant difference between the intrinsic ATP hydrolysis activity of Hsc70 alone (green) and Hsc70 with the DNAJB1 mutants. This in a way was expected as H32 is known to be essential for the stimulation of ATPase activity (Kityk, Kopp and Mayer, 2018).

In the luciferase refolding assay (Fig. 3.10 performed by Merve Özel) DNAJB1^{H32Q} and DNAJB1$^{H32Q\text{-}H244A}$ together with Hsc70 and Apg2 (yellow curve/bar) were unable to refold heat denatured luciferase. The refolding efficiency of 3.7 % for DNAJB1^{H32Q} and 1.6 % for DNAJB1$^{H32Q\text{-}H244A}$ did not differ from the negative control with 2.0 %, where heat-denatured luciferase was incubated without any chaperones (green curve/bar).

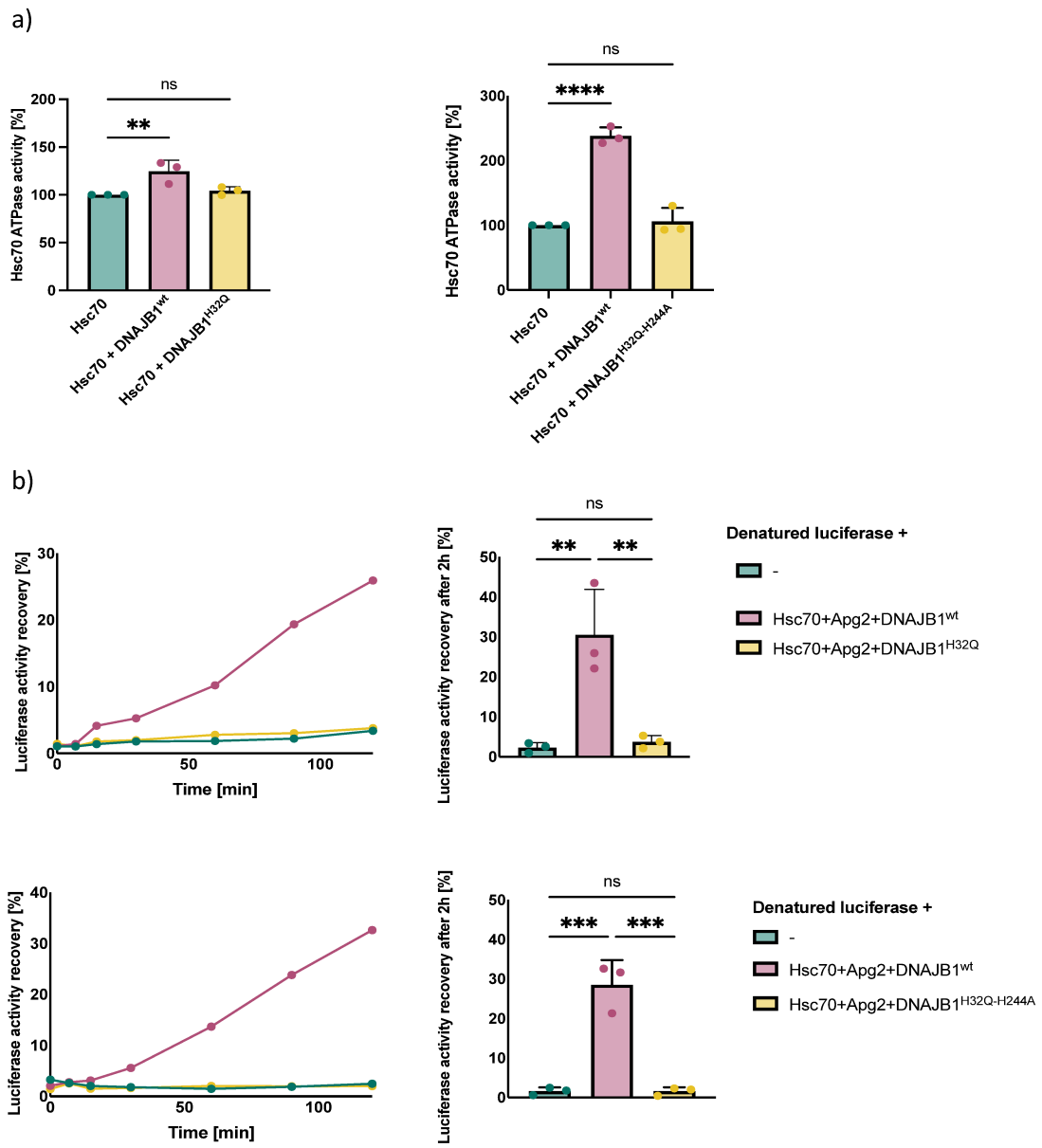

Figure 3.10: Stimulation of the Hsc70 ATPase activity and Luciferase refolding activity by DNAJB1^{H32Q} and DNAJB1$^{H32Q-H244A}$

a) Comparison of the ATPase activity of Hsc70 alone and upon addition of DNAJB1^{wt}, DNAJB1^{H32Q} or DNAJB1$^{H32Q-H244A}$. The ATPase activity of Hsc70 + J-protein was normalized to the intrinsic ATPase activity of Hsc70. The means of three independent experiments are shown in the graph with error bars corresponding to the SD. Data were analyzed by one-way ANOVA. **** p≤ 0.0001; ** p≤ 0.01; ns not significant. **b)** Heat-denatured luciferase was refolded by Hsc70, Apg2 and DNAJB1^{wt} (red) or DNAJB1^{H32Q} / DNAJB1$^{H32Q-H244A}$ (yellow). To analyze refolding efficiency, luminescence emission was measured over time. The graph on the left depicts a representative result of three independent experiments. The bar graph on the right depicts the mean values for the final luciferase activity recovery after 2 h with error bars corresponding to the SD. Data were analyzed by a one-way ANOVA. ** p≤ 0.01; ***p ≤ 0.001; ns not significant.

I performed FRET based HTTEX1Q$_{48}$ aggregation assays for DNAJB1^{H32Q} and DNAJB1$^{H32Q-H244A}$ to test their ability to suppress HTTEx1Q$_{48}$ aggregation. Previously it has been shown that DNAJB1 alone cannot suppress HTTEx1Q$_{48}$ aggregation and requires Hsc70 (Scior *et al.*, 2018). For that reason, as the H32Q mutation of DNAJB1 impairs its interaction with Hsc70 it is not expected to suppress aggregation. This hypothesis was confirmed in the experiments. The chaperone complex consisting of Hsc70, Apg2 and DNAJB1^{H32Q} was not able to suppress HTTEx1Q$_{48}$ aggregation (Fig. 3.11, top yellow curve/bar) with T$_{½}$= 8.0 h which was not significant different from HTTEx1Q$_{48}$ alone with T$_{½}$= 7.9 h. The double mutation DNAJB1$^{H32Q-H244A}$ showed the same result with T$_{½}$= 10.3 h (Fig. 3.11 bottom yellow curve/bar) which also was as expected as every mutation on its own already completely abolishes its function to suppress HTTEx1Q$_{48}$ aggregation. Increasing the chaperone concentration had no effect on the suppression efficiency either (Fig. 3.11, blue curve/bar top and bottom). From these results, it was concluded, that the suppression of HTTEx1 is dependent not only on the DNAJB1 substrate interaction but also on the interaction of Hsc70 and DNAJB1. For the suppression of HTTEx1Q$_{48}$ aggregation DNAJB1 has to be able to promote Hsc70 ATPase activity.

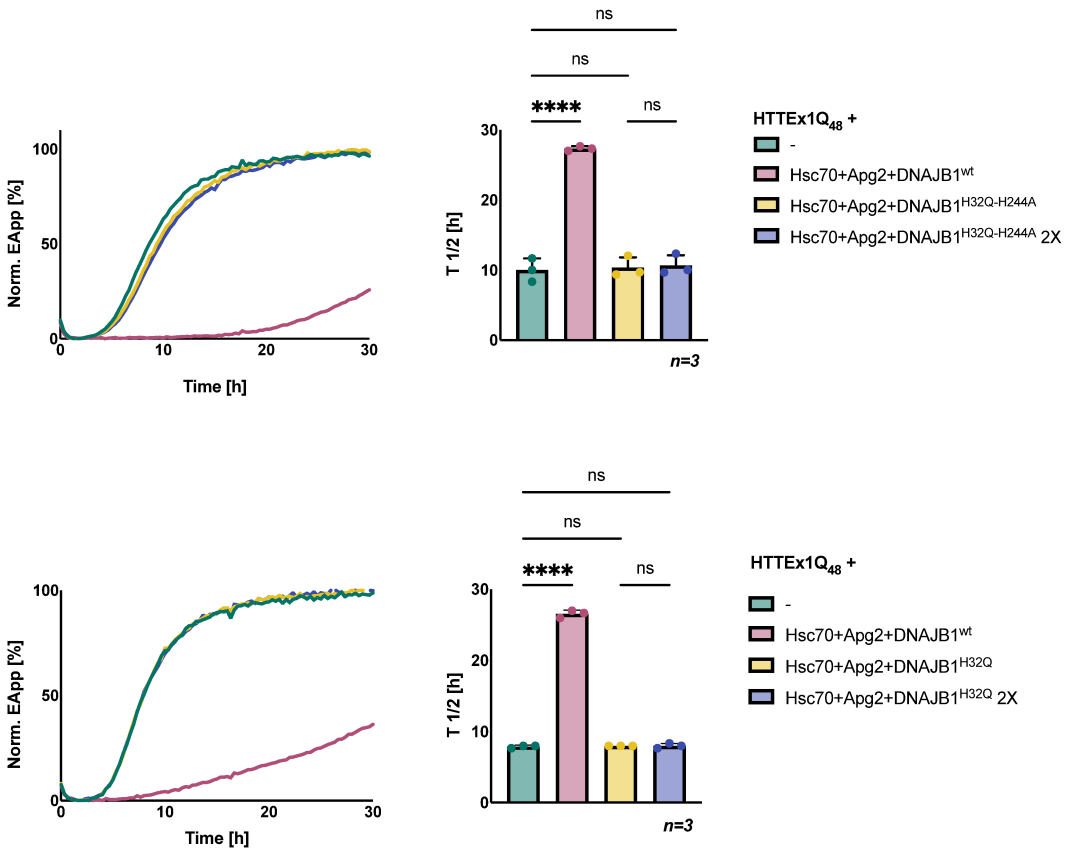

Figure 3.11: Effect of DNAJB1^{H32Q} and DNAJB1$^{H32Q-H244A}$ on the suppression of HTTExon1Q$_{48}$ aggregation

HTTExon1Q$_{48}$ aggregation was followed by FRET measurements where an increase in FRET efficiency corresponds to HTTExon1Q$_{48}$ fibril formation. The graph on the left is a representative result of three independent experiments and shows the normalized apparent FRET efficiency over time of HTTExon1Q$_{48}$ alone (green) + Hsc70 + Apg2 + DNAJB1^{wt} (red), DNAJB1^{H32Q} / DNAJB1$^{H32Q-H244A}$ (yellow) or DNAJB1^{H32Q} 2x / DNAJB1$^{H32Q-H244A}$ 2x (purple). The right graph shows the half-life ($T_{1/2}$) of HTTExon1Q$_{48}$ aggregation for each individual experiment. Data were analyzed by a one-way ANOVA. ****p ≤ 0.0001; ns not significant

3.1.5 Knockdown of DNAJB1 increased HTTExon1Q$_{97}$ foci formation in HEK293 cells

So far experiments were performed with purified proteins expressed in *E.coli.* To prove that the same principles hold true in human cells, I expressed HTTEx1Q$_{97}$-EGFP in HEK293 cells. Modulation of the expression levels of DNAJB1 should have an effect on HTTEx1 aggregation as FRET-based experiments have shown, that the DNAJB1 concentration is the limiting factor for suppression of HTTEx1 aggregation (Fig. 3.12). Keeping the other chaperone concentrations constant and just increasing the DNAJB1 concentration, improved the suppression of HTTEx1 aggregation. 5 µM Hsc70 + 0.25 µM Apg2 and 3 µM of DNAJB1 resulted in a half-life time of HTTEx1Q$_{48}$ of $T_{½}$= 14.7 h (Fig. 3.12 red curve). Increasing DNAJB1 to 4 µM suppressed HTTEx1Q$_{48}$ aggregation longer and led to a half-life time of $T_{½}$= 15.3 h (Fig. 3.12 yellow curve). A further increase of the concentration of DNAJB1 to 5 µM suppressed the aggregation of HTTEx1Q$_{48}$ even longer and resulted in $T_{½}$= 17.7 h (Fig. 3.12 blue curve).

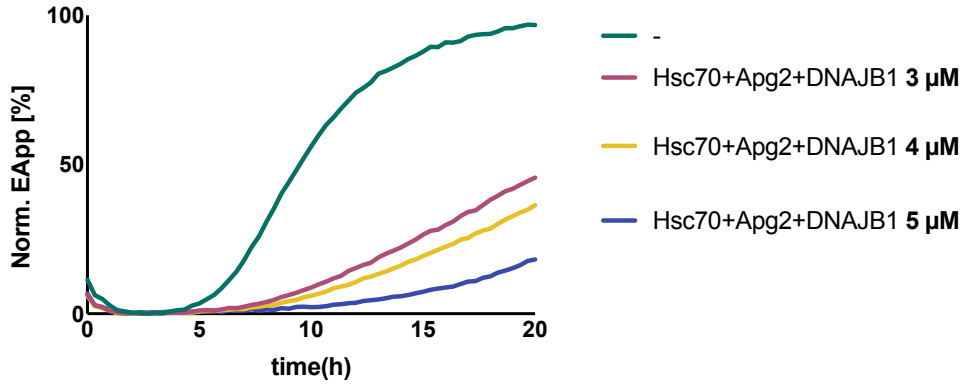

Figure 3.12: DNAJB1 is the limiting factor in suppression of HTTEx1 aggregation

HTTExon1Q_{48} aggregation was followed by FRET measurements where an increase in FRET efficiency corresponds to HTTExon1Q_{48} fibril formation. The graph shows the normalized apparent FRET efficiency over time of HTTExon1Q_{48} alone (green) + Hsc70 (5 µM) + Apg2 (0.25 µM) + **3 µM** DNAJB1 (red), + **4 µM** DNAJB1 (yellow) or + **5 µM** DNAJB1 (blue)

Based on the *in vitro* data, I hypothesized that an overexpression of DNAJB1 should suppress whereas a depletion of DNAJB1 should exacerbate the aggregation of HTTEx1Q_{97} in cultured cells. Mutating H244 of DNAJB1 should abrogate its ability to suppress HTTEx1Q_{97} aggregation and its overexpression should have no effect any longer on the aggregation of HTTEx1Q_{97}. The first HTTEx1Q_{97}-EGFP aggregates could already be observed 24 h after transfection due to the long PolyQ stretch. Expression of DNAJB1 was depleted using siRNA while at the same time either DNAJB1^{wt} or DNAJB1^{H244A} were overexpressed. An empty vector (EV) was used as control. Aggregation of HTTEx1Q_{97}-EGFP was quantified by manually counting foci 32 h after transfection from at least 6 frames per condition of three independent biological replicates. In total, at least 700 cells were analyzed for each condition.

In control conditions, 15.5 % of cells showed foci (Fig. 3.13 green bar and upper left image). Upon depletion of DNAJB1 by siRNA, the proportion of cells showing foci increased significantly to 27.6 % (Fig. 3.13 red bar and upper right image). These results are in line with the *in vitro* experiments (Fig. 3.12). When DNAJB1^{wt} was overexpressed, foci formation was reduced and only 10.4 % of the cells contained foci (Fig. 3.13 yellow bar and lower left image), while overexpression of DNAJB1^{H244A} could not suppress HTTEx1Q_{97} aggregation and 31.1 % of the cells showed foci (Fig. 3.13 blue bar and lower right image).

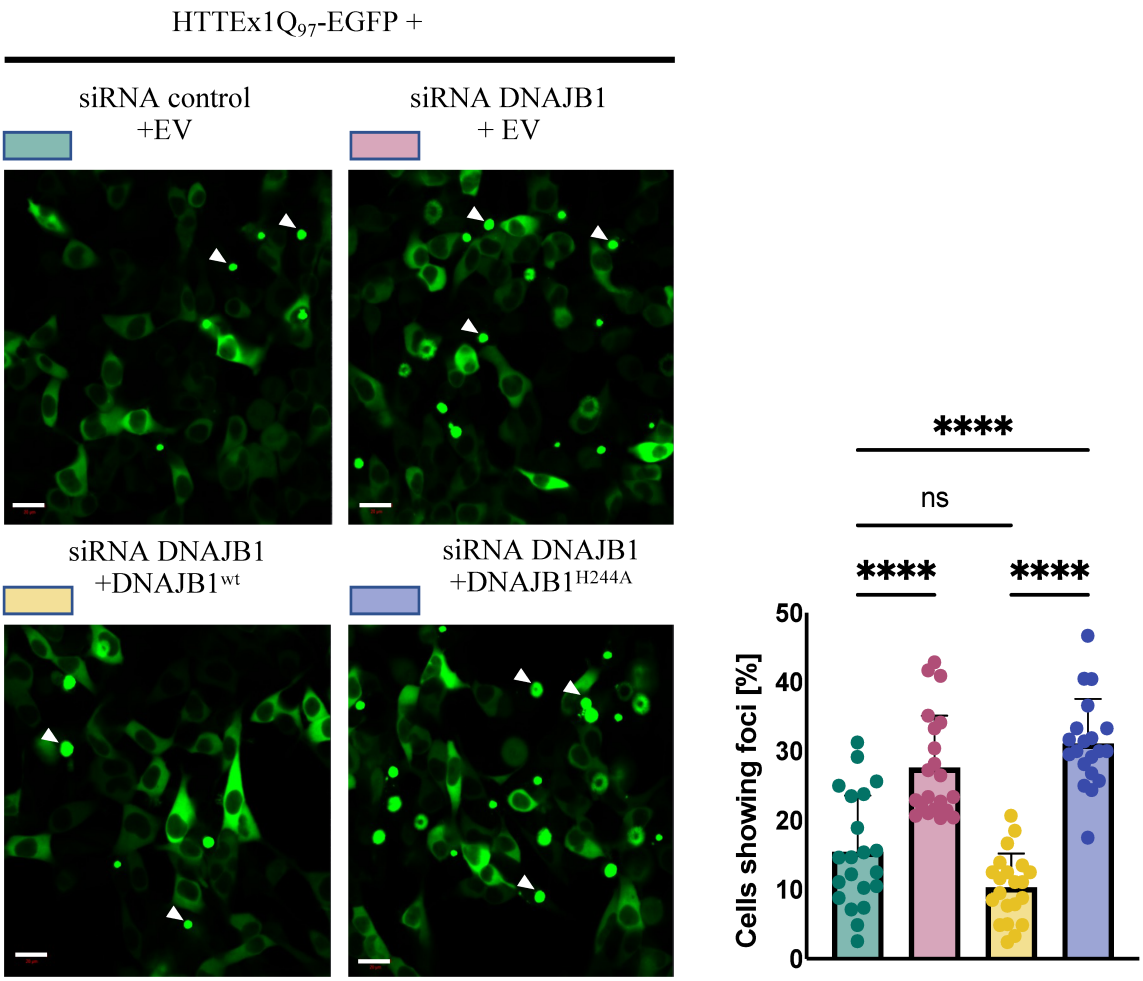

Figure 3.13: Foci quantification of HEK293 cells expressing HTTExon1Q$_{79}$-EGFP

On the left, confocal images of HEK293 cells after expression of HTTExon1Q$_{79}$-EGFP + control siRNA or siRNA against DNAJB1 and concomitant expression of DNAJB1 or DNAJB1^{H244A} for 32 h. On the right, a bar graph is shown depicting the proportion of cells showing HTTExon1Q$_{79}$-EGFP foci. Every dot represents one technical replicate from three independent biological replicates. In total, 703 to 868 cells were analyzed per condition. Bars are representing the mean values with error bars corresponding to the SD. Data were analyzed by a one-way ANOVA. ****p ≤ 0.0001; ns not significant.

To verify the experimental conditions of the depletion and overexpression of DNAJB1, I quantified the DNAJB1 protein levels by western blots. Analogous to the imaging experiments, the cells were harvested and lysed 32 h after transfection. The protein concentrations of the lysates were determined by Bradford assay and 35 µg of protein of each condition were loaded per lane and subjected to SDS-PAGE.
Afterwards, the proteins were blotted onto nitrocellulose membranes and stained with the respective antibodies (Fig. 3.14). The signals of GFP (to detect HTTEx1Q$_{97}$-

EGFP) and DNAJB1 were normalized to the ß-actin signal. Subsequently, the signal intensities were normalized to the DNAJB1 and GFP signal of the control.

When the cells were transfected with siRNA against DNAJB1 and the EV, I observed a reduction of DNAJB1 levels by 30 %. While transfection with siRNA and a concomitant overexpression of DNAJB1^{wt} or DNAJB1^{H244A} resulted in an increase of the DNAJB1 protein levels to 258 % for DNAJB1^{wt} and 261 % for DNAJB1^{H244A}. Thus, the data confirm the experimental conditions and also show that the DNAJB1 protein levels did not differ between wt and H244A mutant. The HTTEx1Q$_{79}$-EGFP levels did not differ significantly between the experimental conditions, except for the cells transfected with siRNA against DNAJB1 and the overexpression vector for DNAJB1^{wt}. There, the HTTEx1Q$_{79}$-EGFP levels were slightly increased (* $p = 0.034$). However, this was actually the condition showing the least foci. On the other hand, the conditions where the foci number was increased, showed no significant increase in the HTTEx1Q$_{79}$-EGFP protein levels indicating, that the increase in aggregation is not caused by an increase in HTTEx1Q$_{79}$-EGFP expression.

These results demonstrate, that depletion of DNAJB1 leads to an increase of HTTEx1Q$_{97}$-EGFP aggregation, that can be rescued by DNAJB1^{wt} overexpression, but not by overexpression of DNAJB1^{H244A} and confirm the results of the FRET-based *in vitro* aggregation assays.

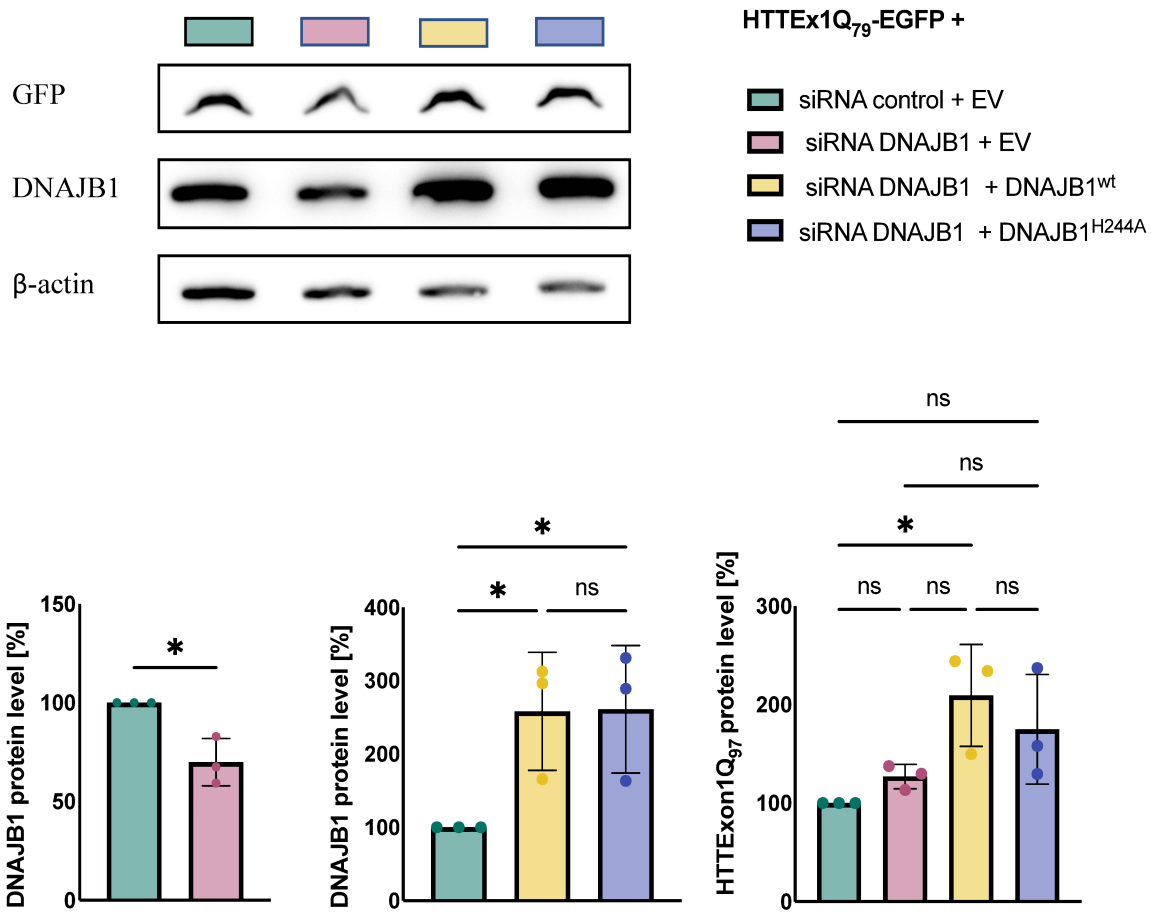

Figure 3.14: Relative quantification of protein levels by western blot

On the top, a representative western blot of three independent experiments is shown. Western blot signals for DNAJB1 and HTTExon1Q$_{97}$-EGFP were normalized to the β-actin signal. On the bottom, bar graphs are depicting the mean values of relative protein levels with error bars corresponding to the SD. Data were analyzed by t-test or one-way ANOVA. *p≤ 0.05; ns not significant.

3.1.6 Deletion of the first proline region of HTTEx1 had no effect on the chaperone-mediated suppression of HTTEx1Q_{48}ΔP1 aggregation

The Huntingtin binding motif of DNAJB1 was mapped to interact with the second proline stretch of the proline rich region by cross-linking mass spectrometry (Ayala Mariscal *et al.*, 2022). To validate the binding site experimentally, FRET based aggregation experiments were performed with a HTTEx1 variant missing the second proline stretch (HTTEx1ΔP2) by my colleague Maria Lucia Pigazzini (Kirstein lab). Hsc70, Apg2 and DNAJB1 were no longer able to suppress aggregation of HTTEx1ΔP2 (Ayala Mariscal *et al.*, 2022).

It was however not known if the first proline stretch of the proline rich domain was part of the binding interface or had an effect on the DNAJB1-HTTEx1 interaction. To test that, a HTTEx1 variant missing the first proline stretch (HTTEx1ΔP1) was analyzed in the FRET-based aggregation assay. It has previously been shown by our lab that a deletion of the first proline stretch of the proline rich domain has an effect on the aggregation propensity of HTTEx1 independently of chaperones (Pigazzini *et al.*, 2021). I could reproduce this and observed a delay in the aggregation onset of HTTEx1Q_{48}ΔP1 with $T_{½}$= 26.2 h (Fig. 3.15 red curve/bar) compared to HTTEx1Q_{48} $T_{½}$= 10.0 h (Fig. 3.15 green curve/bar). To ensure that the aggregation of HTTEx1Q_{48}ΔP1 reaches a plateau, I performed the experiment over a longer time period (60 h). Although the chaperones could not fully suppress HTTEx1ΔP1 aggregation, they were able to delay the onset of aggregation $T_{½}$= 35.2 h (Fig. 3.15 yellow curve/bar).

This led to the conclusion, that while the second proline stretch is crucial for DNAJB1-HTTEx1Q_{48} interaction, the first proline stretch also affects the DNAJB1-HTTEx1Q_{48} interaction. Although this could also be due to conformational changes within HTTEx1Q_{48}ΔP1 compared to HTTEx1Q_{48} and hence rather reflect an indirect effect than presenting a second binding site. This assumption is supported by the different aggregation kinetic of HTTEx1Q_{48}ΔP1 vs HTTEx1Q_{48} (Fig. 3.15 compare red and green curves)

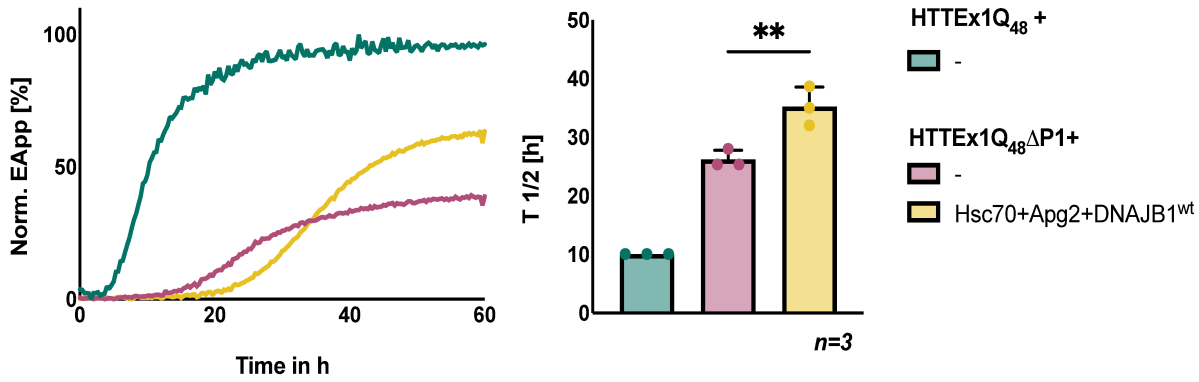

Figure 3.15: Effect of the trimeric chaperone complex on the aggregation of HttEx1Q$_{48}$_ΔP1

HTTExon1Q$_{48}$ or HTTEx1Q$_{48}$ΔP1 aggregation was followed by FRET measurements where an increase in FRET efficiency corresponds to HTTExon1Q$_{48}$/HTTEx1Q$_{48}$ΔP1 fibril formation. The graph on the left is a representative result of three independent experiments and shows the normalized apparent FRET efficiency over time of HTTExQ$_{48}$ alone (green), HttEx1Q$_{48}$ΔP1 alone (red) or HttEx1Q$_{48}$ΔP1 + Hsc70 + Apg2 + DNAJB1^{wt} (yellow). The right graph shows the half-life ($T_{1/2}$) of HTTEx1Q$_{48}$/HTTEx1Q$_{48}$ΔP1 aggregation for each individual experiment. Data were analyzed by a one-way ANOVA. **p ≤ 0.01.

3.2 Analysis of the role of the DNAJB1 orthologue, DNJ-13 on HTTEx1Q$_{48}$ aggregation in *C. elegans*

The *in vitro* experiments have shown that the chaperone complex composed of Hsc70, DNAJB1 and Apg2 is able to suppress HTTEx1Q$_{48}$ aggregation and that DNAJB1 is the limiting factor as demonstrated in the FRET based aggregation assays as well as in cultured HEK293 cells where an overexpression of DNAJB1 alone could reduce HTTEx1Q$_{79}$-EGFP foci formation.
To analyze the role of the J-domain protein on HTT pathology on an organismal level *in vivo,* I used a *C. elegans* model. *C. elegans* possesses orthologs for the three human chaperones of the chaperone complex that I worked with *in vitro*. Namely, HSP-1 for the human Hsc70, HSP-110 for Apg2 and DNJ-13 for DNAJB1. This allowed me to study the same system in the nematode as before *in vitro*. It has been shown, that although *C. elegans* does not have a Huntingtin ortholog, those chaperones can suppress HTTEx1Q$_{48}$ aggregation (Scior *et al.*, 2018). In this thesis, I focused on DNJ-13 and its ability to interact with and interfere with the aggregation of neuronal HTTEx1Q$_{48}$ in the nematode.

To study the effect of DNJ-13 overexpression on HTTEx1Q$_{48}$ aggregation in the nematode, a DNJ-13 overexpression strain, where *dnj-13::yfp* was expressed under the control of the endogenous *dnj-13* promotor was used (Papsdorf, Sacherl and Richter, 2014) and crossed with Huntington´s disease strains. The DNJ-13 overexpression strain will be referred to as DNJ-13.

For the Huntington´s disease strains, HTTEx1Q$_{48}$ and HTTEx1Q$_{48}$ΔP were expressed pan-neuronally in the nematode (Pigazzini *et al.*, 2021). To allow fluorescence microscopy for the detection of the protein and to monitor its aggregation, HTTEx1Q$_{48}$ and HTTEx1Q$_{48}$ΔP were sub-stoichiometrically labelled with codon optimized mScarlet. To archive the sub-stoichiometric labelling, two moieties of HTTEx1Q$_{48}$ or HTTEx1Q$_{48}$ΔP were expressed in a single operon under the control of the pan-neuronal *rgef-1* promotor. The untagged HTTEx1Q$_{48}$ or HTTEx1Q$_{48}$ΔP was translated in a cap-dependent manner, while for the second fluorescently-tagged moiety, translation was driven by a less efficient internal ribosome entry site (IRES) element, resulting in a sub-stoichiometric labelling of the expressed HTTEx1Q$_{48}$ and

HTTEx1Q$_{48}$ΔP moieties (Fig. 3.16 top) (Gallrein *et al.*, 2021; Pigazzini *et al.*, 2021). Although those strains are expressing both, mScarlet tagged and non-tagged HTTEx1Q$_{48}$ and HTTEx1Q$_{48}$ΔP moieties, the strains will be referred to as HTTEx1Q$_{48}$ and HTTEx1Q$_{48}$ΔP for simplicity. HTTEx1Q$_{48}$ΔP was chosen as it is missing the proline rich domain and hence the binding site for DNJ-13. For that, it served as a control as HTTEx1Q$_{48}$ΔP aggregation should not be affected by DNJ-13 overexpression.

mScarlet expressed under the control of the *rgef-1* promotor and the IRES motif alone was used as a control. Also, the mScarlet control strain was crossed with the DNJ-13 overexpression line. Fluorescent microscopy images of all the strains used in this work are shown in Fig. 3.16.

What can be observed in the fluorescent images of the *C. elegans* strains (Fig. 3.16 bottom) is, that DNJ-13 alone is mainly expressed in the tail region of the nematode and much less in other body parts. When the DNJ-13 strain was crossed with the mScarlet control or HTTEx1Q$_{48}$ΔP strain, the expression pattern did not change. Only when the DNJ-13 strain was crossed with the HTTEx1Q$_{48}$ strain, DNJ-13 seemed to be differently expressed. The expression was no longer restricted to the tail region, but DNJ-13 was now also expressed in other tissues and in particular in the head region where it likely interacts with HTTEx1Q$_{48}$. The co-localization was analyzed next. Notably, also the fluorescence intensity of HTTEx1Q$_{48}$-mScarlet is increased in the HTTEx1Q$_{48}$ x DNJ-13 strain.

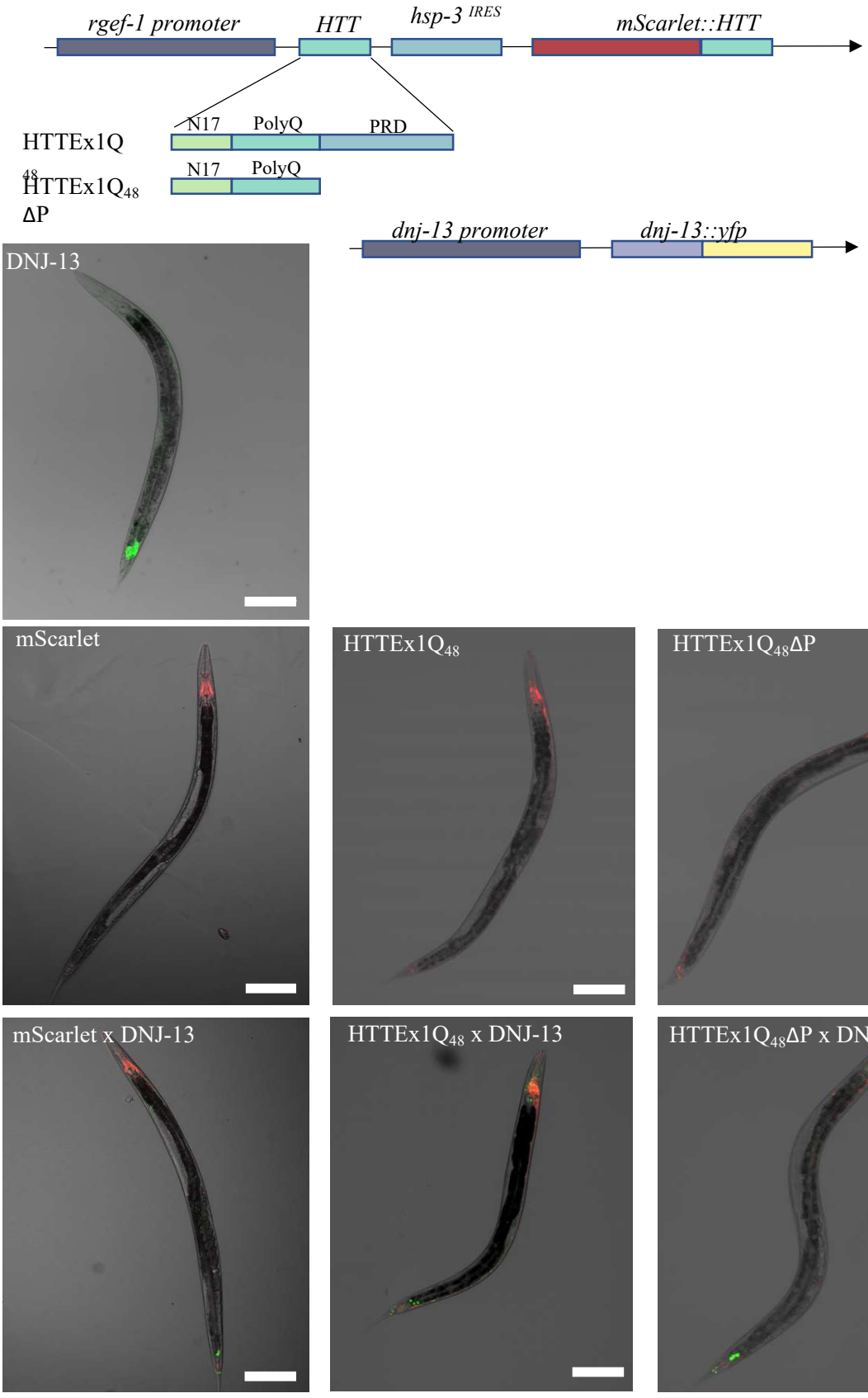
rgef-1 promoter
HTT
hsp-3 IRES
mScarlet::HTT
N17
PolyQ
PRD
HTTEx1Q48
N17
PolyQ
HTTEx1Q48 ΔP
dnj-13 promoter
dnj-13::yfp
DNJ-13
mScarlet
HTTEx1Q48
HTTEx1Q48ΔP
mScarlet x DNJ-13
HTTEx1Q48 x DNJ-13
HTTEx1Q48ΔP x DNJ-13

Figure 3.16: Overview of nematode strains

At the top, schematics of the DNA constructs used for the generation of *C. elegans* strains are shown. In the HTTEx1Q_{48} and HTTEx1$Q_{48}\Delta$P strains, *HTTEx1* is transcribed under the control of the pan-neuronal promotor *rgef-1*. A second fluorescently tagged HTTEx1 moiety is translated in a CAP-independent manner using an IRES element of *hsp-3. dnj-13::yfp* is expressed under the control of the endogenous *dnj-13* promotor. At the bottom, representative confocal images of the whole nematode for each individual *C. elegans* strains are shown and the crossed strains with DNJ-13. Scale bars are 100 µm.

3.2.1 DNJ-13 co-localizes with HTTEx1Q_{48}

To assess the interaction between DNJ-13 with HTTEx1Q_{48} and HTTEx1$Q_{48}\Delta$P, nematodes of the crossed strains HTTEx1Q_{48} x DNJ-13 and HTTEx1$Q_{48}\Delta$P x DNJ-13 were synchronized by egg laying and confocal images of day 4 old nematodes were acquired. For each strain at least ten nematodes were analyzed for co-localization. Images were acquired from the head and tail region. For all images the Pearson´s correlation coefficient r was determined. r can be between with -1 and 1, where a value of -1 indicates total negative correlation and a value of 1 complete positive correlation. Values between 0.3 and 0.5 indicate weak co-localization and values from 0.5 to 0.8 moderate co-localization (Dunn, Kamocka and McDonald, 2011)

Calculating those r values resulted in r= 0.52 for the head region for HTTEx1Q_{48} x DNJ-13 and r= 0.65 for the tail region (Fig. 3.17 a)). These values suggest a moderate co-localization of HTTEx1Q_{48} and DNJ-13 in both, the head and tail region. For HTTEx1$Q_{48}\Delta$P x DNJ-13 the calculated r values were lower: for the head region r= 0.48 and for the tail region r= 0.35 (Fig. 3.17 a)). Those values suggest only a weak co-localization of HTTEx1$Q_{48}\Delta$P and DNJ-13. While the difference in the r value for the head region was not significantly different between the HTTEx1Q_{48} x DNJ-13 and HTTEx1$Q_{48}\Delta$P x DNJ-13, the r value for the tail region showed a significant difference ($p = <0.0001$).

Interestingly, DNJ-13 seemed to mainly co-localize with HTTEx1Q_{48} when it was highly concentrated forming foci/aggregates and seemed to co-localize less if HTTEx1Q_{48}

showed weak/diffuse fluorescence, which becomes better visible in the images of the individual fluorescent channels for HTTEx1Q$_{48}$ x DNJ-13 (Fig. 3.17 b)). Arrowheads are highlighting some of those foci, that were showing red and green fluorescence. The co-localization with the HTTEx1Q$_{48}$ foci suggests that DNJ-13 has a higher affinity to HTT aggregates than to soluble HTT or that the interaction with soluble HTT is too transient. These observations recapitulate *in vitro* obtained data from Merve Özel (Kirstein lab).

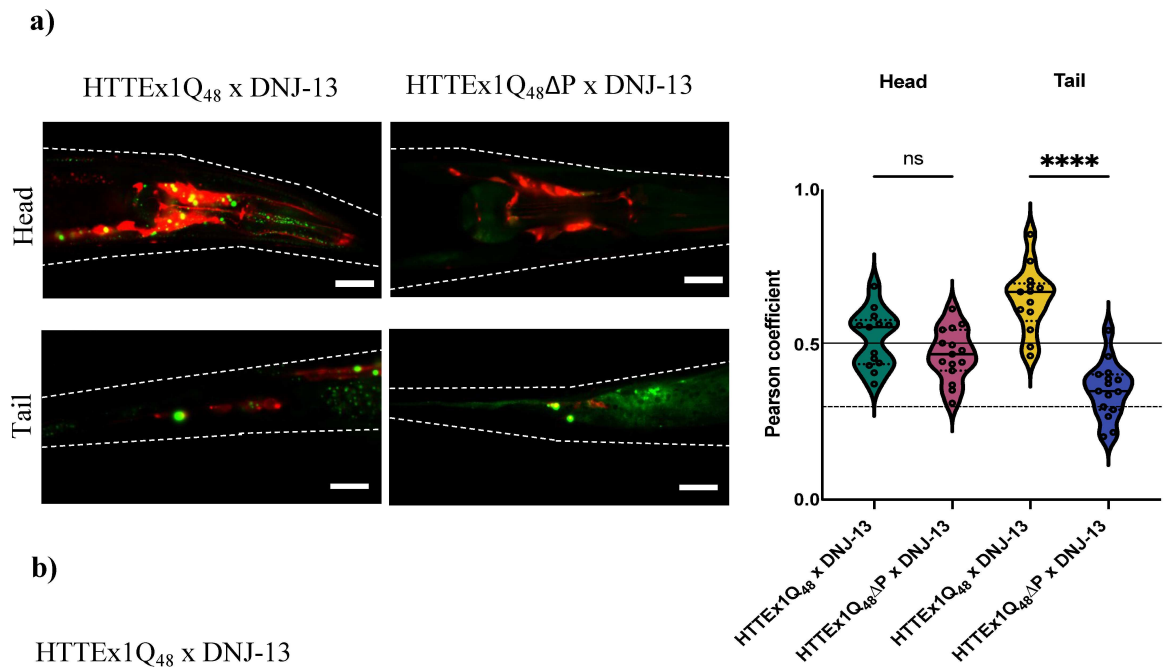

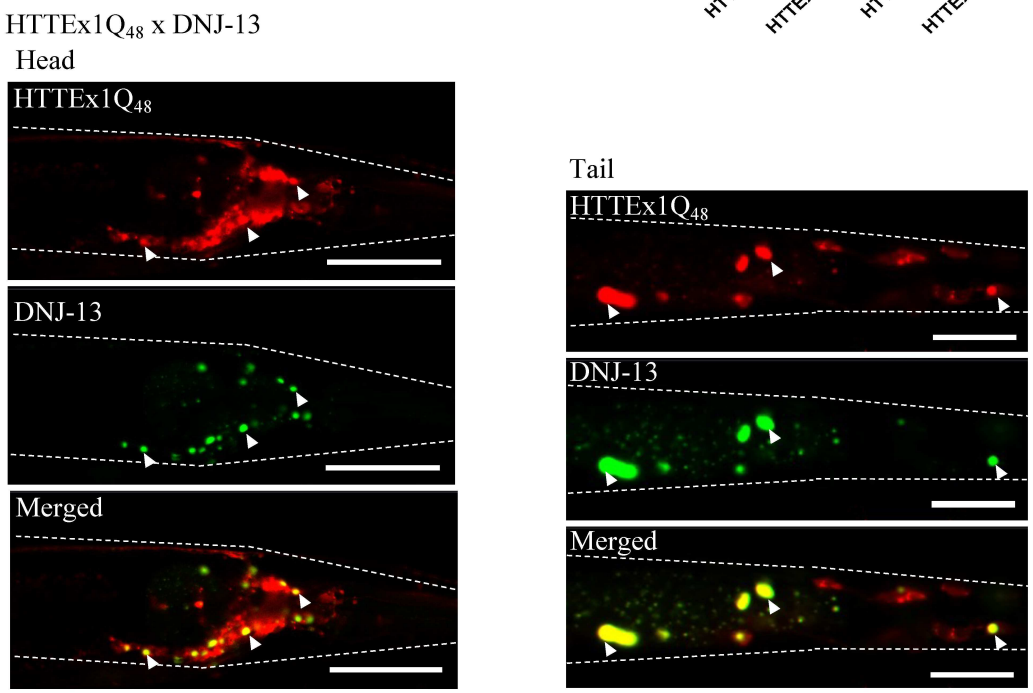

Figure 3.17: Co-localization analysis of HTTEx1Q$_{48}$ or HTTEx1Q$_{48}$ΔP with DNJ-13

a) On the left, representative confocal images of the head and the tail region of HTTEx1Q$_{48}$ or HTTEx1Q$_{48}$ΔP crossed with DNJ-13::YFP (DNJ-13) nematodes are shown. Red fluorescence shows HTTEx1Q$_{48}$ expression (due to mScarlet tag) while green fluorescence shows DNJ-13 expression (fused with YFP). Scale bars are 20 µm. On the right, a violin plot shows the Pearson's correlation coefficient between HTTEx1Q$_{48}$ and DNJ-13 for the head and tail region of each cross. Positive values indicate co-localization, while negative values would indicate no co-localization. Values below 0.3 (dashed line) indicate weak co-localization and values above 0.5 (solid line) indicate moderate co-localization. Data were analyzed by a t-test, **** $p \leq 0.0001$; ns not significant. **b)** Representative confocal images of individual and merged fluorescent channels for HTTEx1Q$_{48}$ x DNJ-13 of the head and tail region. Arrowheads highlight areas of co-localization in the merged and individual fluorescent channels. Scale bars for the head region are 50 µm and 20 µm for the tail region.

Taken together and as expected, DNJ-13 co-localized stronger with HTTEx1Q$_{48}$ than with HTTEx1Q$_{48}$ΔP. Next, I analyzed the effect of DNJ-13 overexpression on the aggregation of HTTEx1Q$_{48}$ in *C. elegans* by fluorescence-lifetime imaging microscopy (FLIM).

3.2.2 DNJ-13 overexpression leads to increased aggregation of HTTEx1Q$_{48,}$ but not of HTTEx1Q$_{48}$ΔP

To quantify aggregation and be able to compare the aggregation propensity between strains, time-correlated single photon counting fluorescence lifetime microscopy (TCSPC-FLIM) was employed. FLIM measurements will give the fluorescent lifetime (tau, τ) in nanoseconds (ns) as a readout. Each fluorophore has a defined tau value, that is only affected by changes of the surrounding environment or structural properties, but not by its concentration (Becker, 2012). FLIM has already been established to distinguish between soluble, oligomeric and aggregated species of aggregation prone proteins like Huntingtin, α-synuclein and Aβ_{1-42} in *C. elegans* (Kaminski Schierle *et al.*, 2011; Laine *et al.*, 2019; Gallrein *et al.*, 2021; Pigazzini *et al.*, 2021).

An aggregation of HTTEx1 would result in a decrease in tau values of the fused mScarlet protein due to molecular quenching of the β-sheets of HTTEx1Q_{48} upon their fibrilization. For that, the tau values can be directly correlated to the aggregation propensity. FLIM measurements were performed at day 4 (young adults) and day 7 (older animals) of the nematodes` life, for the mScarlet control, HTTEx1Q_{48}, and HTTEx1$Q_{48}\Delta$P strains as well as for the DNJ-13 overexpression crosses.

The tau value for mScarlet in the neurons of day 4 old nematodes was 2.89 ns and the nematodes showed no aggregates, which would be visualized in blue in the color coded FLIM images (Fig. 3.18). When mScarlet was crossed with the DNJ-13 overexpression strain, no effect on the tau value was observed (2.93 ns). At day 4, also the HTTEx1Q_{48} strain showed no aggregates yet and had a tau value of 2.88 ns, which did not differ significantly from the mScarlet control (Fig. 3.19 top). However, the HTTEx1Q_{48} x DNJ-13 cross showed strong aggregation already at day 4 with a tau value of 2.76 ns, which was significantly lower than the one for HTTEx1Q_{48} ($p=<0.0001$). Contrary to the cell culture experiments, DNJ-13 overexpression seemed to increase the aggregation propensity of HTTEx1 in the nematode. The distribution of the tau values is depicted in a histogram, where the tau values were plotted against the frequency (Fig. 3.18 below each representative FLIM image the respective histogram is shown). The histogram for HTTEx1Q_{48} x DNJ-13 only showed a slight shift towards lower tau values in general when compared to the one of HTTEx1Q_{48}, but the abundance of species with tau values between 2.0 ns and 2.5 ns was increased noticeably. Therefore, the individual histogram shows a shoulder and no gaussian distribution. For HTTEx1$Q_{48}\Delta$P, the tau values were overall lower with 2.73 ns, but here the HTTEx1$Q_{48}\Delta$P x DNJ-13 cross showed no significant difference compared to HTTEx1$Q_{48}\Delta$P with a tau value of 2.70 ns (Fig. 3.19). In both strains, aggregates can be observed already at day 4 and are depicted as dark blue spots in the color coded FLIM images (Fig. 3.18).

These results, are in line with previous studies that have shown that the proline rich domain has a protective role against aggregation of HTTEx1 and deleting it, results in an increase of aggregation (Dehay and Bertolotti, 2006; Gruber *et al.*, 2018; Pigazzini *et al.*, 2021). That the overexpression of DNJ-13 had no effect on the aggregation

propensity of HTTEx1Q$_{48}$ΔP can be interpreted as a result of the missing proline rich domain and therefore the absence of the binding site for DNJ-13.

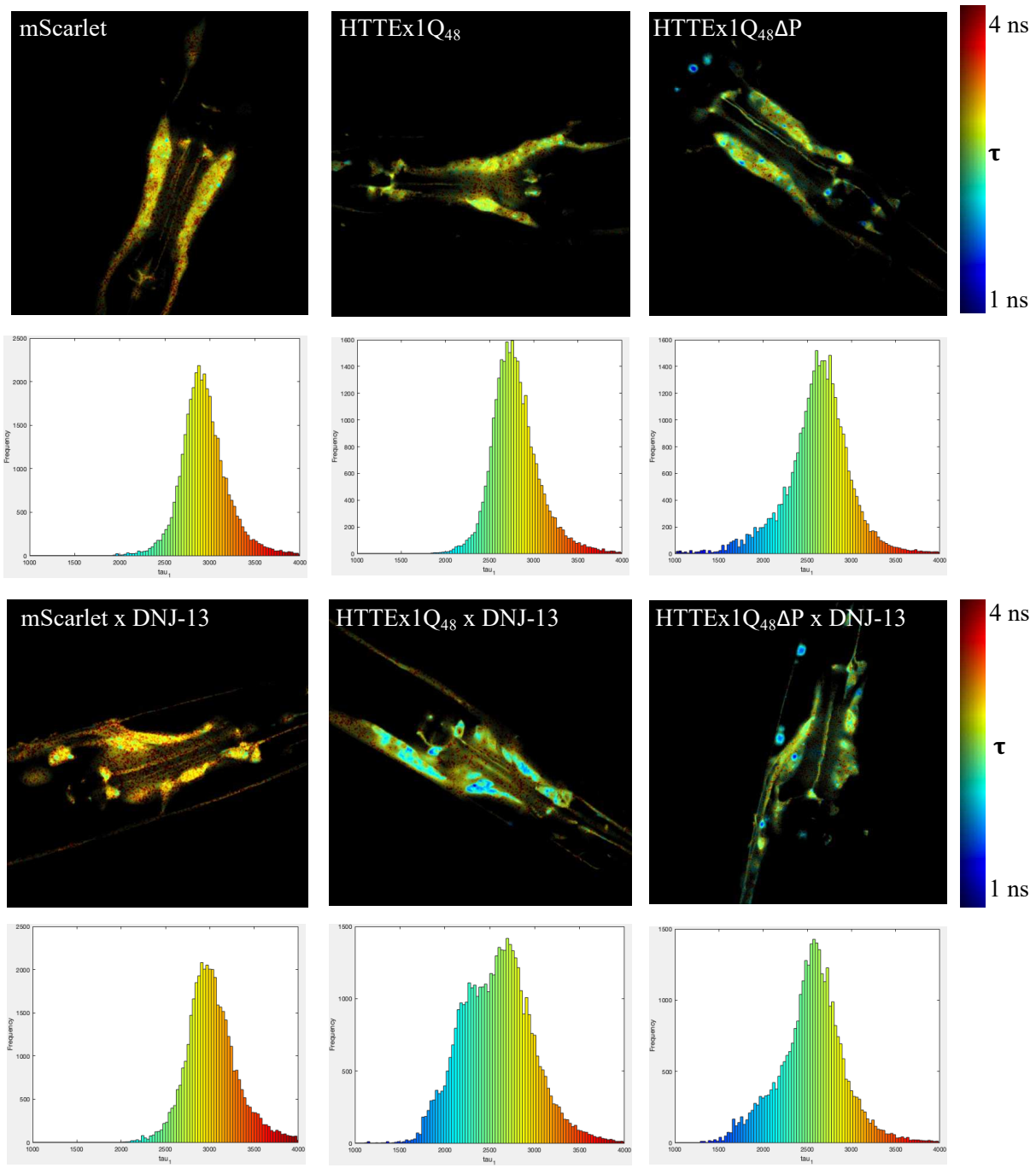

Figure 3.18: Detection of aggregation of HTTEx1Q$_{48}$ or HTTEx1Q$_{48}$ΔP in four days old nematodes in the neurons by using FLIM

Representative confocal TCSPC images of the head region of four days old nematodes of the indicated strains. The fluorescence lifetime is false color coded, from blue → short fluorescent lifetime (=aggregated protein) to red → long fluorescence lifetime (soluble protein). Underneath each image, the respective histogram is depicted showing the frequency of pixels with a certain fluorescence lifetime (tau).

The histogram of a representative data set of HTTEx1Q$_{48}$ x DNJ-13 showed an increase in the HTTEx1 species with tau values between 2.0 and 2.5 ns compared to HTTEx1Q$_{48}$. To corroborate these data, I analyzed the histograms of all animals of the analyzed strains, HTTEx1Q$_{48}$, HTTEx1Q$_{48}$ x DNJ-13, HTTEx1Q$_{48}$ΔP and HTTEx1Q$_{48}$ΔP x DNJ-13. The histogram depicting the average of over 30 nematodes for HTTEx1Q$_{48}$ x DNJ-13 (Fig. 3.18 bottom left, blue) was overlaid with the one of HTTEx1Q$_{48}$ (Fig. 3.18 bottom left, dashed line). Again, an increase in abundance of species with a tau value between 2.0 ns and 2.5 ns could be observed. As this histogram is depicting the average of over 30 nematodes, the curve is smoother compared to the one of the individual nematodes (Fig.3.18). For HTTEx1Q$_{48}$ΔP x DNJ-13 (Fig. 3.19 bottom right, orange) and HTTEx1Q$_{48}$ΔP (Fig. 3.19 bottom right, dashed line) the two histograms were nearly completely overlapping and no such difference was observed.

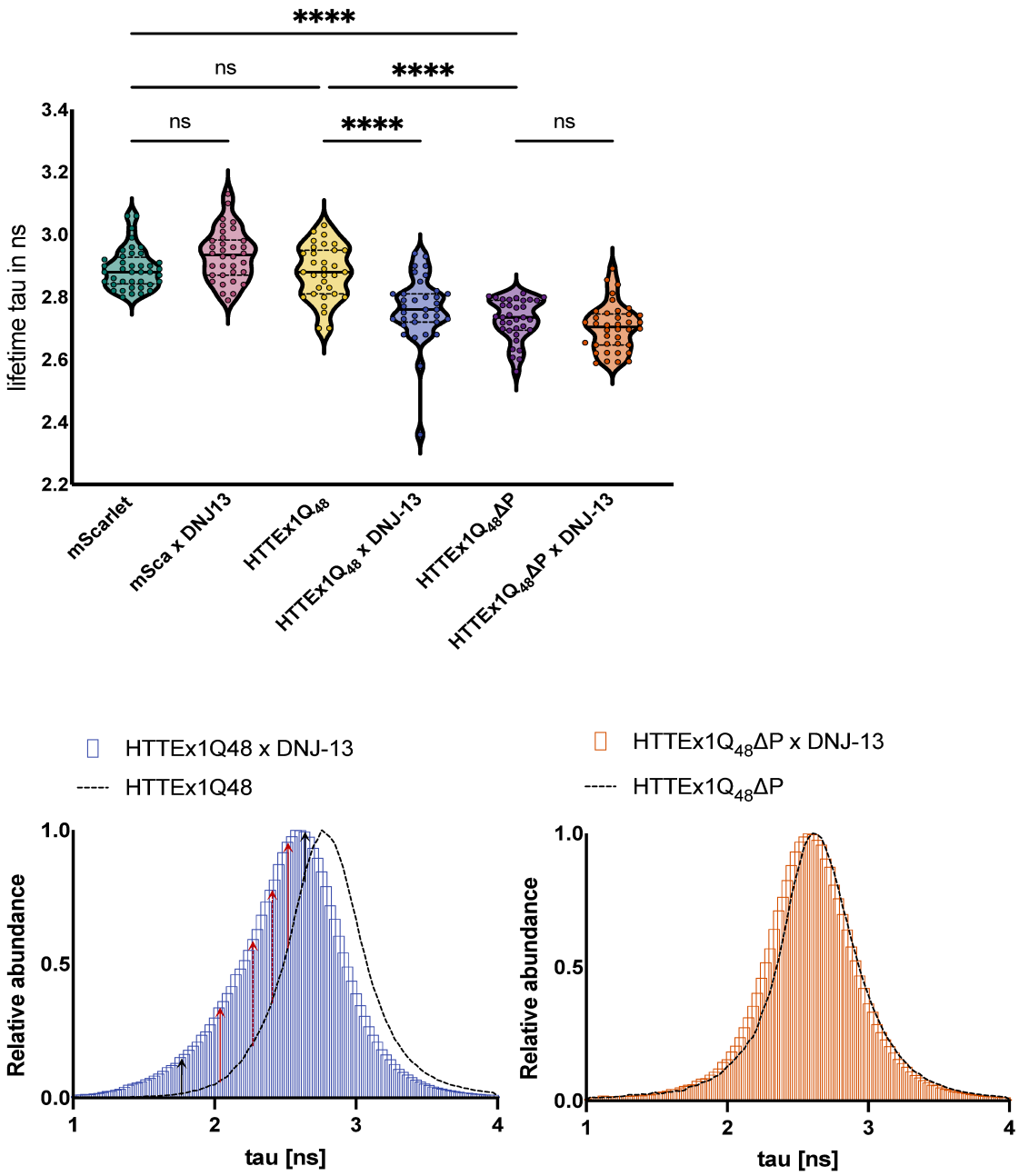

Figure 3.19: FLIM data analysis Day 4

Violin plot at the top shows the average fluorescent lifetime for the head neurons of nematodes expressing mScarlet, HTTEx1Q$_{48}$ or HTTEx1Q$_{48}$ΔP on day 4 of the nematodes' life. From each strain, at least 30 nematodes were analyzed, each circle represents one individual nematode. Nematodes were derived from three independent biological replicates. The median is shown by a solid line, while quartiles are depicted by dotted lines. Data were analyzed by a one-way ANOVA followed by a Bonferroni post hoc test. ****p ≤ 0.0001; ns not significant. At the bottom, histograms, which depict the relative abundance of tau values for all nematodes analyzed of the respective strains are shown. Red arrows highlight the increase in abundance of tau values from 2.1 ns to 2.5 ns in the HTTEx1Q$_{48}$ x DNJ-13 strain compared to HTTEx1Q$_{48}$.

With the start of the reproductive phase it has been found that the proteostasis capacity is declining in *C. elegans* (Labbadia and Richard I. Morimoto, 2015). To investigate if the effect of DNJ-13 overexpression persists in older animals, FLIM measurements were performed in day 7 old nematodes for the same strains as before.

At an advanced age, the proteostasis network is already compromised and I expected more HTT aggregates as on day4 (young adult animals). Indeed, day 7 old nematodes showed more aggregates which are depicted by blue colored areas in the FLIM images (Fig. 3.20). The tau values for the control strains expressing non aggregation prone mScarlet was hardly affected with a tau value of 2.86 ns for mScarlet (data were obtained by my colleague Franziska Hirsch) and 2.87 ns for mScarlet x DNJ-13 at day 7 compared to 2.89 and 2.93 ns at day 4 (Fig. 3.21 violin blot at the top). In all the Huntingtin strains the fluorescent life time decreased significantly ($p = <0.0001$) compared to the measurements at day 4. For HTTEx1Q_{48} the tau value was decreased by 0.2 ns to a tau value of 2.68 ns. For the HTTEx1Q_{48} x DNJ-13 cross the tau value was decreased by 0.18 ns to a tau value of 2.59 ns. For HTTEx1$Q_{48}\Delta$P and the HTTEx1$Q_{48}\Delta$P x DNJ-13 cross the tau values were decreased by 0.18 and 0.15 ns resulting in a tau value of 2.55 ns for both the strains at day 7 (Fig. 3.21 violin blot at the top). When analyzing the histograms for the individual FLIM measurements the shoulder observed in the histogram of HTTEx1Q_{48} x DNJ-13 strain at day 4 could be no longer observed on day 7. Although, the difference in the average tau values between the HTTEx1Q_{48} and HTTEx1Q_{48} x DNJ-13 strain did not change with 0.1 ns on both days. Overlaying all histograms of both the strains for day7 revealed that the decrease in the tau value in the cross on day 4 was mainly due to an increase of HTTEx1Q_{48} species with shorter fluorescence lifetime, whereas at day 7 it derives from a decrease of HTTEx1Q_{48} species with a longer fluorescent lifetime (Fig. 3.21 histogram at the bottom left). For the HTTEx1$Q_{48}\Delta$P and HTTEx1$Q_{48}\Delta$P x DNJ-13 cross, also at day 7 the two histograms were nearly completely overlapping and no such difference was observed (Fig. 3.21 histogram at the bottom right). Thus, also on day 7 DNJ-13 overexpression leads to an increase in HTTEx1Q_{48} aggregation and does not affect the aggregation propensity of HTTEx1$Q_{48}\Delta$P.

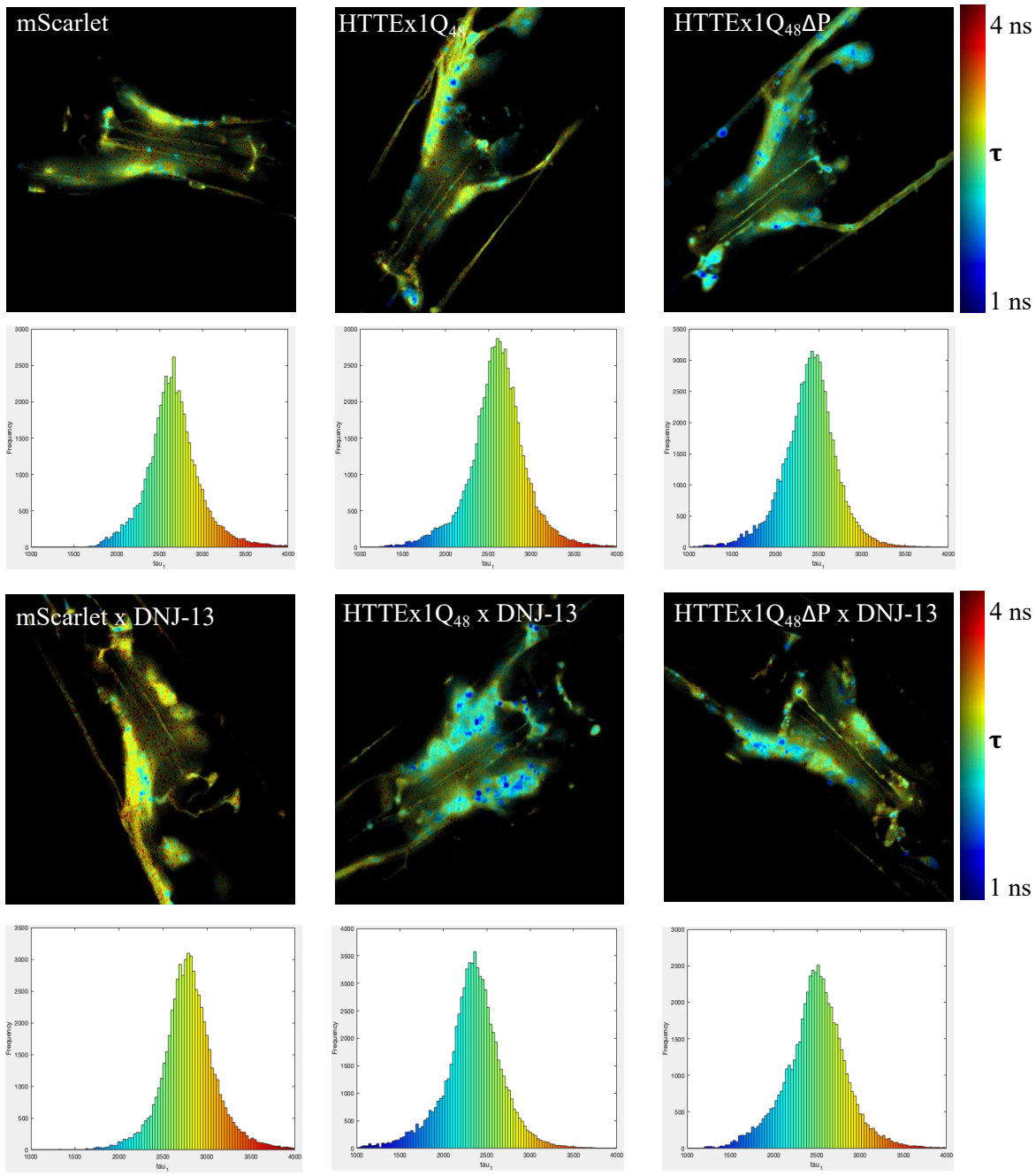

Figure 3.20: Detection of aggregation of HTTEx1Q$_{48}$ or HTTEx1Q$_{48}$ΔP in seven days old nematodes in the neurons by using FLIM

Representative confocal TCSPC images of the head region of seven days old nematodes of the indicated strains. The fluorescence lifetime is false color coded, from blue → short fluorescent lifetime (= aggregated protein) to red → long fluorescence lifetime (= soluble protein). Underneath each image, the respective histogram is depicted showing the frequency of pixels with a certain fluorescence lifetime (tau).

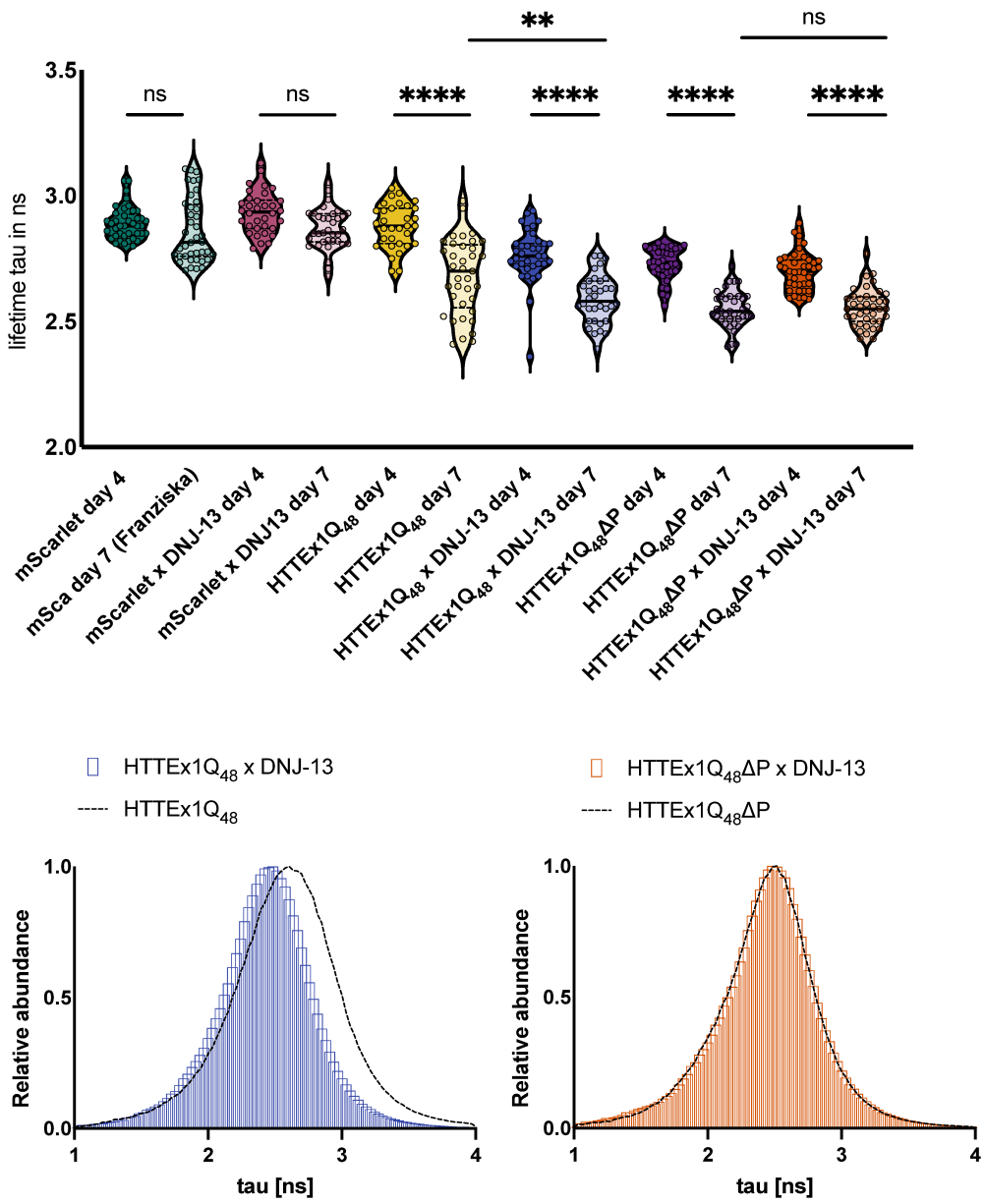

Figure 3.21: FLIM data analysis day 4 and 7 comparison:

Violin plot at the top shows the average fluorescent lifetime from the head neurons of nematodes expressing mScarlet, HTTEx1Q48 or HTTEx1Q48ΔP on day 4 and day 7 of the nematodes' life. From each strain at least 30 nematodes were analyzed, each circle represents one individual nematode. Nematodes were derived from three independent biological replicates. The median is shown by a solid line, while quartiles are depicted by dotted lines. Data were analyzed by a one-way ANOVA followed by a Bonferroni post hoc test. ****p ≤ 0.0001; **p ≤ 0.01; ns not significant. At the bottom, histograms, which depict the relative abundance of tau values for all nematodes analyzed of the respective strains at day 7 are shown.

3.2.3 DNJ-13 overexpression compromises organismal fitness

As the FLIM measurements have shown, DNJ-13 overexpression led to an increase in HTTEx1 aggregation in the HTTEx1Q_{48} strain (Fig. 3.18 - 3.21). To investigate whether this increase in aggregation also had an effect on the organismal fitness of the nematodes, fecundity assays were performed. Nematodes were synchronized by egg laying and when they reached the L4 stage, they were separated onto individual plates. From then on, they were transferred to new plates every day until the end of their reproductive phase. The viable offspring was counted every day and summed up (Fig. 3.22). For the mScarlet strain, the fertility was not different from the wt control, indicating that expression of the fluorophore alone had no effect on the organismal fitness. Also, the HTTEx1Q_{48} strain showed no decrease in fertility compared to the control strains, while HTTEx1$Q_{48}\Delta$P showed a significant reduction in the number of viable offspring. Those results were mainly in line with previously published data (Pigazzini *et al.*, 2021) were there was also no difference detected between the mScarlet control and HTTEx1Q_{48}. Although, there was no significant reduction in the offspring of HTTEx1$Q_{48}\Delta$P observed compared to the control while here the number of viable offspring was reduced.

These results I obtained from the fecundity assay indicate that the increase in aggregation observed in the FLIM measurements can be correlated to the organismal fitness. Notably, HTTEx1Q_{48} x DNJ-13 showed a significant reduction in the number of viable offspring compared to HTTEx1Q_{48}, while the viable offspring of the HTTEx1$Q_{48}\Delta$P x DNJ-13 cross did not differ significantly from the one of HTTEx1$Q_{48}\Delta$P. Interestingly, the number of viable offspring of the DNJ-13 strain was significantly reduced compared to the wt, indicating that the overexpression of DNJ-13 in general had a negative effect on the organismal fitness independent of Huntingtin. Although, if the decrease in the number of viable offspring would be only due to the additive effect of DNJ-13 overexpression and HTTEx1 aggregation one would expect the HTTEx1$Q_{48}\Delta$P x DNJ-13 strain to be most impaired. However, this is not the case, as outlined by comparing the viable offspring of HTTEx1Q_{48} x DNJ-13 and HTTEx1$Q_{48}\Delta$P x DNJ-13 that shows that it is significantly lower for the HTTEx1Q_{48} x DNJ-13 strain ($p=<0.01$) (Fig. 3.22).

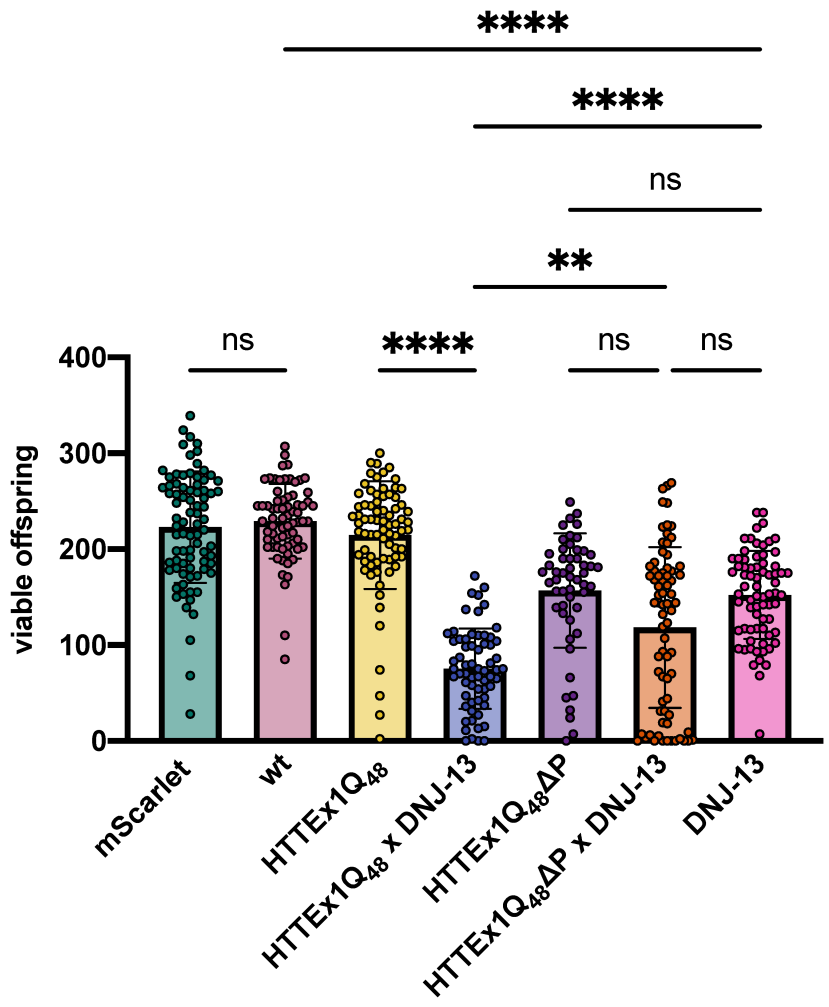

Figure 3.22: Fecundity assay

Bar graph depicting the mean of the viable offspring of the indicated nematode strains with error bars showing the SD. Each dot represents the offspring of one individual nematode. Three independent experiments with at least 20 animals each were performed for all strains. Data were analyzed by a one-way ANOVA followed by a Bonferroni post hoc test. **p ≤ 0.01; ****p ≤ 0.0001; ns not significant.

3.3 Condensation of HTTEx1

It has been recently established that HTTEx1 can undergo liquid-liquid phase separation (Peskett *et al.*, 2018) and this was discussed to be a possible aggregation mechanism. In which liquid-liquid phase separation of HTTEx1 leads to locally increased concentration of HTTEx1 in the condensed phase and promotes aggregation by a liquid-to-solid phase transition. I wanted to investigate if the condensation process of HTTEx1 is affected by the PolyQ flanking regions and how chaperones can modulate liquid-liquid phase separation of HTTEx1.

3.3.1 Liquid-liquid phase separation of HTTEx1 and HTTEx1 variants

In a first step, I established liquid-liquid phase separation of HTTEx1 in our lab. For that, GST-HTTEx1Q_{23}-YPet was expressed in *E. coli* and purified by affinity chromatography. The GST-tag was cleaved on the column resulting in HTTEx1Q_{23}-YPet as the final purification product. Mixing 50 µM of the purified protein with 10% Dextran as a crowding reagent resulted in induction of liquid-liquid phase separation.

To assess droplet maturation, confocal images were taken over time (Fig. 3.23a). As liquid-liquid phase separation is no stable state, droplets constantly undergo changes. While the ratio of proteins between the condense and dilute phase always remains stable under a certain condition, droplets start to grow in size over time. This is due to two processes. One is the Ostwald ripening (Shepilov 1992; Brangwynne 2013; Babinchak and Surewicz 2020). Larger droplets are more stable than smaller ones. Proteins from smaller, dissolving droplets move into larger droplets. This results in a growth of droplet size. Additionally, as the droplets are liquid, they can fuse with each other resulting in larger droplets as well (Babinchak and Surewicz 2020). This leads to the increase in size observed for HTTEx1Q_{23}-YPet over the course of 30 min (Fig. 3.23a). Notably, over time the morphology of the droplets changed and they appeared to become hollow, indicating a liquid to solid phase transition.

As liquid-liquid phase separation of HTTEx1 has been shown to depend on hydrophobic interaction and hence can be disturbed by addition 3.3 % of hexanediol, addition of hexanediol would be expected to reverse liquid-liquid phase separation and by that only solid structures would remain. Indeed, addition of 3.3 % of hexanediol 35 min after initiation of liquid-liquid phase separation could not reverse condensation, indicating that a liquid to solid phase separation had taken place over the time of 35 min (Fig. 3.23b).

a)

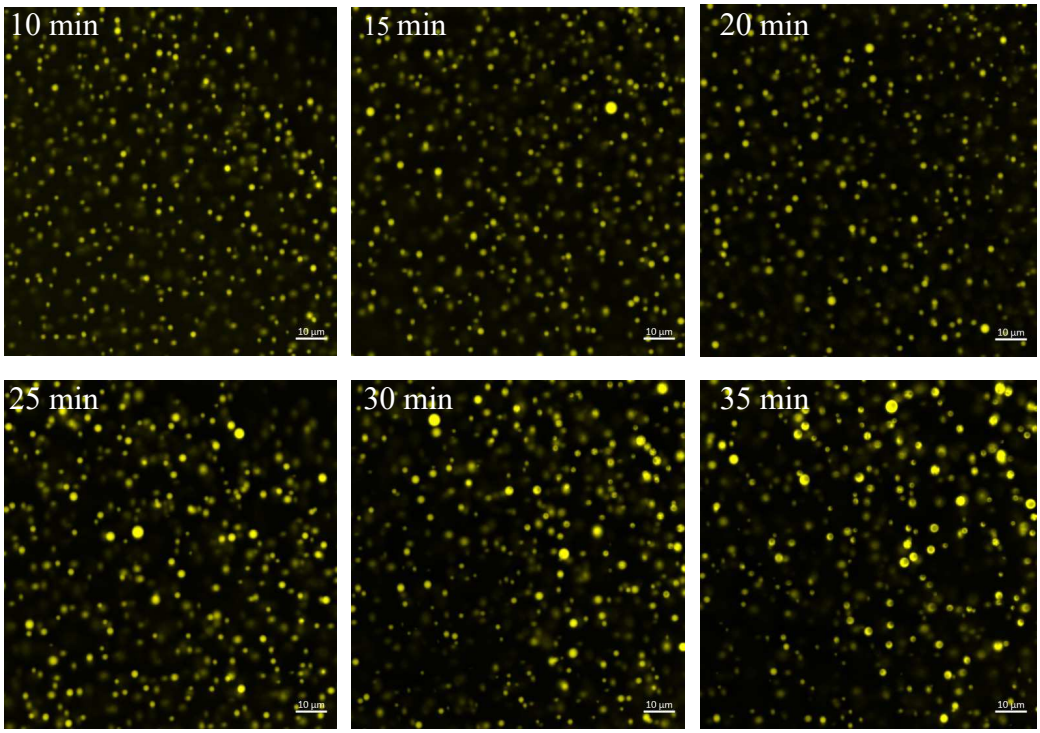

b)

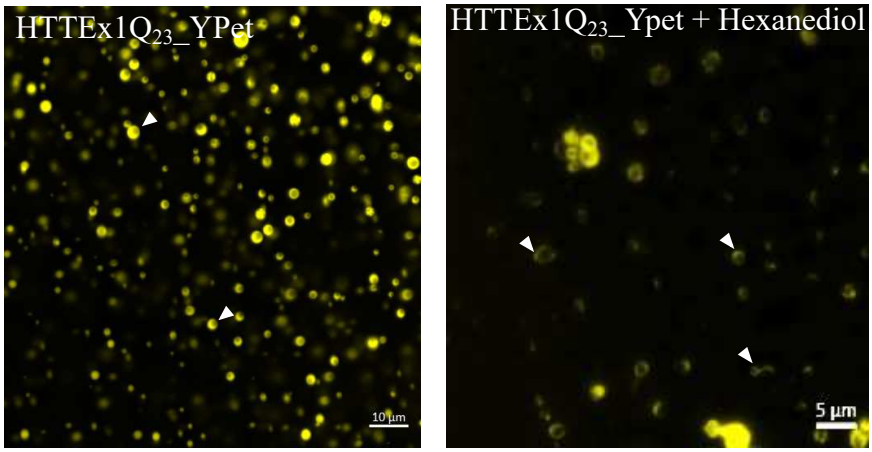

Figure 3.23: Liquid-liquid phase separation of HTTEx1Q$_{23}$

a) Confocal images of droplet formation and droplet maturation of 50 µM HTTEx1Q$_{23}$_YPet in LLPS buffer with 10% Dextran. Scale bars are 10 µm. **b)** On the left, confocal image of HTTEx1Q$_{23}$_YPet droplets after 35 min and on the right after addition of 3.3 % hexanediol. Scale bars are 10 µm and 5 µm.

To assess how the PolyQ flanking regions affect liquid-liquid phase separation of HTTEx1, different HTTEx1 variants were expressed in *E. coli* and purified. While establishing liquid-liquid phase separation of HTTEx1Q$_{23}$-YPet I observed that upon induction of phase separation the droplet formation led to an increase of turbidity so it was used to quantify droplet formation.

To determine turbidity, the absorbance was measured at 595 nm over a time course of 60 minutes. The proteins were expressed without a fluorophore so it would not interfere with the absorbance measurement, but like other phase separating proteins, HTTEx1 becomes very sticky without a tag, so I was not able to purify it without any tag. When I tried to cleave the GST-tag, HTTEx1 got stuck on the column. For that reason, the GST-tagged HTTEx1 proteins were used.

It was hypothesized that the PolyQ flanking regions might have an effect on the liquid-liquid phase separation behavior of HTTEx1 as it has been previously shown, that the N17 region promotes aggregation of HTTEx1 and deletion of it reduced the aggregation propensity while the proline rich domain was found to delay aggregation. (Bhattacharyya *et al.*, 2006; Dehay and Bertolotti, 2006; Arndt, Chaibva and Legleiter, 2015; Pigazzini *et al.*, 2021; Vieweg *et al.*, 2021). If the same principles apply in phase separation depletion of the N17 region would be expected to result in less droplet formation while deletion of the proline rich domain would be expected to facilitate droplet formation.

When taking confocal images GST-HTTEx1Q$_{23}$ seemed to show the same droplet size and formation as HTTEx1Q$_{23}$-YPet, although here only 25 µM of protein were used to slow down droplet maturation and growth as otherwise I was not able to observe the initial increase (Fig. 3.24). GST-HTTEx1Q$_{23}$ΔN17 showed no phase separation under those conditions and so, no increase in turbidity was observed over time (Fig. 3.24; red curve/bar). GST-HTTEx1Q$_{23}$ΔP showed a smaller droplet size compared to GST-

HTTEx1Q_{23} and always had a lag phase in the beginning that was not observed for the other variants. This lag phase could be also observed at the confocal laser scanning microscope as the droplets only started to form after some time, although overall the number of droplets seemed to be increased, which resulted in an increased turbidity (Fig. 3.24; yellow curve/bar) compared to GST-HTTEx1Q_{23} (Fig. 3.24; green curve/bar). Elongating the proline rich domain resulted in smaller droplets for GST-HTTEx1Q_{23}P+ compared to GST-HTTEx1Q_{23} and GST-HTTEx1Q_{23}ΔP. Although in the end, the turbidity was significantly higher for GST-HTTEx1Q_{23}P+ than for GST-HTTEx1Q_{23}, initially GST-HTTEx1Q_{23}P+ showed less turbidity (Fig. 3.24; blue curve/bar).

These results are in general complementary to and in agreement with previous FRET based aggregation experiments, where the deletion of the proline rich domain resulted in a faster aggregation while the deletion of the N17 region delayed aggregation (Pigazzini et al. 2021).

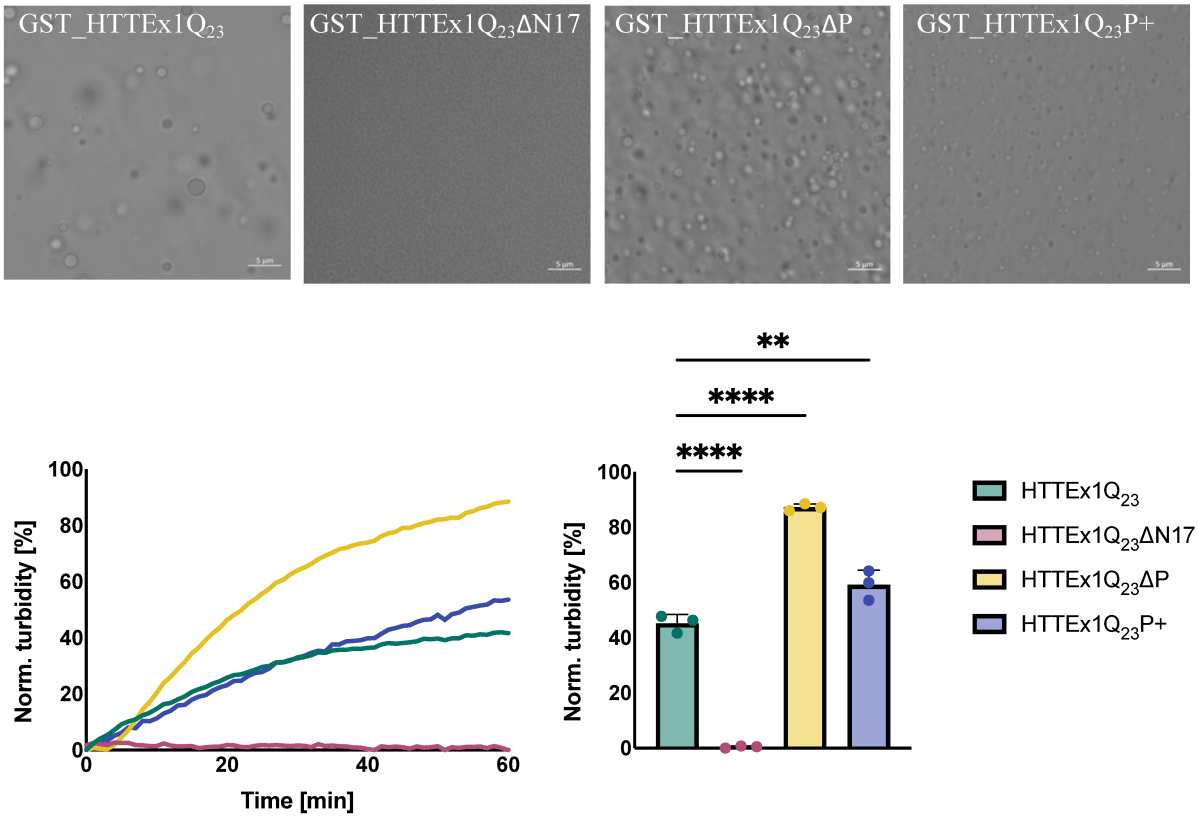

Figure 3.24: Turbidity assay for relative quantification of liquid-liquid phase separation of HTTEx1 variants

At the top, confocal images of 25 µM GST-tagged HTTEx1 variants in LLPS buffer with 10% GST after 30 min are shown. Scale bars are 5 µm. At the bottom, the graph on the left is a representative result of three independent experiments and shows the normalized turbidity in % over time of GST-HTTQ$_{23}$ variants. The right graph shows the average normalized turbidity after 1 h. Data were analyzed by a one-way ANOVA.

3.3.2 Liquid to solid phase transition of HTTEx1Q$_{23}$ and HTTEx1Q$_{23}$ΔP

As the change in morphology and the hexanediol tolerance of the HTTEx1Q$_{23}$-YPet droplets over time indicated liquid to solid phase transition, this was further investigated by fluorescence recovery after photobleaching (FRAP) experiments.
From here on, also the HTTEx1Q$_{23}$ΔP variant was studied as it showed the most prominent increased in turbidity compared to HTTEx1Q$_{23}$ and would be interesting to further study the interaction with chaperones and by that complement the *in vitro* data of the FRET experiments and the *in vivo C. elegans* data. For both, HTTEx1Q$_{23}$-YPet and HTTEx1Q$_{23}$ΔP a change in morphology was observed over time (Fig. 3.25).

When FRAP measurements were performed, droplets were partially bleached and the fluorescent recovery was monitored for 2 min (Fig. 3.25). In the beginning, 10 min after addition of 10 % Dextran, the fluorescence recovery was ~80 % for HTTEx1Q$_{23}$-YPet and HTTEx1Q$_{23}$ΔP. 40 min after addition of 10 % Dextran, the fluorescence recovery was reduced to ~40 % for both. So, although there seemed to be an increase in the condensate formation for HTTEx1Q$_{23}$ΔP compared to HTTEx1Q$_{23}$, this seemed to have no effect on the liquid to solid phase transition since the FRAP measurements showed no difference between HTTEx1Q$_{23}$-YPet and HTTEx1Q$_{23}$ΔP.

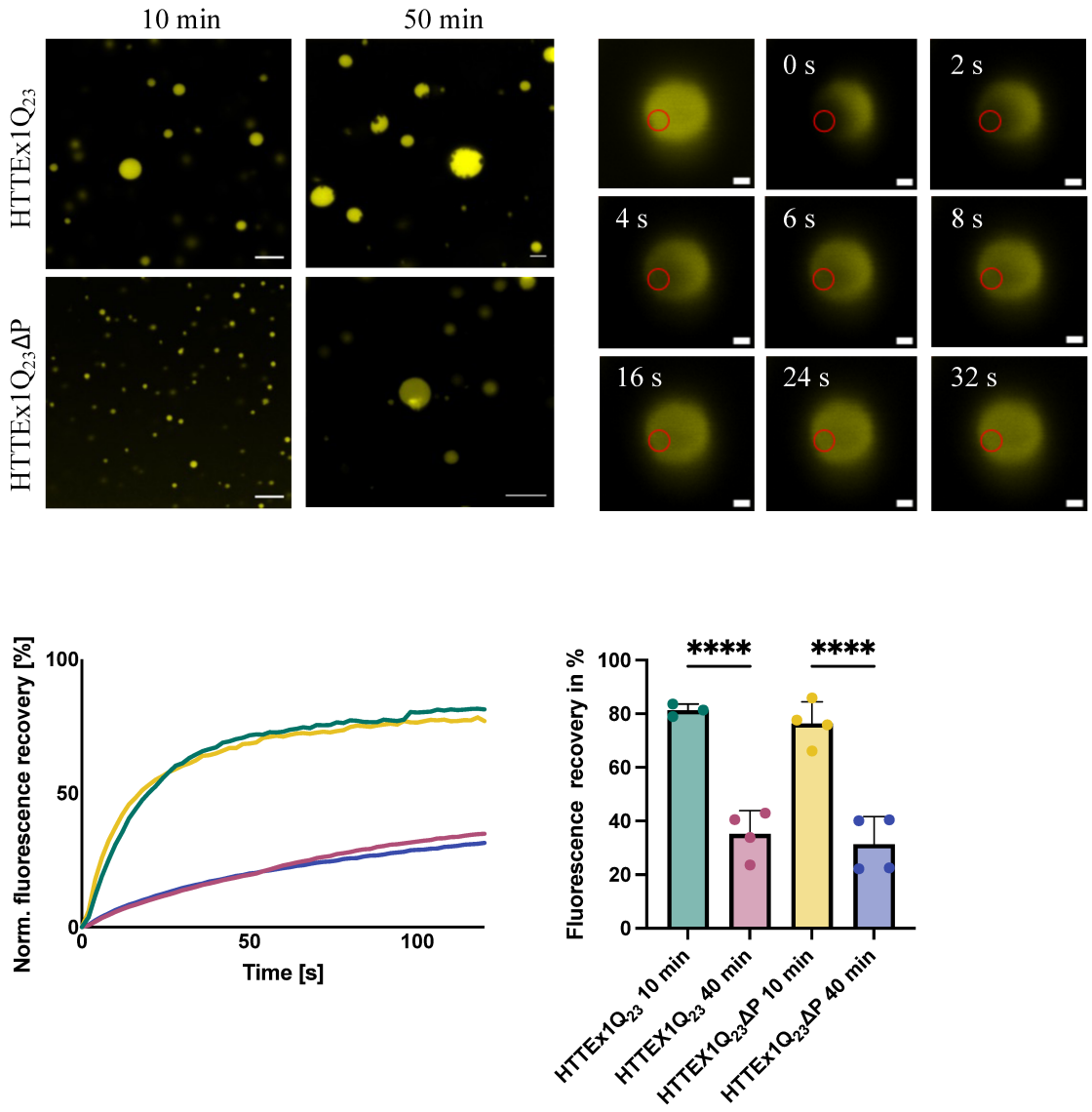

Figure 3.25: Liquid to solid phase transition of HTTEx1Q$_{23}$ and HTTEx1Q$_{23}$ΔP

At the top left, confocal images of 45 µM GST-HTTEx1Q$_{23}$ + 5 µM HTTEx1Q$_{23}$-YPet or 45 µM GST-HTTEx1Q$_{23}$ΔP + 5 µM HTTEx1Q$_{23}$ΔP-Ypet in LLPS 10 and 50 minutes after addition of 10 % Dextran are shown. Scale bars are 5 µm. On the top right, an exemplary FRAP experiment is shown. Scale bars are 5 µm. The graph at the bottom left is a representative result of three independent experiments and shows the normalized fluorescence recovery in % over time of HTTEx1Q$_{23}$ or HTTEx1Q$_{23}$ΔP at 10 and 40 minutes after addition of Dextran. The right graph shows the average final fluorescence recovery in % after 120 s with error bars depicting the SD. Each dot represents one independent experiment. Data were analyzed by a one-way ANOVA. ****p ≤ 0.0001.

3.3.3 DNAJB1 co-condensates with HTTEx1, but requires Hsc70 and ATP to suppress the liquid to solid phase transition of HTTEx1

The chaperone complex consisting of Hsc70, DNAJB1 and Apg2 has been shown to suppress aggregation of HTTEx1 (Scior et al., 2018) and therefore would be expected to interact with soluble moieties of HTTEx1. Here I investigated if and how the chaperones could affect the liquid to solid phase transition of HTTEx1Q_{23} and HTTEx1$Q_{23}\Delta$P.

For DNAJB1 it has been previously shown that it phase separates on its own (Gu et al. 2020) As the buffer conditions were different compared to the phase separation buffer used for HTTEx1, I first tested if DNAJB1 was phase separating under the same conditions as HTTEx1. DNAJB1_mCherry phase separated under the same conditions as HTTEX1Q_{23}-YPet and showed droplet growth over time (Fig. 3.26a). Notably, compared to HTTEx1Q_{23} the morphology of the droplets seemed not to change.

When DNAJB1_mCherry was mixed with HTTEx1Q_{23} or HTTEx1$Q_{23}\Delta$P co-condensation was observed (Fig. 3.26a). This was surprising, as HTTEx1$Q_{23}\Delta$P was missing the proline rich domain and therefore the binding site of DNAJB1.

Performing FRAP measurements showed that DNAJB1 alone had no effect on the liquid to solid phase transition of HTTEx1Q_{23} or HTTEx1$Q_{23}\Delta$P, although it was co-condensating (Fig. 3.26b+c). The FRAP recovery was determined 10 min and 40 min after addition of 10 % Dextran to the protein mixture and showed recovery efficiencies of ~80 % after 10 min and ~40 % after 40 min, which was equal to the measurements without DNAJB1 (Fig. 3.25). Upon addition of Hsc70 and ATP together with DNAJB1, the fluorescence recovery after 40 min was increased to ~80 % for HTTEx1Q_{23} while it was not significantly changed for HTTEx1$Q_{23}\Delta$P (Fig. 3.26c).

These results suggest that although DNAJB1 was co-condensating with HTTEx1Q_{23} and HTTEx1$Q_{23}\Delta$P, it required the PRD presumably as binding site to prevent liquid to solid phase transition. Additionally, these results show that DNAJB1 requires Hsc70 and ATP to suppress liquid to solid phase transition, suggesting an active chaperone-mediated process.

a)

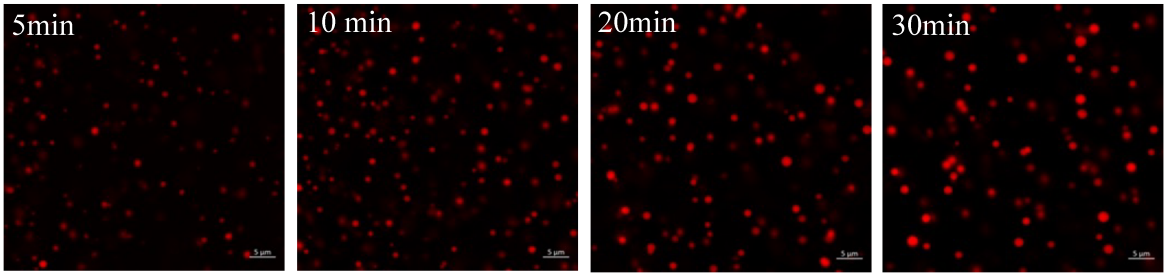
5min
10 min
20min
30min

b)

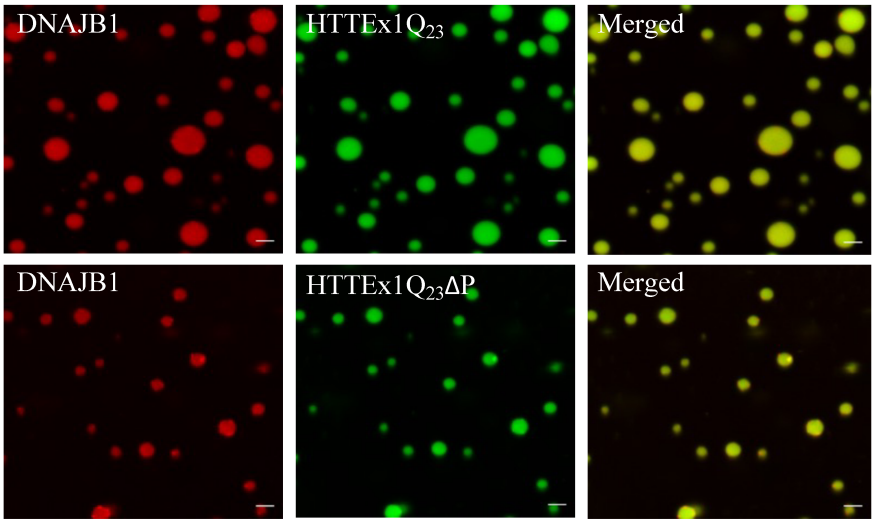
DNAJB1
HTTEx1Q23
Merged
DNAJB1
HTTEx1Q23ΔP
Merged

c)

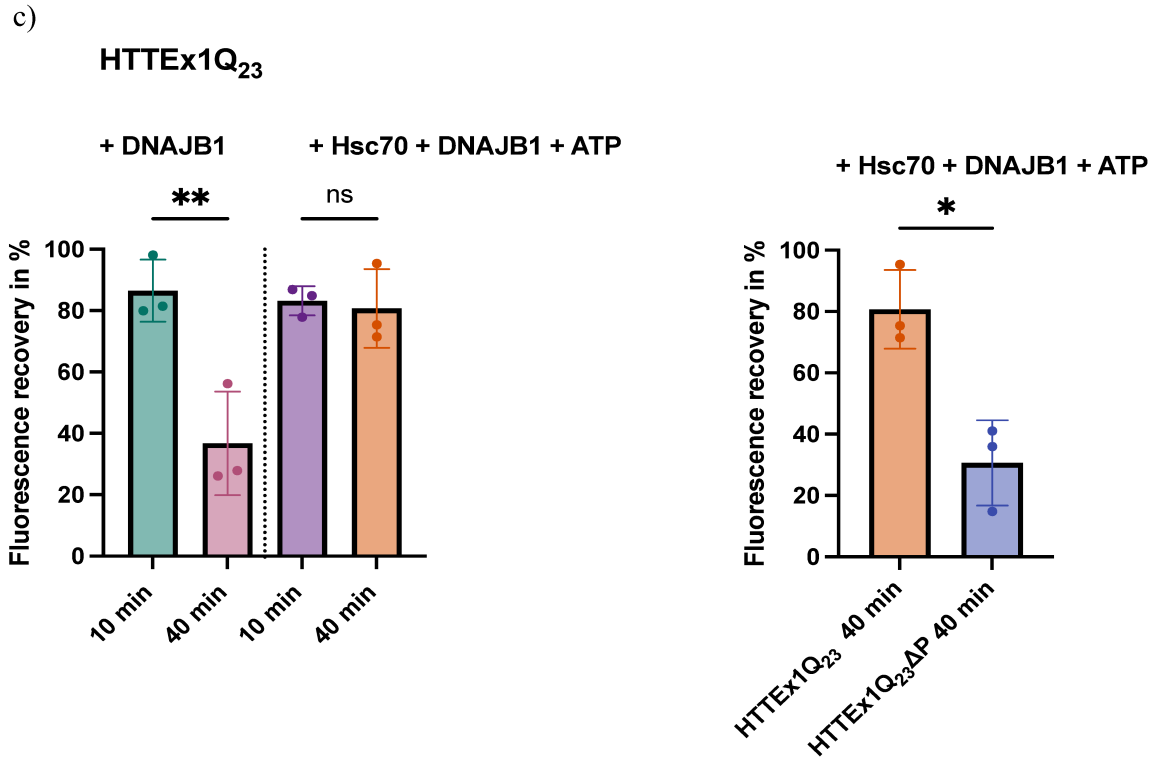
HTTEx1Q23
+ DNAJB1
+ Hsc70 + DNAJB1 + ATP
**
ns
Fluorescence recovery in %
100
80
60
40
20
0
10 min
40 min
10 min
40 min
+ Hsc70 + DNAJB1 + ATP
*
Fluorescence recovery in %
100
80
60
40
20
0
HTTEx1Q23 40 min
HTTEx1Q23ΔP 40 min

Figure 3.26: Effect of chaperones on liquid to solid phase transition of HTTEx1Q$_{23}$ and HTTEx1Q$_{23}$ΔP

a) Confocal images of droplet formation and droplet maturation of 40 µM DNAJB1_mCherry in LLPS buffer with 10 % Dextran. Scale bars are 5 µm. **b)** Confocal images showing co-localization of DNAJB1 and HTTEx1Q$_{23}$ or HTTEx1Q$_{23}$ΔP with GST-HTTEx1Q$_{23}$/ΔP (45 µM) + HTTEx1Q$_{23}$/ΔP_YPet (5 µM) + DNAJB1_mCherry (5 µM) 40 min after addition of 10 % Dextran. Scale bars are 5 µm. **c)** bar graphs are showing the average final fluorescence recovery in % after 120 s with error bars depicting the SD. FRAP experiments were performed at 10 min and 40 min after addition of Dextran. Each dot represents one independent experiment. Data were analyzed by a one-way ANOVA. *p ≤ 0.05; **p ≤ 0.01; ns non-significant.

.

4. Discussion

4.1 The Huntingtin binding motif of DNAJB1

This work contributed to the understanding of the interaction between HTTEx1 and DNAJB1. It was known before that DNAJB1 co-localizes with HTTEx1 fibrils and can suppress HTTEx1 aggregation in an ATP dependent manner with Hsc70 and Apg2 (Scior *et al.*, 2018).

However, the mechanism remained unknown. Now, that the binding site of DNAJB1 could be mapped to the second proline stretch of the proline rich region of HTTEx1 and a 9-amino acid motif in the C-terminal domain of DNAJB1, I was able to contribute with this work in investigating the binding mechanism.

In the binding motif of DNAJB1, H244 was found to be the most crucial amino acid. Mutation of this specific amino acid could completely disrupt the ability of DNAJB1 to suppress HTTEx1 aggregation (H244A; H244F). Substitution of H244 by a charged or polar amino acid (H244Q) could partially restore its function.

Molecular dynamics and docking experiments hinted that it is not the side chain at position 244 of DNAJB1 but the back bone of the peptide chain that is interacting with HTTEx1 while the side chain forms a stable hydrogen bond with E173. Mutating E173 to alanine and thereby preventing the formation of the intramolecular hydrogen bond did however not impair its ability to suppress HTTEx1 aggregation. As further docking experiments revealed, in this case the side chain of H244 forms a stable hydrogen bond directly with HTTEx1. From these findings, it can be concluded that hydrogen bonds are required to stabilize the DNAJB1/HTTEx1 interaction. The mechanism through which DNAJB1^{E174A} mutation affects the suppression of HTTEx1 aggregation must be further investigated. As MD simulations did not show any interactions between E174 and the Huntingtin binding motif and also docking experiments between DNAJB1^{E174A} and HTTEx1 showed no changes in the contact map (Fig. 3.9). This suggests that this amino acid is not involved in HTTEx1 binding and is rather impairing the DNAJB1/Hsc70 interaction specifically for HTTEx1 as it was able to refold heat-

denatured luciferase and promoted the ATPase activity of Hsc70, which also requires DNAJB1/Hsc70 interaction.

Suppression of HTTEx1 aggregation was shown to depend on the interaction of Hsc70 and DNAJB1. Mutations in the HPD motif in DNAJB1 (DNAJB1^{H32Q}) have been shown to disrupt its interaction with Hsc70 (Michels *et al.*, 1999). DNAJB1 alone cannot suppress HTTEx1 aggregation and suppression of HTTEx1 aggregation was shown to be ATP-dependent (Scior *et al.*, 2018). Consequently, disrupting the DNAJB1/Hsc70 interaction by mutating the HPD motif in DNAJB1 (DNAJB1^{H32Q}) resulted in a complete loss of its chaperone activities. For this reason, DNAJB1^{H32Q} was also not able to suppress HTTEx1 aggregation (Fig. 3.11). This is a major difference compared to other J-domain proteins such as DNAJB6 or DNAJB8, which have been shown to be able to suppress HTTEx1 aggregation in a Hsc70 independent manner by interacting with the PolyQ stretch of HTTEx1 (Gillis *et al.*, 2013; Kakkar *et al.*, 2016).

With the second proline stretch of the proline rich domain, a new binding site for chaperones on HTTEx1 was detected. So far, chaperones were only known to interact with the N17 region or the polyQ stretch of HTTEx1 (Tam *et al.*, 2006; Monsellier *et al.*, 2015; Kakkar *et al.*, 2016; Shen *et al.*, 2019). The FRET based experiments with HTTEx1Q$_{48}$ΔP1 support the findings of the cross-linking mass spectrometry that only detected binding between DNAJB1 and the second proline rich domain of HTT, but not the first. As the chaperones were still able to delay the aggregation of HTTEx1Q$_{48}$ΔP1 (Fig. 3.15)

In the FRET based assay it could be shown that the DNAJB1 concentration is one of the rate-limiting factors in the suppression of HTTEx1 aggregation. However, these assays were performed in a very controlled environment with samples just containing HTTEx1Q$_{48}$-CyPet/YPet, Hsc70, DNAJB1, Apg2 and an ATP regeneration system. In living cells, additional chaperones and chaperone complexes could be involved in Huntingtin interaction. The HEK cell experiments in which DNAJB1 was overexpressed while simultaneously expressing HTTEx1Q$_{97}$-EGFP showed that those principles observed *in vitro* also hold true in cells, despite the presence of additional chaperones.

Although our lab was able to show that the binding motif of DNAJB1 is required for suppression of HTTEx1 aggregation it is not the only relevant domain of the J-protein. As the binding motif is highly conserved among different J-domain proteins of class A and B also DNAJA1 contains the Huntingtin binding site, but is not able to suppress aggregation. FRET based aggregation experiments with protein chimeras of DNAJA1 and DNAJB1 revealed that probably also the G/F-rich region has an impact on the HTTEx1 J-domain protein interaction (Ayala Mariscal *et al.*, 2022).

4.2 DNJ-13 overexpression leads to an increased HTTEx1 aggregation in *C. elegans*

To study the effect of DNAJB1 on Huntingtin aggregation on an organismal level, Huntington´s disease *C. elegans* strains were employed (Pigazzini *et al.*, 2021). *C. elegans* itself contains only a single canonical class B J-domain protein in the cytosol, which is a homologue of the human DNAJB1, DNJ-13 (Davis *et al.*, 2022). Based on the results of the HEK cell experiments it was hypothesized that an overexpression of DNJ-13 would lead to a reduction of Huntingtin aggregation in *C. elegans*.

Co-localization of HTTEx1Q_{48} and DNJ-13 (Fig. 3.17) as well as the change in the expression pattern of DNJ-13 in the HTTEx1Q_{48} x DNJ-13 cross compared to the parental DNJ-13 strain (Fig. 3.16) indicated that DNJ-13 was interacting with HTTEx1Q_{48} in *C. elegans*. This is in line with previous *C. elegans* experiments, where Htt513Q_{128}-YFP was expressed in the muscle tissue of *C. elegans* and found to be co-localizing with endogenous DNJ-13 by immunostaining (Scior *et al.*, 2018). In the same publication, it was also shown that depletion of DNJ-13 by RNAi in nematodes expressing Htt513Q_{15}-YFP in the muscle tissue resulted in foci formation although the protein showed no aggregation in the control strain due to its non-pathogenic Q length. This shows that depletion of DNJ-13 negatively affects the proteostasis network in *C. elegans*.

Analysis of HTTEx1 aggregation by FLIM measurements revealed an increase in aggregation in the HTTEx1Q_{48} x DNJ-13 cross compared to the HTTEx1Q_{48} strain. These results were contradictory to my expectations based on the cell culture experiments. This posed the question why the overexpression of DNJ-13 led to an increase of Huntingtin aggregation in the nematodes, whereas it was shown in cell culture that overexpression of DNAJB1 reduced foci formation.

The histograms of the HTTEx1Q_{48} x DNJ-13 cross, wherein the tau values were plotted against the frequency showed a noticeable increase of species with tau values between 2.0 and 2.5 ns compared to the parental HTTEx1Q_{48} strain. While highly aggregated species with a tau value of 1 to 1.5 ns showed dark blue spots in the color-

coded FLIM images (Fig. 3.18 and 3.20), species with tau values between 2.0 and 2.5 ns seemed to be broader distributed indicated by light blue color in the color-coded FLIM images. For this reason, these species seem to be not fully aggregated yet, resulting in a more diffused distribution (Fig. 3.18) indicating higher mobility. These more mobile species could be either oligomeric species or smaller aggregates which could lead to an increased seeding potential and toxicity.

Huntingtin seeding activity has been discussed to be linked to Huntingtin pathology (Pecho-Vrieseling *et al.*, 2014; Pearce *et al.*, 2015; Jeon *et al.*, 2016). In previous FRET based seeding experiments it could be demonstrated that larger fibrils had less seeding potential compared to smaller fibrils generated by sonification from larger aggregates (Ast *et al.*, 2018). While there the overall structure of the fibril supposedly stayed same, this effect might be due to the increased surface area resulting in a higher seeding potential (Ast *et al.*, 2018). On the other hand, it has also been shown that Huntingtin amyloids can have different conformations and show polymorphism. *In vitro* grown fibrils at 4 °C showed a much higher toxicity compared to fibrils grown at 37 °C (Nekooki-Machida *et al.*, 2009; Mario Isas *et al.*, 2021). Both fibril types were found in *in vivo* mice models with higher proportions in specific brain areas (Nekooki-Machida *et al.*, 2009). Further structural analysis of the fibrils led to a model where the ß-sheet amyloid core of the fibrils is formed by the expanded polyQ stretch and the proline rich domain is pointing outwards (Lin *et al.*, 2017). Polymorphism of fibrils can be observed for other amyloidogenic proteins like Aß (Qian *et al.*, 1996; Kodali *et al.*, 2010; Lu *et al.*, 2013) and α-synuclein (Bousset *et al.*, 2013; Gath *et al.*, 2014) as well, but in those, the core structure between different strains was found to be changed, while for HTTEx1 fibrils the core seemed to remain the same. For this reason, the fibril types have been shown to be interconvertible and the difference mainly lays in the entanglement and dynamics of the proline rich domain (Mario Isas *et al.*, 2021). HTTEx1 was found to form at least three different fibril types, larger non-toxic fibrils (N-fibrils), toxic fibrils (T-fibrils) and proto fibrils (P-fibrils) (Fig. 4.1).

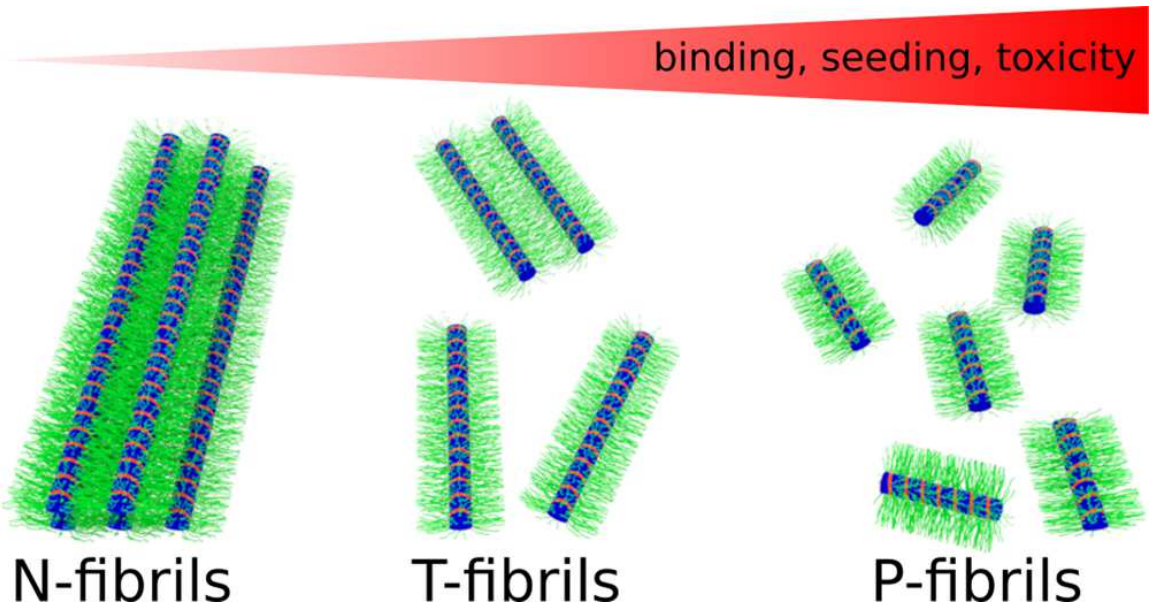

Figure 4.1: Model of HTTEx1 fibril strains

The proline rich domain is depicted in green while the fibril core is shown in blue. The entanglement of the proline rich domain is increasing from the P-fibrils (right) to the N-fibrils (left) while seeding potential and toxicity is increasing from N-fibrils to P-fibrils. (Figure from Mario Isas *et al.*, 2021).

As these fibril types can be interconverted, T-fibrils can convert to N-fibrils by further entanglement of their proline rich domain. Regarding their toxicity and seeding potential T and P-fibrils have been found to be far more toxic than N-fibrils (Nekooki-Machida *et al.*, 2009; Mario Isas *et al.*, 2021).

In all the proposed fibril strains of HTTEx1 the proline rich domain would be accessible for DNAJB1 which would allow speculation on how the chaperone complex consisting of Hsc70, DNAJB1 and Apg2 is able to not only suppress Huntingtin aggregation, but also interact with and disaggregate HTTEx1 fibrils. It has been shown that both, the human chaperones as well as their *C. elegans* orthologs, can disaggregate Huntingtin fibrils (Scior *et al.*, 2018; Ayala Mariscal *et al.*, 2022), but it remains unclear what the product of the disaggregation process would be.

There are different options, it is possible that monomers are released from the end of the fibrils, and the fibrils would be disassembled this way. Another option to consider is, as the binding site for both DNAJB1 and Hsc70 has been mapped to the second

proline stretch of the proline rich domain (Ayala Mariscal *et al.*, 2022), that the chaperones can disentangle the proline rich domains and thereby could convert N-fibrils back to T or P-fibrils.

T or P-fibrils show greater seeding potential compared to N-fibrils, which is discussed to be due to the better accessibility of the fibril surface, which could be a potential side for secondary seeding while fibril ends are involved in primary seeding and hence P and T-fibrils are shorter compared to N-fibrils, they would offer more sides for primary seeding as well (Mario Isas *et al.*, 2021).

Applying this theory to the nematodes, it could be speculated that overexpression of DNJ-13 leads to disaggregation of fibrils and could make them more accessible for primary and secondary nucleation events resulting in increased fibril formation. This theory would be supported by the increase of HTTEx1 species with tau values between 2.0 and 2.5 ns in young nematodes at day 4 while in older nematodes at day 7 the proportion of HTTEx1 species with longer life times are reduced. Although *in vitro* it has been shown, the trimeric chaperone complex consisting of Hsc70/Hsp-1, DNAJB1/DNJ-13 and Apg2/Hsp-110 is able to resolubilize HTTEx1 fibrils this process might be not favored *in vivo*.

To back this theory, further experiments have to be performed investigating the spreading of HTTEx1 in the nematodes. Additionally, one could investigate the seeding potential of nematode lysates in *in vitro* FRET based assays.

Interestingly and contrary to DNAJB1, DNAJB6 overexpression in a Huntingtin mouse model led to a reduction in HTTEx1 aggregation by inhibiting primary nucleation and subsequent formation of amyloid fibrils (Kakkar *et al.*, 2016). So far, DNAJB6 has only been shown to be able to suppress HTTEx1 aggregation, but not to disaggregate HTTEx1 fibrils which could explain the different effect on the aggregation propensity of HTTEx1 upon the overexpression *in vivo*.

The HTTEx1$Q_{48}\Delta$P strain showed an increased aggregation compared to HTTEx1Q_{48}, which is in line with previously published results and *in vitro* experiments (Pigazzini *et al.*, 2021). As expected, I could not detect any significant difference in the aggregation

propensity between HTTEx1$Q_{48}\Delta$P and HTTEx1$Q_{48}\Delta$P xDNJ-13 cross, likely due to the missing binding site for DNJ-13 in HTTEx1$Q_{48}\Delta$P.

The bottle brush model and the dual action of suppression and disaggregation of the chaperone complex could also be a possible explanation on how in the cell culture experiments overexpression of DNAJB1 reduced foci formation of HTTEx1Q_{97}-EGFP. Here I just transiently transfected the cells expressing both HTTEx1Q_{97}-EGFP and DNAJB1 simultaneously and increased levels of DNAJB1 were resulting in less fibril formation probably by improving the suppression of fibril formation. As for the siRNA experiments, the foci formation was also quantified 32 h after transfection of the HEK cells with HTTEx1Q_{97}-EGFP, depletion of DNAJB1 probably resulted in more aggregates as the suppression of fibril formation was impaired. Cell culture experiments have their limitations, as amyloid spreading, cross-tissue communication (e.g., trans-cellular chaperone signaling) and aging cannot be studied. These limitations demonstrate that it is important to carefully choose a suitable *in vivo* model system to study amyloid proteins and their associated pathologies.

4.3 Liquid-liquid phase separation of HTTEx1

So far, the aggregation mechanism of HTTEx1 *in vivo* remains unclear, however fibril formation of HTTEx1 is discussed to progress over intermediate steps of oligomers and amorphous aggregates (Scherzinger *et al.*, 1997; Poirier *et al.*, 2002; Lee, Walters and Murphy, 2007; Legleiter *et al.*, 2010; Vitalis and Pappu, 2011; Wetzel, 2012; Crick *et al.*, 2013), rather than by nucleated growth where a single misfolded protein initiates aggregation with the addition of monomers resulting in fibril growth (Esler *et al.*, 2000).

Recently it could be shown, that HTTEx1 can form liquid-like assemblies and that those convert into solid-like assemblies *in vitro* and HEK cells. This liquid to solid phase transition is discussed to be a pathway leading from soluble HTTEx1 residues to irreversible solid aggregates, as formation of solid-like assemblies could only be observed after formation of liquid-like assemblies (Peskett *et al.*, 2018).

Here I investigated the effect of the PolyQ flanking regions of HTTEx1 on the formation of liquid-like assemblies by confocal laser scanning microscopy and turbidity assays. It is known that aqueous solutions are not an efficient solvent for polyQ proteins (Crick *et al.*, 2006) and because of that there exists a threshold concentration for polyQ polymers defined as saturation concentration. Once this threshold is reached, the protein/solvent solution separates into a soluble and insoluble phase hence it is aggregating or phase separating (Crick *et al.*, 2013). The N17 region was discussed to destabilize nonspecific associations, deleting it slows down fibril formation (Crick *et al.*, 2013), which has been shown in *in vitro* (Thakur *et al.*, 2009) and cell culture experiments (Tam *et al.*, 2006). The proline rich region instead has been found to increase the saturation concentration of HTTEx1, thus reducing the driving force of aggregation (Crick *et al.*, 2013; Pigazzini *et al.*, 2021).

I did not observe any phase separation in the confocal images and consequently was unable to detect turbidity in the turbidity assay for GST-HTTEx1$Q_{23}\Delta$N17. If liquid to solid phase transition is on pathway for HTTEx1 fibril formation, this would be in line with previous observations of the N17 region promoting aggregation and deletion of it, delays aggregation (Arndt, Chaibva and Legleiter, 2015; Baias *et al.*, 2017). Mechanistically this could be explained by a proposed model, which is based on the

observation, that in monomeric HTTEx1 the N17 region does not form a stable secondary structure (Thakur *et al.*, 2009). Upon oligomerization of HTTEx1, the propensity of the N17 region forming α-helices, increases and is stabilized by intermolecular interactions (Jayaraman *et al.*, 2012). The formation of α-helix rich oligomers subsequently leads to the formation of β-sheets nucleating aggregation (Sivanandam *et al.*, 2011; Bugg *et al.*, 2012; Jayaraman *et al.*, 2012; Mishra *et al.*, 2012; Vieweg *et al.*, 2021).

Compared to GST-HTTEx1Q_{23}, GST-HTTEx1Q_{23}ΔP showed an increased number of droplets in the confocal images (Fig. 3.24), which resulted in an increased turbidity. Since deleting the proline rich domain decreases the saturation concentration, an increase of condensates would be in line with previous *in vitro* experiments (Crick *et al.*, 2013).

Contrary to Peskett *et al.*, 2018 where HTTEx1 was expressed in HEK cells and condensates/assemblies could be only observed for HTTEx1Q_{25}-GFP, but not for HTTEx1Q_{25}ΔP-GFP. From there they claimed, that the proline rich region promotes the formation of liquid-like assemblies. Therein, the protein was expressed in HEK cells and the Q-length was slightly increased compared to the here used HTTEx1Q_{23} which could have had an effect on condensate formation.

Another option that had an effect on condensate formation might have been the fluorescent tag. I worked with GST and fluorescently tagged HTTEx1 proteins. While the GST-tag was fused to the N-terminus, the fluorophore was fused to the C-terminus of HTTEx1. For the turbidity assay, only GST-tagged HTTEx1 constructs were used. The fluorophore might have had an effect on the condensation of HTTEx1ΔP.

It was shown by Pigazzini *et al.*; 2019 that HTTEx1ΔP C-terminally tagged with fluorophores showed no aggregation in a FRET based aggregation assay, while it usually is highly prone to aggregation. Titrating in non-fluorescently tagged HTTEx1ΔP resulted in faster aggregation kinetics, where the aggregation kinetics were dependent on the proportion of untagged to fluorescently tagged HTTEx1ΔP. Placing the fluorophore close to the aggregation prone domain therefore might affect its aggregation and condensation (Riguet *et al.*, 2021).

This also became a challenge for me when I later on tried to perform FRAP experiments with HTTEx1Q_{23}_YPet and HTTEx1$Q_{23}\Delta$P_YPet, where the condensate formation of HTTEx1$Q_{23}\Delta$P_YPet seemed greatly reduced compared to the experiments with the GST-tagged proteins. For that reason, I ultimately used 90 % GST-tagged HTTEx1Q_{23}/HTTEx1$Q_{23}\Delta$P and only 10 % fluorescently tagged protein in further experiments. Having some proportion of fluorescently tagged protein in it was necessary to perform FRAP and co-localization experiments. Removing the GST-tag, like it was done in the FRET assays for HTTEx1ΔP, would require the addition of PreScission protease to the phase separation mixture, which would add another variable.

In addition, a tag close to the aggregation prone region might affect condensation and aggregation propensity of the proteins and would also suggest that GST-HTTEx1$Q_{23}\Delta$N17 condensation might be affected by the GST-tag more severely than the other HTTEx1 variants, as here the GST-tag is immediately preceding the polyQ stretch. To eliminate that possibility, one should use the C-terminally fluorescently tagged proteins again. In the *C. elegans* Huntington´s disease models, which are expressing HTTEx1Q_{48} and HTTEx1$Q_{48}\Delta$P, this problem was circumvented as only a substoichiometric fraction of the protein is labelled.

To investigate the effect of chaperones on the liquid to solid phase transition and relate those results to the *in vivo* experiments I focused on HTTEx1Q_{48} and HTTEx1$Q_{48}\Delta$P for now. The FRAP experiments revealed, that over time both, HTTEx1Q_{48} and HTTEx1$Q_{48}\Delta$P, were solidifying (Fig. 3.25). Surprisingly both of them co-condensated with DNAJB1 although HTTEx1$Q_{48}\Delta$P is missing the binding site. (Fig. 3.26b)

Co-condensation might be a step prior to the suppression of liquid to solid phase transition. DNAJB1 together with Hsc70 and ATP was shown here to suppress the liquid to solid phase transition of HTTEx1Q_{23} for at least 40 min while the same could not be observed for HTTEx1$Q_{48}\Delta$P (Fig. 3.26c). Indicating that also here in the early phase of condensation, the binding site is crucial for suppression of liquid to solid phase transition and subsequently fibril formation.

It has been shown, that structural factors that favor LLPS are intrinsically disordered regions and low complexity domains, where specific amino acids are overrepresented

(Harmon *et al.*, 2017; Martin and Mittag, 2018; Alberti, Gladfelter and Mittag, 2019) For DNAJB1 this description fits to the G/F-rich region and deletion of it has been shown to drastically diminish the phase separation of DNAJB1 (Gu *et al.*, 2020). For DNAJA1, which contains a shorter G/F region than DNAJB1, no liquid-like condensates were observed but a more gel-like structure (Gu *et al.*, 2020). Investigating if DNAJA1 also co-condensates with HTTEx1 would be interesting as it harbors the HTTEx1 binding site. An absence of co-condensation of DNAJA1 and HTTEx1 could imply that this step is needed to bring the HTT-binding motif of the J-domain protein and the proline-rich region of HTTEx1 into close contact to allow stable hydrogen bond formation. In the FRET based aggregation assays it has been shown, that replacing the G/F-rich region of DNAJA1 by that of DNAJB1 allowed DNAJA1 to partially suppress HTTEx1 aggregation (Ayala Mariscal *et al.*, 2022), supporting the assumption that co-condensation might be the a critical step how chaperones could interfere with the aggregation cascade of HTTEx1 .

5. Material

5.1 Chemicals and solutions

Product	Company
Acetic acid	VWR, Darmstadt, Germany
Agar Agar	Carl Roth, Karlsruhe, Germany
Agarose	Biozym, Oldendorf, Germany
Ammonium molybdate	Riedel-de Haen AG
Ampicillin	Sigma Aldrich, St. Louis, USA
Adenosine triphosphate	Sigma Aldrich, St. Louis, USA
Ammoniumperoxodisulfat	SERVA Feinbiochemica, Heidelberg, Germany
β-mercaptoethanol	Sigma Aldrich, St. Louis, USA
Bacto Peptone	Carl Roth, Karlsruhe, Germany
Bromphenol blue	Merck, Darmstadt, Germany
Bovine serum albumin	Sigma Aldrich, St. Louis, USA
Calcium chloride	Sigma Aldrich, St. Louis, USA
Chloramphenicol	Carl Roth, Karlsruhe, Germany
Cholesterol	Sigma Aldrich, St. Louis, USA
cOmplete^{TM} protease inhibitor cocktail	Roche, Mannheim, Germany
Coomassie Brilliant Blue G-250	SERVA Feinbiochemica, Heidelberg, Germany
Deoxynucleotidetriphosphates	Thermo Fisher Scientific
Dextran (64 -76 kDa)	Sigma Aldrich, St. Louis, USA
Dithiothreitol	Carl Roth, Karlsruhe, Germany
DMEM High Glucose (4.5 g/l) with L-Glutamine with Sodium Pyruvate	Capricorn Scientific, Ebsdorfergrund, Germany
DMSO	Carl Roth, Karlsruhe, Germany
Ethylenediaminetetraacetic acid	Carl Roth, Karlsruhe, Germany

Ethanol	Chemsolute
Fetal-Calf-Serum EU approved	Capricorn Scientific, Ebsdorfergrund, Germany
Formaldehyde (37 %)	Sigma Aldrich, St. Louis, USA
L-Glutathione, reduced	Sigma Aldrich, St. Louis, USA
Glycerol	Carl Roth, Karlsruhe, Germany
Glycine	Sigma Aldrich, St. Louis, USA
Glycylglycine	AppliChem, Darmstadt, Germany
HEPES (4-(2-hydroxyethyl)-1-piperazineethanesulfonic acid)	Carl Roth, Karlsruhe, Germany
Hexanediol	Sigma Aldrich, St. Louis, USA
Hydrochloric acid (37 %)	VWR, Radnor, USA
Imidazole	Carl Roth, Karlsruhe, Germany
IPTG (Isopropyl-β-d-thiogalactopyranosid)	Thermo Fisher Scientific
Kanamycin	Carl Roth, Karlsruhe, Germany
LB agar	SERVA Feinbiochemica, Heidelberg, Germany
LB media	Carl Roth, Karlsruhe, Germany
D-Luciferin	Sigma Aldrich, St. Louis, USA
Magnesium acetate	Merck, Darmstadt, Germany
Magnesium chloride	Carl Roth, Karlsruhe, Germany
Magnesium Sulfate	Carl Roth, Karlsruhe, Germany
Malachite green hydrochloride	Carl Roth, Karlsruhe, Germany
2-Mercaptoethanol	Sigma Aldrich, St. Louis, USA
Methanol	VWR, Darmstadt, Germany
Milk powder	Sucofin
Mono- & dipotassium phosphate	Merck, Darmstadt, Germany
Monosodium citrate	Carl Roth, Karlsruhe, Germany
Mono- & disodium phosphate	Carl Roth, Karlsruhe, Germany
Penicillin/Streptomycin Solution (100x)	Capricorn Scientific, Ebsdorfergrund, Germany
Phenylmethylsulfonylfluorid (PMSF)	Sigma Aldrich, St. Louis, USA

Phosphoenolpyruvic acid	Sigma Aldrich, St. Louis, USA
Polyethylenimine	Polyscience, Eppelheim, Germany
Potassium acetate	Carl Roth, Karlsruhe, Germany
Potassium chloride	Sigma Aldrich, St. Louis, USA
Potassium hydroxide	Merck, Darmstadt, Germany
Sodium acetate	Riedel-de Haen AG
Sodium dodecyl sulfate	Carl Roth, Karlsruhe, Germany
Sodium azide	Carl Roth, Karlsruhe, Germany
Sodium chloride	Carl Roth, Karlsruhe, Germany
Sodium hydroxide	Carl Roth, Karlsruhe, Germany
Tetramethylethylenediamine (TEMED)	Merck, Darmstadt, Germany
Tris(hydroxymethyl)aminomethane	Carl Roth, Karlsruhe, Germany
Triton X-100	Sigma Aldrich, St. Louis, USA
Tween 20	SERVA Feinbiochemica, Heidelberg, Germany
Yeast extract	Carl Roth, Karlsruhe, Germany

5.2 Buffers and media

Name	Composition
Ammonium molybdate stock solution	5.7 % (w/v) ammonium molybdate in 6 M HCl, filtered (0.2 µm)
Assay buffer (Luciferase assay)	25 mM Glycylglycine; 100 mM KCl; 15 mM $MgCl_2$; 5 mM ATP
Benzonase buffer	1 mM $MgCl_2$, 50 mM Tris, pH 8.0
Coomassie staining solution	2.5 % (v/v) Coomassie brilliant blue G-250, 40 % (v/v) methanol, 10 % (v/v) acetic acid
Destaining solution	40 % (v/v) ethanol, 10 % (v/v) acetic acid
Dialysis buffer (GST-tag purification)	50 mM Tris pH 7.4, 150 mM NaCl, 1 mM EDTA, 5 % glycerol
Dialysis buffer (His-tag purification)	30 mM HEPES pH 7.4, 100 mM KCl, 5 mM $MgCl_2$, 10 % glycerol, 1 mM β-mercaptoethanol
Elution buffer (GST-tag purification)	50 mM NaH_2PO_4, 5 mM Tris, 150 mM NaCl, 1 mM EDTA, 20 mM reduced glutathione; pH 8.6
Elution buffer (His-tag purification)	30 mM HEPES pH 7.4, 100 mM KCl, 5 mM $MgCl_2$, 300 mM imidazole, 10 % (v/v) glycerol, 1 mM β-mercaptoethanol

Green malachite stock solution	0,082 % (w/v) green malachite, filtered (0.2 µm)
High salt buffer	30 mM HEPES pH 7.4, 1 M KCl, 5 mM $MgCl_2$, 25 mM imidazole, 10 % glycerol, 1 mM β-mercaptoethanol
HMK buffer (Luciferase assay)	50 mM HEPES-KOH; 100 mM KCl; 5 mM $MgCl_2$; 1 mM DTT; 10 µM BSA; pH 7,4
Liquid-liquid phase separation buffer	50 mM Na_2HPO_4/NaH_2PO_4, 150 mM NaCl, pH 7.4
Low salt buffer	30 mM HEPES pH 7.4, 50 mM KCl, 5 mM $MgCl_2$, 25 mM imidazole, 10 % glycerol, 1 mM β-mercaptoethanol
Lysis buffer (cell culture)	50 mM Tris/HCl pH 7.4, 150 mM NaCl, 1 mM EDTA, 1 % Triton X-100, 1 tab/50 ml of complete EDTA-free protease inhibitor cocktail (Roche)
Lysis buffer (GST-tag purification)	50 mM NaH_2PO_4, 5 mM Tris, 150 mM NaCl, 1 mM EDTA, 1 mM PMSF, 1 tab/50 ml of complete EDTA-free protease inhibitor cocktail (Roche); pH 8.0
Lysis buffer (His-tag purification)	30 mM HEPES pH 7.4, 500 mM KCl, 5 mM $MgCl_2$, 30 mM imidazole, 10 % glycerol, 1 mM PMSF, 1 mM β-mercaptoethanol, 10 µg/ml DNase I, 1 tab/50 ml of complete EDTA-free protease inhibitor cocktail (Roche)

Lysis buffer (nematodes)	10 mM β-Mercaptoethanol, 1% Triton X100, 20 mM Tris HCl (pH 7.5) + protease inhibitor cocktail
M9	3 g/l KH_2PO_4, 5 g/l NaCl, 6 g/l Na_2HPO_4 Autoclave, then add: 1 mL 1 M $MgSO_4$
NGM-Agar / RNAi-Aagar	50 mM NaCl; 2,5 g/l Bacto Peptone; 17 g/l Agar Agar; 5 µg/ml cholesterol; 1 mM $CaCl_2$; 1 mM $MgSO_4$; 25 mM KH_2PO_4; pH 6 + 100 µg/ml Ampicillin and 1 mM IPTG for RNAi plates
10x reaction buffer (FRET assay)	300 mM Hepes pH 7.4, 1.5 M NaCl, 50 mM $MgCl_2$
Running buffer (10x) for SDS PAGE	25 mM Tris-HCl (pH 8.8), 192 mM glycine, 0.1 % (w/v) SDS, filtered (0.2 µm)
4 x SDS sample loading buffer	100 mM Tris-HCl (pH6.8), 4 % (w/v) SDS, 30 % (v/v) glycerol, 0.2 % (w/v) Bromophenol blue, 100 mM DTT
SDS wash buffer	0.1 %, 1 %, or 2 % SDS, 150 mM NaCl, 10 mM Tris pH 8.0
Separation gel buffer for SDS-PAGE	1.5 M Tris-HCl, pH 8.8, 0.04% (w/v) SDS, filtered (0.2 µm)
Stacking gel buffer for SDS-PAGE	0.5 M Tris-HCl, pH 6.8, 0.04% (w/v) SDS, filtered (0.2 µm)
2x Termination buffer	40 mM EDTA, 4 % SDS, 100 mM DTT

10x TBS	200 mM Tris; 1,5 M NaCl
10x TBS-T	200 mM Tris; 1,5 M NaCl; 1 % Tween 20 (v/v)
Wash buffer (GST-tag purification)	50 mM NaH_2PO_4, 5 mM Tris, 150 mM NaCl, 1 mM EDTA, 1 tab/50 ml of complete EDTA-free protease inhibitor cocktail (Roche), 0.1 % Triton X-100; pH 8.0

5.3 Enzymes

Enzyme	Company
DNAse I	AppliChem GmbH, Darmstadt, Germany
DpnI	New England Biolabs, Ipswich, USA
Luciferase	Sigma Aldrich, St. Louis, USA
Lysozyme	Carl Roth, Karlsruhe, Germany
Phusion High-Fidelity DNA Polymerase	New England Biolabs, Ipswich, USA
PreScission™ Protease	Kirstein lab
Pyruvate kinase	Sigma Aldrich, St. Louis, USA
SUMO protease (Ulp1 fragment)	Kirstein lab
Trypsin	Capricorn Scientific, Ebsdorfergrund, Germany

5.4 Ladders and dyes

Product	Company
DNA loading dye (6x)	Thermo Fisher Scientific, Waltham, USA
GeneRulerTM 1kb	Thermo Fisher Scientific, Waltham, USA
PageRulerTM Plus Prestained Protein Ladder	Thermo Fisher Scientific, Waltham, USA

5.5 Kits

Product	Name	Company
Gibson cloning	Gibson Assembly®	New England Biolabs, Ipswich, USA
Plasmid isolation	NuceloSpin Plasmid Mini	Macherey-Nagel, Düren, Germany
Western blot	Trans-Blot® TurboTM Mini PVDF/Nitrocellulose Transfer Packs	BioRad, Hercules, USA
ECL Detection Kit	Pierce ECL Western Blot Substrate	Thermo Fisher Scientific, Waltham, USA

5.6 Antibodies

Primary antibodies	Origin	Dilution	Company
Anti-β -actin	mouse	1:1000	Abcam (ab8224)
Anti-DNAJB1 (polyclonal)	rabbit	1:2000	Proteintech (cat.no: 13174-1-AP)
Anti-GFP B34 (monoclonal)	mouse	1:1000	ENZO Life Sciences, Farmingdale, USA (cat.no: ENZ- ABS141-0200)
Secondary antibodies			
Goat IgG anti-rabbit IgG (H+L)-HRPO	goat	1:10000	DIANOVA (cat.no: 111-035-003)
Goat IgG anti-mouse IgG (H+L)-HRPO	goat	1:10000	DIANOVA (cat.no: 115-035-003)

5.7 Consumables

Consumable	Manufacturer
Pipette tips (1000 µL, 200 µL, 10 µL)	Sarstedt Nümbrecht, Germany
PCR tubes	Sarstedt, Nümbrecht, Germany
Microtubes (1.5 mL, 2 mL)	Sarstedt Nümbrecht, Germany
Microfuge® Tube Polyallomer 1.5 mL	Beckman Coulter, Brea, USA
Low Binding Tubes 1.5 ml	Sarstedt Nümbrecht, Germany
Falcon tubes (15 ml, 50 mL)	Sarstedt Nümbrecht, Germany
Amicon® Ultra Centrifugal filter units (0.5 ml, 15 ml with 10 or 30 kDa MWC)	Merck Millipore, Cork, Ireland
Petri dishes	Sarstedt Nümbrecht, Germany
Platinum wire (0.3 mm)	Carl Roth, Karlsruhe, Germany
Conical flasks	Schott, Mainz, Germany
Laboratory bottles with cap	Schott Mainz, Germany
Graduated cylinders	Vitlab, Großostheim, Germany
Cuvettes	Eppendorf, Hamburg, Germany
Serological pipettes (5 mL, 10 mL, 25mL)	Sarstedt AG & Co. KG
384-wells Flat Bottom Black Polystyrene Plate	Corning Life Sciences, Corning, USA
384-wells Flat Bottom White Polystyrene Plate	Corning Life Sciences, Corning, USA

96-well Microplate, transparent	Sarstedt AG & Co. KG
96-well Microplate, white	Corning Life Sciences, Corning, USA
NALGENE® Centrifuge bottles, 500 mL	Nalgene, New York, USA
Polypropylene Columns (5 mL)	QIAGEN N.V.
Dialysis membrane (MWCO 6-8 kDa)	Spectrum laboratories
High-Density Nickel 6BL-QNi-100	Agarose Bead Technologies
Glutathione sepharose beads	GE Healthcare Buckinghamshire, UK
Glass Microscopy Slides	Epredia, Braunschweig, Germany
Glass Microscopy Cover Slides	Carl Roth, Karlsruhe, Germany
Filter Paper 0.22 uM	Sartorius, Göttingen, Germany

5.8 Equipment

Device	Name	Company
Blotting Transfer Cell	Trans-Blot® TurboTM	Bio-Rad, Hercules, USA
Centrifuge	Sorvall® EvolutionTM Rc Superspeed	Thermo Fisher Scientific, Waltham USA
	OptimaTM Ultracentrifuge	Beckman Coulter Inc.
	Centrifuge 5810 R	Eppendorf, Germany
	Centrifuge MiniSpin®	Eppendorf, Germany
Confocal Laser Scanning Microscope	LSM 880 with Airyscan	Zeiss, Germany
Container (electrophoresis)	Mini PROTEAN® Tetra Cell	Bio-Rad, Hercules, USA
Heating Block	Digital Heatblock	VWR/Avantor, USA
	Heating-Thermo Shaker MHR 11	Ditabis, Germany
	Thermoschüttler pro	CellMedia, Germany
Homogenizer	Precellys 24	Bertin instruments, Montigny-le-Bretonneux, France

Incubator (15°C)	TC255	Lovibond Tintometer GmbH, Dortmund, Germany
Incubator (30°C and 37°C)	Heraeus Kelvitron	Thermo Fisher Scientific, Waltham USA
Microfluidizer	LM10	MicrofluidicsTM Westwood, Massachusetts USA
pH meter		Mettler Toledo, Ohio, USA
Photometer	NanoPhotometer® N60	IMPLEN, Munich, Germany
Pipettes	Transferpette	Brand, Wertheim, Germany
Pipettor	Pipetboy	Integra Bioscience, Bibertal, Germany
Plate reader	Infinite® 200 pro	Tecan, Männedorf, Switzerland
	F200 Pro	Tecan, Männedorf, Switzerland
Power supply	PowerPacTM Basic	Bio-Rad, Hercules, USA
Scale	BP 221 S	Sartorius, Germany
	BL 1500	Sartorius, Germany
Shaker (WB)	GFL Shaker 3016	Lauda, Germany
	WT 16	Biometra® , Germany
Stereo Fluorescence Microscope	Leica M165 FC	Leica, Wetzlar, Germany
Thermocycler	C1000 Touch	Bio-Rad, Hercules, USA

Vacuum pump		H.Saur, Reutling; Germany
Vortex	Vortex VF2	Janke & Kunkel Labortechnik
Westernblot detection system	ChemoStar Touch ECL	Intas, Germany
Westernblot system (semi-dry)	Trans-Blot Turbo Transfer System	Bio-Rad, Hercules, USA

5.9 Plasmids

Plasmid	Source
pGEX-6P1-HttExon1Q_{48}-CyPet	Kirstein lab (Scior *et al.*, 2018)
pGEX-HttExon1Q_{48}-YPet	Kirstein lab (Scior *et al.*, 2018)
pGEX-6P1-HttExon1Q_{48}ΔP1-CyPet	Kirstein lab (Pigazzini *et al.*, 2021)
pGEX-HttExon1Q_{48}ΔP1-YPet	Kirstein lab (Pigazzini *et al.*, 2021)
pGEX-6P1-PreScission	Kirstein lab
pET-6His-Smt3-Apg2	Bukau lab (Nillegoda *et al.*, 2015)
pET-6His-Smt3-Hsc70	Bukau lab (Nillegoda *et al.*, 2015)
pET-6His-Smt3-DNAJB1	Bukau lab (Nillegoda *et al.*, 2015)
pET-6His-Smt3-DNAJB1_H244Q	this work
pET-6His-Smt3-DNAJB1_H244F	this work
pET-6His-Smt3-DNAJB1_D234A	this work
pET-6His-Smt3-DNAJB1_F247A	this work
pET-6His-Smt3-DNAJB1_R249A	this work
pET-6His-Smt3-DNAJB1_E173A	this work
pET-6His-Smt3-DNAJB1_E174A	this work
pET-6His-Smt3-DNAJB1_H32Q_H244A	This work
pCDNA3-HTTExon1Q_{97}-EGFP	Kirstein lab (Scior et. al 2018)
pCDNA3-DNAJB1	Kirstein lab (Scior et. al 2018)

5.10 *C.elegans* strains

Strain	Genotype	Source
N2	wild type (*C. elegans* var Bristol)	CGC
DNJ-13	*dnj-13p::dnj-13::yfp*	Richter lab (Papsdorf et al. 2014)
mScarlet	*pPD_95-rgef-1::*-IRES-mSCA:: *-unc54-3'UTR*	Kirstein lab (Pigazzini 2021)
HTTEx1Q_{48}	*pPD_95-rgef-1::HttEx1Q_{48}-IRES-mSCA:: HttEx1Q_{48}-unc54-3'UTR*	Kirstein lab (Pigazzini 2021)
HTTEx1Q_{48}ΔP	*pPD_95-rgef-1::HttEx1Q_{48}ΔP-IRES-mSCA:: HttEx1Q_{48}ΔP-unc54-3'UTR*	Kirstein lab (Pigazzini 2021)
mScarlet x DNJ-13	*pPD_95-rgef-1::*-IRES-mSCA:: *-unc54-3'UTR; dnj-13p::dnj-13::yfp*	this work
HTTEx1Q_{48} x DNJ-13	*pPD_95-rgef-1::HttEx1Q_{48}-IRES-mSCA:: HttEx1Q_{48}-unc54-3'UTR; dnj-13p::dnj-13::yfp*	this work
HTTEx1Q_{48}ΔP x DNJ-13	*pPD_95-rgef-1::HttEx1Q_{48}ΔP-IRES-mSCA:: HttEx1Q_{48}ΔP-unc54-3'UTR; dnj-13p::dnj-13::yfp*	this work

5.11 Bacterial strains

Strain	Genotype
DH5α	*E. coli* [*dlacZ Delta M15 Delta(lacZY A-argF) U169 recA1 endA1 hsdR17(rK-mK+) supE44 thi-1 gyrA96 relA1*] (plasmid preparation/cloning)
BL21 (DE3) pRare	*E. coli* [*fhuA2 [lon] ompT gal (λ DE3) [dcm] ΔhsdS* pRARE (Cam^R) *λ DE3 = λ sBamHIo ΔEcoRI-B int::(lacI::PlacUV5::T7 gene1) i21 Δnin5*] (protein expression)
OP50	*E. coli* (*C. elegans* food source), Uracil auxotroph

5.12 Software/online tools

Software/online tool	Company
BioRender	BioRender
Fiji v2.0	ImageJ (Schindelin *et al.*, 2012)
Fiji-plugin: JaCoP	Bolte and Cordelières, 2006
FLIMFit 5.1.1	Photonics Group, Physics Department at Imperial College London
i-control 2.0	Tecan
Microsoft Excel 2019	Microsoft Corporation
Microsoft Word 2019	Microsoft Corporation
NEBuilder Assembly Tool 2.0	New England BioLabs
Prism 9.3.1	GraphPad
SnapGene Viewer	SnapGene
SymPhoTime 64	PicoQuant
Tm calculator 1.16.5	New England BioLabs
Zen lite	Zeiss, Oberkochen, Germany
Zen 2.3 SP1	Zeiss, Oberkochen, Germany

6. Methods

6.1 *In vitro* methods

6.1.1 Polymerase chain reaction

Polymerase chain reaction (PCR) was employed for site-directed mutagenesis or to amplify DNA for molecular cloning using specific primers for the desired mutation or region of interest that was supposed to be amplified. In general, the PCR was carried out in a reaction volume of 50 µl in 1x Phusion HF buffer. The reaction mixture also contained dNTPs (200 µM), Primers (0.5 µM each), Phusion Polymerase (1 U) and the DNA template (50 ng for genomic DNA and 10 ng for plasmids). For the standard PCR program, the DNA was denatured in an initial denaturation step at 98 °C for 30 s followed by 35 cycles of denaturation at 98 °C for 10 s, annealing of the primers at 45-72 °C for 30 s (depending on primer length and sequence) and elongation at 72 °C for 30 s per kb. For a final extension step, the reaction was kept at 72 °C for 5-10 min after the last cycle. In cases where the PCR reaction was not successful, 3 % of DMSO were added to the reaction mix.

6.1.2 QuikChange™ site-directed mutagenesis PCR

For generating single amino acid exchanges of DNAJB1 site directed mutagenesis was employed. For that primers were designed, that had a base pair mismatch in the middle carrying the desired mutations and annealing overhangs of approximately 20 bp at each side (Table). In a PCR, the whole plasmid was amplified using Phusion high fidelity DNA Polymerase.

PCR program:

98 °C for 3 min	
98 °C for 30 s 55 °C for 1 min 68 °C for 1 min per kb	x 18
68 °C for 15 min	

Upon completion of the PCR, 1 µl of DpnI (10 U/µl) was directly added to the PCR tubes, which were subsequently incubated for 1 h at 37 °C to digest the parental plasmid. DpnI was inactivated at 80 °C for 30 min. Afterwards, the plasmid was purified (using the NuceloSpin Plasmid Mini Kit) and transformed into *E. coli* DH5α. Colonies, from which overnight cultures were prepared, were picked the next day. Plasmid was isolated and the successful mutagenesis was verified by DNA sequencing (LGC, Biosearch Technologies)

Table 6.1: List of oligonucleotides for site directed mutagenesis

DNAJB1_D234A	Fw	ccaacaacattccagctgctatcgtctttgttttaaag
	Rv	ctttaaaacaaagacgatagcagctggaatgttgttgg
DNAJB1_F247A	Fw	caagccccacaatatcgctaagagagatggctctg
	Rv	cagagccatctctcttagcgatattgtggggcttg
DNAJB1_R249A	Fw	cacaatatctttaaggcagatggctctgatgtc
	Rv	gacatcagagccatctgccttaaagatattgtg
DNAJB1_H244Q	Fw	gttttaaaggacaagccccagaatatctttaagagagatgg
	Rv	ccatctctcttaaagatattctggggcttgtcctttaaaac
DNAJB1_H244F	Fw	gtctttgttttaaaggacaagcccttcaatatctttaagagagatggctc
	Rv	gagccatctctcttaaagatattgaagggcttgtcctttaaaacaaagac
DNAJB1_E173A	Fw	cttcgagtctcccttgcagagatctacagcggc
	Rv	gccgctgtagatctctgcaagggagactcgaag
DNAJB1_E174A	Fw	gagtctcccttgaagcgatctacagcggctg
	Rv	cagccgctgtagatcgcttcaagggagactc

6.1.3 Gibson assembly

For cloning, Gibson assembly was employed since it allows cloning without restriction sites. For Gibson assembly, primers are designed in a way, that they have a complementary part, that anneals to the template and an overhang complementary to the insert/vector. After amplification by PCR, the PCR products are treated with exonucleases creating sticky ends, allowing the fragments to align.

Here, Gibson assembly was used to create the DNAJB1_linker_mCherry construct. For the PCR, following primers were used (Table 6.2).

Table 6.2: Primer for Gibson assembly

pSUMO_DNAJB1_linker_mCherry		
pMH1130 (rgef-1p::mcherry::gfp::lgg-1)	Fw	ccaataggtggaggcggttcagtgagcaagggcgaggagg
	Rv	ggtggtggtgctcgagcctacttgtacagctcgtccatgc
pSUMO_DNAJB1	Fw	gcatggacgagctgtacaagtaggctcgagcaccaccacc
	Rv	gctcactgaaccgcctccacctattggaagaacctgctc

Following the PCR, the PCR products were purified and the Gibson assembly reaction was set up by mixing 50 ng of vector with 3-fold molar excess of the insert and Gibson assembly master mix. The reaction was incubated for 1 h at 50 °C. Following the incubation, the mixture was either stored at -20 °C or directly used for transfection into DH5α. Successful cloning was verified by restriction digest and subsequent agarose gel electrophoresis. If that showed the expected results, samples were send for DNA sequencing.

6.1.4 Preparation of chemically competent *E. coli* cells

Overnight cultures of the *E. coli* strain of interest (DH5α or BL21) were prepared. The next day, 30 ml of LB medium supplemented with 10 mM $MgSO_4$ were inoculated with 300 µl of the overnight culture and incubated at 37 °C shaking until an OD_{600} of ~ 0,4 was reached. The bacteria were transferred into centrifuge vials and centrifuged at 5000 g for 5 min at 4 °C. The supernatant was discarded and the cells were resuspended in 10 ml of 0.1 M $CaCl_2$ solution. The cells were incubated on ice for 20 min before they were centrifuged again at 6000 g for 5 min at 4 °C. The supernatant was discarded and the cells were resuspended in 850 µl of cold 0,1 M $CaCl_2$ + 150 µl of 87 % glycerol. After resuspension, the cells were aliquoted into 50 µl aliquots and flash-frozen for storage at – 80 °C.

6.1.5 Heat-shock transformation

For transforming into *E. coli* DH5α or BL21, 50 µl of competent cells were thawed on ice. Thawed cells were mixed with max. 1/10 (volume/volume) of plasmid or ligation mix and incubated for 30 min on ice. Cells were heat shocked for 45 s at 42 °C and returned back to the ice for 2 min afterwards. Then 500 µl of SOC medium was added and the cells were incubated at 37 °C for 1 h at 750 rpm. 20 – 40 µl were plated onto LB-Agar plates containing the respective antibiotic. Plates were incubated overnight at 37 °C.

6.1.6 Protein expression

The recombinant proteins further used for biochemical assays were expressed in *E. coli* BL21. BL21 cells were transformed with the respective plasmid and from there usually glycerol stocks were prepared which were used for the inoculation of overnight cultures. Alternatively, overnight cultures could also be inoculated by picking colonies directly from the transformation plate. Cells were grown in LB-medium containing

25 µg/ml Chloramphenicol and 100 µg/ml Ampicillin or 25 µg/ml Kanamycin. With the overnight cultures the main culture was inoculated the next day by adding 1/100 of the final culture volume from the pre-culture. The main culture was supplemented with the same antibiotics as the overnight culture. Then the main culture was grown at 37 °C until an OD_{600} of 0.5 to 0.8 was reached. Afterwards, expression was induced by adding IPTG. Expression of chaperones was induced by addition of 0.5 mM IPTG followed by an incubated at 20 °C for 16 h on a shaker. Expression of HTT constructs was induced by adding 1 mM IPTG followed by an incubation at 18 °C for 16 h on a shaker. After the expression step, the cells were harvested by centrifugation at 8.000 x g at 4 °C for 30 min. From there, the protein was either directly purified or the pellets were transferred to smaller vials and recentrifuged at 18.000 rpm for 30 min at 4 °C before they were stored at -80 °C until the protein was purified.

6.1.7 Protein purification of His-tagged proteins (Chaperones)

Bacterial pellets from the overexpression of recombinant proteins were resuspended in 50 ml of lysis buffer by scratching with a glass rod and pipetting up and down. Any remaining bacterial clumps were disrupted by using a potter. Afterwards the bacteria were lysed using an LM10 microfluidizer. The microfluidizer was equilibrated with lysis buffer first, before passing the bacteria solution five times at 18.000 psi. Afterwards the lysate was centrifuged at 16.000x g for 30 min at 4 °C to get rid of cell debris. The supernatant was transferred into new cups and 1,5 ml of pre-washed Ni-NTA beads were added. The lysate was incubated with the beads on rollers at 4 °C for 1 h. Then the whole lysate was passed through a gravity flow column. The beads were washed with 25 ml of high-salt buffer followed by 25 ml of low-salt buffer. Then 5 ml of elution buffer were added to the beads and the column was incubated for 30 min at 4 °C on the rollers, before the elution fraction was collected. Subsequently, 1 ml of elution buffer was added to the beads and eluted by gravity flow. Protein content of the elution fractions was determined by adding drops of 20 µl of 1x Bradford reagent onto a piece of parafilm and mixing with 2 µl of each elution fraction. Elution fractions containing protein were pooled and mixed with SUMO-protease (conc.) before being transferred into a dialysis tube and dialyzed against 2 l dialysis buffer overnight. The next day the

protein was removed from the dialysis tube. If some protein precipitation was observed the protein solution was centrifuged at 18.000 x g for 10 min to get rid of most of the precipitated protein and prevent clogging of the reverse column. To remove the cleaved tag, 1 ml of beads were added and incubated with the protein for 30 min on the rollers at 4 °C. The flow through was collected and the final protein concentration determined by Bradford assay. The protein was aliquoted and flash frozen to be stored at -80 °C. While the purification process samples for SDS-PAGE analysis were taken at each step. All buffers were ice-cold and the protein lysate was kept cold throughout the purification process.

6.1.8 Protein purification of GST-tagged proteins (HTT-constructs)

The bacterial pellet from the overexpression was resuspended in 50 ml of lysis buffer, and passed through the microfluidizer five times at 18.000 psi. Afterwards, 1 % Triton X-100 (v/v) was added to the lysate by slowly pipetting it while the lysate was stirred on a stirring plate in the cold room at 4 °C. When the Triton X-100 was completely dissolved, the lysate was transferred into centrifugation tubes and centrifuged at 16.000 rpm for 40 min at 4 °C. In the meantime, 2 ml of glutathione sepharose beads were equilibrated with lysis buffer and added to the supernatant. The lysate with the beads was incubated on the rollers for 1 h at 4 °C allowing the tagged protein to bind to the beads. Next, the whole lysate was passed through a gravity flow column and the beads were washed with 25 ml of wash buffer.

For on-column cleavage (fluorescently tagged Htt constructs for phase separation), 5 ml of dialysis buffer containing 320 µg of PreScission were added to the column which was then incubated on the rollers overnight at 4 °C. The next day, the elution fractions were collected. Fractions containing protein could be identified by fluorescence and were pooled.

If the GST-tag was kept, 5 ml of elution buffer were added to the column and it was incubated at the rollers for 30 min at 4 °C. The elution fractions were collected. Fractions containing protein were identified by fluorescence or using Bradford reagent. Protein-containing fractions were then pooled and transferred to the dialysis tube.

Protein was then dialyzed against 2 l of dialysis buffer overnight. The next day, the protein was recovered from the dialysis tube.

The final protein concentration was determined by Bradford assay. The protein was aliquoted and flash frozen in liquid N_2 to be stored at -80 °C. During the purification process samples were collected at each step for SDS-PAGE analysis. All the buffers were ice cold and the protein lysate was kept cold throughout the purification process.

6.1.9 Protein quantification (Bradford)

Protein quantification was carried out using Bradford reagent. 5x Bradford reagent (Roti-Quant) was diluted with ddH_2O to 1x and 200 µl per well were pipetted into a transparent 96-well plate. A calibration of BSA concentrations was performed with each Bradford assay using BSA concentrations between 0.5 to 7 mg/ml (0.5; 1, 1.5, 2, 2.5, 3, 4, 5, 6, 7). The calibration was performed in duplicates while each sample was analyzed in triplicates. After mixing the sample with the reagent, the plate was incubated for 5 min before the absorbance at 595 nm was measured using a plate reader (Tecan). The protein concentration was calculated using the calibration curve.

6.1.10 Agarose gel electrophoresis

Agarose gel electrophoresis was used to determine the size of DNA fragments. For gel preparation 1 % (w/v) agarose was dissolved in 1x TBE buffer by boiling it in the microwave. Afterwards, 0,05 µg/ml Ethidium bromide were added, the gel was cast into a chamber, and a comb was placed inside. Then it was left to solidify for 20 min. 2 µl of DNA were mixed with the loading dye and ddH_2O and loaded onto the gel. For the marker (gene ruler) only 1 µl was taken but otherwise it was prepared the same way. Gel electrophoresis was then performed for 1 h at 50 V. The gel was imaged using the Intas chemo star.

6.1.11 SDS-PAGE

SDS-PAGE gels were cast using the Bio-Rad system. The glass plates were cleaned with 70 % EtOH before use. The gel was then prepared in two steps. First the separation gel was prepared and cast and overlaid with Isopropanol to get a smooth edge between separation- and stacking gel. After the separation gel was cured, the isopropanol was removed and the stacking gel was cast on top. A 10 or 15-well comb was added into the gel and it was left to solidify.

Samples were prepared by adding 4x SDS sample loading buffer and ddH_2O to the sample to a final concentration of 1x SDS sample loading buffer and 10-50 µg of protein. The samples were incubated at 95 °C for 5 min before loading them onto the gel. For the pre-stained molecular weight marker, 3 µl of marker were directly loaded to the gel. The SDS-PAGE was performed in a Bio-Rad chamber (Mini-Protean Tetra) at a constant voltage of 70 V until the samples reached the stacking gel, then the voltage was increased to 120 V.

Afterwards, the gel was either used for western blotting or stained with Coomassie. For Coomassie staining, the gel was incubated with the staining solution for 20-30 min and destained in destaining solution overnight. Images of the gel were taken using the Intas chemo star.

Table 6.3: SDS-PAGE recipe for 1 gel 1.5 mm (Separation gel conc. can be changed, stacking gel conc. Always stayed at 4 %)

Components	Separation gel 12 %	Stacking gel 4 %
ddH_2O	3.32 ml	3 ml
Separation gel buffer	2.50 ml	-
Stacking gel buffer	-	1.25 ml
10 % SDS	50 µl	25 µl
Rotiphorese Gel 30 (37.4:1)	4 ml	0.67 µl
TEMED	20 µl	7 µl
APS (10 %)	76 µl	50 µl

6.1.12 Western Blot (Semi-dry)

For identification and determination of relative abundance of proteins up to 70 kDa, semi-dry western blot was employed. For that, 1x transfer buffer was prepared from a 5x stock provided in the transfer kit following the instructions of the kit. Transfer stacks were soaked in 1x transfer buffer and also the nitrocellulose membrane was incubated in the buffer prior to the assembly. Then one transfer stack was placed at the bottom of the cassette followed by the nitrocellulose membrane. The SDS-PAGE gel was directly transferred and placed on top of the membrane and covered with another transfer stack. Air bubbles were removed from the stack by rolling with a gel roller over the stack. The cassette was then locked and placed in the instrument. Blotting was performed at 1.3 A constant with a voltage up to 25 V for 13 min for 1 mini gel or at 2.5 A constant with a voltage up to 25 V for 13 min for 2 mini gels. After blotting, the membrane was blocked with 5 % milk powder (w/v) in TBS-T for 1 h at RT on the shaker. Once the blocking solution was removed, the primary antibody diluted in 3 % (w/v) milk powder in TBS-T was added to the membrane. The membrane was incubated with the primary antibody on the shaker overnight at 4 °C. The next day, the membrane was washed three times for 10 min with TBS-T before the secondary antibody diluted in 3 % (w/v) milk powder in TBS-T was added to the membrane. The membrane was then incubated with the second antibody on the shaker for 2 h at RT and washed again three times for 10 min with TBS-T prior to imaging. Imaging was performed using the ECL-reagent and the Intas Chemostar to detect chemiluminescence.

6.1.13 ATPase assay

To assess the functionality of purified J-domain proteins, their ability to induce the ATPase activity of Hsc70 was tested with this assay. In a total reaction volume of 160 µl in 1x reaction buffer, 1 µM Hsc70 was mixed with 0.5 µM of the respective J-domain protein and 1 mM ATP. As an autohydrolysis control, ATP was incubated under the same conditions without chaperones. Further controls were ATP with Hsc70 alone and ATP with just the J-domain protein. To all samples ATP was added last, which

marked the beginning of the experiment. The samples were then incubated for 2.5 h at RT. After 2 h, green malachite reaction solution was prepared by mixing the green malachite stock solution with the ammonium molybdate stock solution and ddH_2O in a ratio of 2:1:3. After 20 min of incubation at RT the solution becomes clear and yellow and was ready to use. Once the incubation time was over, each sample was pipetted to a transparent 96-well plate in triplicates by adding 50 µl per well. A phosphate standard was measured in parallel containing KH_2PO_4 in the following concentrations: 0 mM, 5 mM, 10 mM, 20 mM, 40 mM, 80 mM and 160 mM. Then 160 µl of green malachite reaction solution and 20 µl of 34 % sodium citrate were added to each well. Absorbance at 650 nm was measured using the plate reader (Tecan). The concentration of free phosphate was calculated from the equation obtained from the standard after the autohydrolysis background was subtracted. In the end, the values were normalized to the intrinsic ATPase activity of Hsc70 in the absence of a J-domain protein.

6.1.14 Luciferase refolding assay

To assess the ability of the chaperones to refold denatured proteins, the luciferase refolding assay was performed. For that, 15 nM of Luciferase in HMK buffer were either heat denatured by incubating the solution at 45 °C for 15 min or kept native (positive control). Luciferase was diluted to a final concentration of 5 nM in HMK buffer containing 2,5 µM Hsc70, 0,125 µM Apg2, and 2,5 µM J-domain protein as well as 3,5 µM Pyruvate Kinase, 3 mM Phosphoenolpyruvate and 1 mM ATP. Luminescence was measured at different time points to determine the refolding efficiency. For that, 5 µl samples were taken at time 0, 7, 15, 30, 60, 90, and 120 min in triplicates and pipetted into a white 96-well plate containing 50 µl of assay buffer in each well already. 50 µl of 0.25 mM luciferin were added to each well as substrate and luminescence was measured using a plate reader (Tecan) with the settings as followed: No attenuation, an integration time of 1000 ms and settle time of 0 ms. The measured values were normalized on the values of the native luciferase at each time point. Denatured luciferase in the absence of chaperones served as negative control. The values were then depicted as the percentage of luciferase activity recovered over time.

6.1.15 HTT-FRET assay

The FRET assay was employed to monitor Htt aggregation and its suppression by chaperones. Samples were prepared in low binding tubes in 1x reaction buffer to which ATP (5 mM), DTT (10 mM) and the ATP regeneration system consisting of pyruvate kinase (1 µl/50 µl) and phosphoenol pyruvate (3 mM) were added freshly. GST-HttEx1_CyPet and GST-HttEx1_YPet were mixed in an equimolar ratio with a final Htt concentration of 0,375 µM. In general chaperones were added at concentrations of Hsc70 5 µM, J-domain protein 5 µM and Apg2 0,25 µM. For the 2x samples, the J-protein concentration was increased to 10 µM. The reaction was initiated by the addition of PreScission (1,4 µl/ 100 µl), cleaving the GST-tag. All samples were prepared in a final volume of 100 µl. Samples were transferred to a black 384-well plate in triplicates with 30 µl per well. Depicted values are the mean values of triplicates. The plate was covered with foil to prevent evaporation of the samples over time. As controls/background GST-HttEx1_CyPet and GST-HttEx1_Ypet were measured individually and mixed without chaperones. Fluorescence signals were measured every 20 min in three fluorescent channels:

Donor channel: (CyPet): Excitation at 430 nm (20 nm bandwidth), emission at 485 nm (20 nm bandwidth)

Acceptor channel: (YPet): Excitation at 485 nm (20 nm bandwidth), emission at 530 nm (25 nm bandwidth)

FRET cannel: Excitation at 430 nm (20 nm bandwidth), emission at 530 nm (25 nm bandwidth)

The following settings were used for all cannels: gain: 50 (manual), number of flashes: 10, integration time: 20 µs, lag time: 0 µs and settle time: 0 µs. Raw signals were processed by subtracting the blank for each channel measured in empty wells. Then the signals were corrected for donor bleed through (RD) and acceptor background (RA)

$$\mathrm{RD} = \frac{\text{Donor fluorescence in FRET channel}}{\text{Donor fluorescence in donor channel}}$$

$$\mathrm{RA} = \frac{\text{Acceptor fluorescence in FRET cahnnel}}{\text{Acceptor fluorescence in acceptor channel}}$$

Therefore, the sensitized emission was then calculated as followed:

$$\begin{aligned}\mathrm{SE} = {} & \text{sample fluorescence in FRET channel} \\ & - ((\text{sample fluorescence in donor channel} * \mathrm{RD}) \\ & - (\text{sample fluorescence in acceptor channel} * \mathrm{RA}))\end{aligned}$$

The sensitized emission was normalized to the acceptor signal in the acceptor channel and half-life times ($T_{1/2}$) were calculated to compare measurements.

6.1.16 Phase separation

For the phase separation experiments, HTTEx1 construct tagged with either GST or a fluorophore were used. All proteins that were added to the phase separation experiments were in liquid-liquid phase separation buffer. The buffer was exchanged prior to the experiment. To induce phase separation, 10 % (w/v) of Dextran was added to the samples.

Phase separation was mainly analyzed by confocal laser scanning microscopy. For that, microscopy slides were prepared in a way that the cover slip was glued to the glass slide with double sided tape. The glass slides were then coated with BSA. For that, a BSA solution of 30 mg/ml was prepared and 500 µl were pipetted in between the cover slip and glass slide. After 30 min of incubation a RT the BSA solution was removed from the slide and the slide was left to dry.

For imaging, 20 µl of sample were pipetted onto the slide.

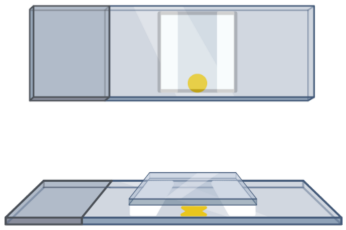

Figure 6.1:**Phase separation slide**

6.1.17 FRAP measurements

Fluorescence Recovery After Photobleaching (FRAP) was employed to investigate the mobility of HTTEx1 in early condensates. For this purpose, a small area inside of a condensate was bleached by using the maximum laser power and 10 iterations on a confocal microscope. The pinhole was adjusted to the size of the condensates to allow bleaching of the whole depth of the condensates. After photobleaching, images were taken with 2 % laser power every 5 s to monitor fluorescence recovery. As a reference, the fluorescence of a non-bleached condensate was measured over time to correct for the general extent of photobleaching due to image acquisition. Additionally, to correct for background fluorescence, a region without condensates was analyzed. For calculation of the fluorescence recovery, the background value was subtracted from all measurements, then the values were corrected for photobleaching by normalization on the reference measurement and finally the recovery was calculated by normalizing to the pre-bleach values of the respective condensate. Multiple condensates (at least three) were bleached and analyzed to acquire technical replicate. For each condition, three independent experiments were performed. All FRAP images were taken at a frame size of 256 x 256 with laser scanning speed of 6 -7 and with the EC Plan-Neofluar 40x/1,3 oil DIC objective (LSM 880 Zeiss).

6.1.18 Turbidity assay

For the turbidity assay, only GST-tagged HttEx1 variants were used. The turbidity assay was performed in liquid-liquid phase separation buffer. For that, the buffer of the proteins was exchanged prior to the experiment. HttEx1 variants were mixed with Dextran to a final protein concentration of 25 µM with 10 % (w/v) Dextran. Directly after the Dextran was added, the samples were pipetted into a transparent 348-well plate. To assess turbidity, the absorbance was measured at 595 nm. As controls, samples without Dextran were prepared. As background, a sample without protein was measured. Measurements were taken in time intervals of 1 min.

6.1.19 CD (circular dichroism) measurement

For CD measurements chloride ions had to be removed from the protein sample. Hence, the protein was dialyzed against 50 mM phosphate buffer pH 7,4 at 4 °C. Afterwards, the protein was ultracentrifuged at 40.000 rpm for 40 min at 4 °C and the protein concentration was determined by Bradford assay. For the measurement, the protein was diluted in phosphate buffer to a final concentration of 0,5 mg/ml. The protein was then handed over to our collaborators (Isabell Grothaus; Universität Bremen) for the CD measurements.

6.1.20 HEK293 cell culture conditions

HEK293 cells were maintained in DMEM High Glucose (4,5 g/l) with L-Glutamine and Sodium Pyruvate supplemented with 10 % fetal calf serum and Penicillin/Streptomycin 100 U/ml both. The cells were kept at 37 °C with 5 % CO_2. Cells were split and transferred to new plates every 2-3 days when 80% coverage was reached.

6.1.21 Transfection of HEK cells

DMEM medium was removed from the cells and cells were washed with DPBS. Then, 500 µl of trypsin (0.25 %) were added per well and the cells were incubated for 2 min at 37 °C to detach the cells from the surface. Afterwards, 1 ml of DMEM + FCS 10 % was added. Cells were transferred into a falcon tube and the cell number per ml was determined by counting the cells in a Neubauer counting chamber. The number of cells that was seeded depended on the downstream application. For imaging, a small round cover slip was placed on the bottom of each well and the wells were seeded with 350.000 cells. While for western blotting 900.000 cells per well were seeded. The next day, when the cells had attached they were transfected. For that, a PEI master mix was prepared by mixing 64 µl of the PEI stock solution (1 mg/ml) with 336 µl of ddH_2O incubating it for 5 min at RT. Then 50 µl of the PEI master mix were mixed with 50 µl of DNA solution containing 2 µg of the respective plasmid or 2 µg of each plasmid for co-transfection in serum free DMEM. The transfection mixture was incubated for 20 min at RT before it was added dropwise to the well. After 48 h, the cells were either harvested or imaged. For siRNA treatment, cells were transfected with jetPRIME according to the manufacturer´s protocol. For transfection, 250.000 cells were seeded and transfected with 1 µg of plasmid and 50 nM final concentration of siRNA (dnajb1 or non-targeting). Cells were harvested or imaged after 32 h.

6.1.22 Imaging of HEK cells

HEK cells were either fixated or imaged directly in the well using cell dishes with a thin glass bottom. For fixation, the coverslip on which the cells had grown was removed from the well and incubated in 4 % formaldehyde solution for 6 min. Then, the coverslip was washed in DPBS and transferred onto a glass slide. For live cell imaging, DMEM buffer was removed and cells were washed with DPBS. DPBS was added to the cells and cells were imaged in the dish. Imaging was performed on a laser scanning confocal microscope (LSM 880, Zeiss) using a Zeiss Plan-Apochromat ×20/0.8 objective.

6.2 *In vivo C. elegans* methods

6.2.1 Maintenance

Nematodes were kept on 60 mm NGM agar plates with a bacterial lawn of *E. coli* OP50 as food source. The nematodes were kept at 20 °C in a dark room. Every four days, 4-8 nematodes (depending on the strain) were passed onto fresh NGM agar plates.

6.2.2 Synchronization

All nematodes were synchronized by egg laying. For that, 10-20 adult gravid nematodes were placed onto fresh NGM plates and left for 4 h at 20 °C. Afterwards, the adults were removed and the plates were left for incubation at 20 °C.

6.2.3 Generation of male nematodes by heat shock

Male nematodes for genetic crossings were generated by heat-shock. For that, five L4 nematodes were placed on a NGM-agar plate which was then incubated at 30 °C in the incubator for 7-8 h. Afterwards, the plates were shifted back to 20 °C. At least three plates were prepared to generate a sufficient number of male nematodes. After 3-5 days (depending on the strain), the plates were screened for male nematodes. Male nematodes were transferred onto fresh plates to which two L4 hermaphrodites of the same strain were added to maintain a male population. From there males were picked for genetic crossings.

6.2.4 Genetic Crossing

To cross two nematode strains, male nematodes were generated for one of the strains. For the genetic crossings, two hermaphrodites in L4 stage from one strain were placed on a plate with 7-10 males from the other strain. Using a 35 mm dish instead of a 60 mm dish can improve mating efficiency. The nematodes were incubated at 20 °C and after 3-5 days, the offspring was checked to determine if the crossing was successful (crossings in this study were confirmed by fluorescence, since all constructs were fluorescently tagged). Nematodes of the F1 generation were placed onto new plates. Of that generation all nematodes which were showing both fluorescent markers were heterozygous for both traits. After 4-5 days the F2 generation was checked for nemtodes carrying both fluorescent markers. Ten nematodes of those were singled out onto fresh plates for self-fertilization. After 4-5 days, the next generation was checked to determine if those nematodes were homozygous for both traits. If none of those nematodes was homozygous for both traits, the nematodes were singled out again and the process was repeated.

6.2.5 Co-localization analysis

To check for subcellular co-localization of two fluorescently tagged proteins, images were taken on the confocal laser scanning microscope. The images for both channels (mScarlett and EYFP) were taken independently to prevent any bleed trough. Images were analyzed in Fiji using the JACoP plugin to calculate the Pearson´s correlation coefficient. For each condition at least 10 nematodes were analyzed.

6.2.6 Fecundity assay

For the fecundity assay, nematodes were synchronized. Then 30 L4 nematodes were placed onto individual 35 mm plates. For the duration of the assay, the nematodes were transferred to new plates every day to separate them from their offspring. The number of eggs/L1 larvae was counted for each nematode every day until they had reached the end of their reproductive phase. If bagging occurred those nematodes were censored from the experiment

6.2.7 Imaging of nematodes

To take images of nematodes, a slide with an agarose pad was prepared to mount the nematodes onto the slide. For that, 3 % (w/v) agarose solution was melted by incubating it at 95 °C in a heating block. 150 µl were pipetted onto a glass slide and directly covered with a second glass slide to create a thin agarose pad. After the agarose solidified the second glass slide was removed and nemtodes were mounted. For that, 20 µl of 250 mM NaN_3 were pipetted onto the agar pad and then nematodes were picked and placed in the droplet. A coverslip was applied and nematodes could be imaged at the microscope.

6.2.8 Fluorescence life time imaging

Fluorescence life time imaging (FLIM) was performed to assess protein aggregation *in vivo*. Ten nematodes were mounted onto a slide. Fluorescent lifetime was measured by time correlated single photon counting (TCSPC). For that, the confocal laser scanning microscope LSM880 from Zeiss with the FLIM set up of PicoQuant, consisting of a PDL 828 Sepia laser unit, a laser combining unit and a PMA Hybrid single photon counting module was used. Since HttExon1Q_n was tagged with mScarlet, the fluorophore was excited at a wavelength of 560 nm by a pulsed laser at 40 MHz pulse rate and the emission was measured in a range from 575-620 nm. To assess HttExon1Q_n aggregation in the neurons, the head region of the nematodes was imaged. The measurement was performed until a photon count of 3000 in the

brightest pixel was reached. Measurements were performed with a laser intensity of 60 %. The pinhole was completely open. All FLIM measurements were taken with the Plan-Apochromat 40x/1,4 Oil DIC M27 objective.

An IRF was measured to correct for light scattering at the glass surface. FLIM data was analyzed using the FlimFit software. An integration value of 40 was used. For fitting of the mono exponential decay data points from 1500 ps to 4000 ps were used.

7. References

Alberti, S., Gladfelter, A. and Mittag, T. (2019) 'Considerations and Challenges in Studying Liquid-Liquid Phase Separation and Biomolecular Condensates', *Cell*, 176(3), pp. 419–434. Available at: https://doi.org/10.1016/j.cell.2018.12.035.

Altun, Z.F., H., D.H. (2023) 'Handbook of C. elegans Anatomy.' WormAtlas.

Andersen, C.B. *et al.* (2009) 'Branching in Amyloid Fibril Growth', *Biophysical Journal*, 96(4), pp. 1529–1536. Available at: https://doi.org/10.1016/j.bpj.2008.11.024.

Andresen, J.M. *et al.* (2007) 'The Relationship Between CAG Repeat Length and Age of Onset Differs for Huntington's Disease Patients with Juvenile Onset or Adult Onset: The Correlation Between HD Age of Onset and CAG Repeat Length Appears Segmental', *Annals of Human Genetics*, 71(3), pp. 295–301. Available at: https://doi.org/10.1111/j.1469-1809.2006.00335.x.

Anfinsen, C.B. (1973) 'Principles that Govern the Folding of Protein Chains', *Science*, 181(4096), pp. 223–230. Available at: https://doi.org/10.1126/science.181.4096.223.

Arndt, J.R., Chaibva, M. and Legleiter, J. (2015) 'The emerging role of the first 17 amino acids of huntingtin in Huntington's disease', *Biomolecular Concepts*, 6(1), pp. 33–46. Available at: https://doi.org/10.1515/bmc-2015-0001.

Ast, A. *et al.* (2018) 'mHTT Seeding Activity: A Marker of Disease Progression and Neurotoxicity in Models of Huntington's Disease', *Molecular Cell*, 71(5), pp. 675-688.e6. Available at: https://doi.org/10.1016/j.molcel.2018.07.032.

Atwal, R.S. *et al.* (2007) 'Huntingtin has a membrane association signal that can modulate huntingtin aggregation, nuclear entry and toxicity', *Human Molecular Genetics*, 16(21), pp. 2600–2615. Available at: https://doi.org/10.1093/hmg/ddm217.

Ayala Mariscal, S.M. *et al.* (2022) 'Identification of a HTT-specific binding motif in DNAJB1 essential for suppression and disaggregation of HTT', *Nature Communications*, 13(1), p. 4692. Available at: https://doi.org/10.1038/s41467-022-32370-5.

Ayala Mariscal, S.M. and Kirstein, J. (2021) 'J-domain proteins interaction with neurodegenerative disease-related proteins', *Experimental Cell Research*, 399(2), p. 112491. Available at: https://doi.org/10.1016/j.yexcr.2021.112491.

Baias, M. *et al.* (2017) 'Structure and Dynamics of the Huntingtin Exon-1 N-Terminus: A Solution NMR Perspective', *Journal of the American Chemical Society*, 139(3), pp. 1168–1176. Available at: https://doi.org/10.1021/jacs.6b10893.

Balch, W.E. *et al.* (2008) 'Adapting Proteostasis for Disease Intervention', *Science*, 319(5865), pp. 916–919. Available at: https://doi.org/10.1126/science.1141448.

Balchin, D., Hayer-Hartl, M. and Hartl, F.U. (2016) 'In vivo aspects of protein folding and quality control', *Science*, 353(6294), p. aac4354. Available at: https://doi.org/10.1126/science.aac4354.

Banani, S.F. *et al.* (2017) 'Biomolecular condensates: organizers of cellular biochemistry', *Nature Reviews Molecular Cell Biology*, 18(5), pp. 285–298. Available at: https://doi.org/10.1038/nrm.2017.7.

Becker, W. (2012) 'Fluorescence lifetime imaging - techniques and applications: FLUORESCENCE LIFETIME IMAGING', *Journal of Microscopy*, 247(2), pp. 119–136. Available at: https://doi.org/10.1111/j.1365-2818.2012.03618.x.

Bhattacharyya, A. *et al.* (2006) 'Oligoproline Effects on Polyglutamine Conformation and Aggregation', *Journal of Molecular Biology*, 355(3), pp. 524–535. Available at: https://doi.org/10.1016/j.jmb.2005.10.053.

Bhide, P.G. *et al.* (1996) 'Expression of Normal and Mutant Huntingtin in the Developing Brain', *The Journal of Neuroscience*, 16(17), pp. 5523–5535. Available at: https://doi.org/10.1523/JNEUROSCI.16-17-05523.1996.

Bolte, S. and Cordelières, F.P. (2006) 'A guided tour into subcellular colocalization analysis in light microscopy', *Journal of Microscopy*, 224(3), pp. 213–232. Available at: https://doi.org/10.1111/j.1365-2818.2006.01706.x.

Bousset, L. *et al.* (2013) 'Structural and functional characterization of two alpha-synuclein strains', *Nature Communications*, 4(1), p. 2575. Available at: https://doi.org/10.1038/ncomms3575.

Brehme, M. *et al.* (2014) 'A Chaperome Subnetwork Safeguards Proteostasis in Aging and Neurodegenerative Disease', *Cell Reports*, 9(3), pp. 1135–1150. Available at: https://doi.org/10.1016/j.celrep.2014.09.042.

Brenner, S. (1974) 'THE GENETICS OF *CAENORHABDITIS ELEGANS*', *Genetics*, 77(1), pp. 71–94. Available at: https://doi.org/10.1093/genetics/77.1.71.

Bugg, C.W. *et al.* (2012) 'Structural Features and Domain Organization of Huntingtin Fibrils', *Journal of Biological Chemistry*, 287(38), pp. 31739–31746. Available at: https://doi.org/10.1074/jbc.M112.353839.

Byerly, L., Cassada, R.C. and Russell, R.L. (1976) 'The life cycle of the nematode Caenorhabditis elegans', *Developmental Biology*, 51(1), pp. 23–33. Available at: https://doi.org/10.1016/0012-1606(76)90119-6.

Cattaneo, E., Zuccato, C. and Tartari, M. (2005) 'Normal huntingtin function: an alternative approach to Huntington's disease', *Nature Reviews Neuroscience*, 6(12), pp. 919–930. Available at: https://doi.org/10.1038/nrn1806.

Chen, M. and Wolynes, P.G. (2017) 'Aggregation landscapes of Huntingtin exon 1 protein fragments and the critical repeat length for the onset of Huntington's disease', *Proceedings of the National Academy of Sciences*, 114(17), pp. 4406–4411. Available at: https://doi.org/10.1073/pnas.1702237114.

Cohen, S.I.A. *et al.* (2012) 'From Macroscopic Measurements to Microscopic Mechanisms of Protein Aggregation', *Journal of Molecular Biology*, 421(2–3), pp. 160–171. Available at: https://doi.org/10.1016/j.jmb.2012.02.031.

Cohen, S.I.A. *et al.* (2013) 'Proliferation of amyloid-β42 aggregates occurs through a secondary nucleation mechanism', *Proceedings of the National Academy of Sciences*, 110(24), pp. 9758–9763. Available at: https://doi.org/10.1073/pnas.1218402110.

Craig, E.A. and Marszalek, J. (2017) 'How Do J-Proteins Get Hsp70 to Do So Many Different Things?', *Trends in Biochemical Sciences*, 42(5), pp. 355–368. Available at: https://doi.org/10.1016/j.tibs.2017.02.007.

Crick, S.L. *et al.* (2006) 'Fluorescence correlation spectroscopy shows that monomeric polyglutamine molecules form collapsed structures in aqueous solutions', *Proceedings of the National Academy of Sciences*, 103(45), pp. 16764–16769. Available at: https://doi.org/10.1073/pnas.0608175103.

Crick, S.L. *et al.* (2013) 'Unmasking the roles of N- and C-terminal flanking sequences from exon 1 of huntingtin as modulators of polyglutamine aggregation', *Proceedings of the National Academy of Sciences*, 110(50), pp. 20075–20080. Available at: https://doi.org/10.1073/pnas.1320626110.

Dahlgren, P.R. *et al.* (2005) 'Atomic force microscopy analysis of the Huntington protein nanofibril formation', *Nanomedicine: Nanotechnology, Biology and Medicine*, 1(1), pp. 52–57. Available at: https://doi.org/10.1016/j.nano.2004.11.004.

Darnell, G. *et al.* (2007) 'Flanking Polyproline Sequences Inhibit β-Sheet Structure in Polyglutamine Segments by Inducing PPII-like Helix Structure', *Journal of Molecular Biology*, 374(3), pp. 688–704. Available at: https://doi.org/10.1016/j.jmb.2007.09.023.

Darnell, G.D. *et al.* (2009) 'Mechanism of Cis-Inhibition of PolyQ Fibrillation by PolyP: PPII Oligomers and the Hydrophobic Effect', *Biophysical Journal*, 97(8), pp. 2295–2305. Available at: https://doi.org/10.1016/j.bpj.2009.07.062.

Davis, P. *et al.* (2022) 'WormBase in 2022—data, processes, and tools for analyzing *Caenorhabditis elegans*', *Genetics*. Edited by M. Walhout, 220(4), p. iyac003. Available at: https://doi.org/10.1093/genetics/iyac003.

Dehay, B. and Bertolotti, A. (2006) 'Critical Role of the Proline-rich Region in Huntingtin for Aggregation and Cytotoxicity in Yeast', *Journal of Biological Chemistry*, 281(47), pp. 35608–35615. Available at: https://doi.org/10.1074/jbc.M605558200.

Dragatsis, I., Levine, M.S. and Zeitlin, S. (2000) 'Inactivation of Hdh in the brain and testis results in progressive neurodegeneration and sterility in mice', *Nature Genetics*, 26(3), pp. 300–306. Available at: https://doi.org/10.1038/81593.

Duennwald, M.L. *et al.* (2006) 'Flanking sequences profoundly alter polyglutamine toxicity in yeast', *Proceedings of the National Academy of Sciences*, 103(29), pp. 11045–11050. Available at: https://doi.org/10.1073/pnas.0604547103.

Duim, W.C. *et al.* (2014) 'Super-Resolution Fluorescence of Huntingtin Reveals Growth of Globular Species into Short Fibers and Coexistence of Distinct Aggregates', *ACS Chemical Biology*, 9(12), pp. 2767–2778. Available at: https://doi.org/10.1021/cb500335w.

Dunn, K.W., Kamocka, M.M. and McDonald, J.H. (2011) 'A practical guide to evaluating colocalization in biological microscopy', *American Journal of Physiology-Cell Physiology*, 300(4), pp. C723–C742. Available at: https://doi.org/10.1152/ajpcell.00462.2010.

Duyao, M.P. *et al.* (1995) 'Inactivation of the Mouse Huntington's Disease Gene Homolog *Hdh*', *Science*, 269(5222), pp. 407–410. Available at: https://doi.org/10.1126/science.7618107.

El-Daher, M. *et al.* (2015) 'Huntingtin proteolysis releases non-polyQ fragments that cause toxicity through dynamin 1 dysregulation', *The EMBO Journal*, 34(17), pp. 2255–2271. Available at: https://doi.org/10.15252/embj.201490808.

Ellis, R.J. (2006) 'Molecular chaperones: assisting assembly in addition to folding', *Trends in Biochemical Sciences*, 31(7), pp. 395–401. Available at: https://doi.org/10.1016/j.tibs.2006.05.001.

Esler, W.P. *et al.* (2000) 'Alzheimer's Disease Amyloid Propagation by a Template-Dependent Dock-Lock Mechanism', *Biochemistry*, 39(21), pp. 6288–6295. Available at: https://doi.org/10.1021/bi992933h.

Faber, P.W. *et al.* (1999) 'Polyglutamine-mediated dysfunction and apoptotic death of a *Caenorhabditis elegans* sensory neuron', *Proceedings of the National Academy of Sciences*, 96(1), pp. 179–184. Available at: https://doi.org/10.1073/pnas.96.1.179.

Ferrone, F. (1999) 'Analysis of protein aggregation kinetics', in *Methods in Enzymology*. Elsevier, pp. 256–274. Available at: https://doi.org/10.1016/S0076-6879(99)09019-9.

Flaherty, K.M., DeLuca-Flaherty, C. and McKay, D.B. (1990) 'Three-dimensional structure of the ATPase fragment of a 70K heat-shock cognate protein', *Nature*, 346(6285), pp. 623–628. Available at: https://doi.org/10.1038/346623a0.

Fourie, A.M., Sambrook, J.F. and Gething, M.J. (1994) 'Common and divergent peptide binding specificities of hsp70 molecular chaperones', *The Journal of Biological Chemistry*, 269(48), pp. 30470–30478.

Gallrein, C. *et al.* (2021) 'Novel amyloid-beta pathology C. elegans model reveals distinct neurons as seeds of pathogenicity', *Progress in Neurobiology*, 198, p. 101907. Available at: https://doi.org/10.1016/j.pneurobio.2020.101907.

Gao, X. *et al.* (2015) 'Human Hsp70 Disaggregase Reverses Parkinson's-Linked α-Synuclein Amyloid Fibrils', *Molecular Cell*, 59(5), pp. 781–793. Available at: https://doi.org/10.1016/j.molcel.2015.07.012.

Gath, J. *et al.* (2014) 'Unlike Twins: An NMR Comparison of Two α-Synuclein Polymorphs Featuring Different Toxicity', *PLoS ONE*. Edited by P. Van Der Wel, 9(3), p. e90659. Available at: https://doi.org/10.1371/journal.pone.0090659.

George Huntington (1872) 'George Huntington, M. D. On Chorea'. The Medical and Surgical Reporter: A Weekly Journal 26, 317–321.

Gillam, J.E. and MacPhee, C.E. (2013) 'Modelling amyloid fibril formation kinetics: mechanisms of nucleation and growth', *Journal of Physics: Condensed Matter*, 25(37), p. 373101. Available at: https://doi.org/10.1088/0953-8984/25/37/373101.

Gillis, J. *et al.* (2013) 'The DNAJB6 and DNAJB8 Protein Chaperones Prevent Intracellular Aggregation of Polyglutamine Peptides', *Journal of Biological Chemistry*, 288(24), pp. 17225–17237. Available at: https://doi.org/10.1074/jbc.M112.421685.

Giorgini, F. (2013) 'A flexible polyglutamine hinge opens new doors for understanding huntingtin function', *Proceedings of the National Academy of Sciences*, 110(36), pp. 14516–14517. Available at: https://doi.org/10.1073/pnas.1313668110.

Gipson, T.A. *et al.* (2013) 'Aberrantly spliced *HTT,* a new player in Huntington's disease pathogenesis', *RNA Biology*, 10(11), pp. 1647–1652. Available at: https://doi.org/10.4161/rna.26706.

Goldberg, Y.P. *et al.* (1996) 'Cleavage of huntingtin by apopain, a proapoptotic cysteine protease, is modulated by the polyglutamine tract', *Nature Genetics*, 13(4), pp. 442–449. Available at: https://doi.org/10.1038/ng0896-442.

Greene, M.K., Maskos, K. and Landry, S.J. (1998) 'Role of the J-domain in the cooperation of Hsp40 with Hsp70', *Proceedings of the National Academy of Sciences*, 95(11), pp. 6108–6113. Available at: https://doi.org/10.1073/pnas.95.11.6108.

Gruber, A. *et al.* (2018) 'Molecular and structural architecture of polyQ aggregates in yeast', *Proceedings of the National Academy of Sciences*, 115(15). Available at: https://doi.org/10.1073/pnas.1717978115.

Gu, J. *et al.* (2020) 'Hsp40 proteins phase separate to chaperone the assembly and maintenance of membraneless organelles', *Proceedings of the National Academy of Sciences*, 117(49), pp. 31123–31133. Available at: https://doi.org/10.1073/pnas.2002437117.

Guo, Q. *et al.* (2018) 'The cryo-electron microscopy structure of huntingtin', *Nature*, 555(7694), pp. 117–120. Available at: https://doi.org/10.1038/nature25502.

Hageman, J. and Kampinga, H.H. (2009) 'Computational analysis of the human HSPH/HSPA/DNAJ family and cloning of a human HSPH/HSPA/DNAJ expression library', *Cell Stress and Chaperones*, 14(1), pp. 1–21. Available at: https://doi.org/10.1007/s12192-008-0060-2.

Harding, R.J. and Tong, Y. (2018) ‘Proteostasis in Huntington’s disease: disease mechanisms and therapeutic opportunities’, *Acta Pharmacologica Sinica*, 39(5), pp. 754–769. Available at: https://doi.org/10.1038/aps.2018.11.

Harmon, T.S. *et al.* (2017) ‘Intrinsically disordered linkers determine the interplay between phase separation and gelation in multivalent proteins’, *eLife*. Edited by A.A. Hyman, 6, p. e30294. Available at: https://doi.org/10.7554/eLife.30294.

Hartl, F.U. (1996) ‘Molecular chaperones in cellular protein folding’, *Nature*, 381(6583), pp. 571–580. Available at: https://doi.org/10.1038/381571a0.

Hartl, F.U., Bracher, A. and Hayer-Hartl, M. (2011) ‘Molecular chaperones in protein folding and proteostasis’, *Nature*, 475(7356), pp. 324–332. Available at: https://doi.org/10.1038/nature10317.

Hipp, M.S. *et al.* (2012) ‘Indirect inhibition of 26S proteasome activity in a cellular model of Huntington’s disease’, *Journal of Cell Biology*, 196(5), pp. 573–587. Available at: https://doi.org/10.1083/jcb.201110093.

Hipp, M.S., Kasturi, P. and Hartl, F.U. (2019) ‘The proteostasis network and its decline in ageing’, *Nature Reviews Molecular Cell Biology*, 20(7), pp. 421–435. Available at: https://doi.org/10.1038/s41580-019-0101-y.

Hipp, M.S., Park, S.-H. and Hartl, F.U. (2014) ‘Proteostasis impairment in protein-misfolding and -aggregation diseases’, *Trends in Cell Biology*, 24(9), pp. 506–514. Available at: https://doi.org/10.1016/j.tcb.2014.05.003.

Hughes, A.C. *et al.* (2014) ‘Identification of Novel Alternative Splicing Events in the Huntingtin Gene and Assessment of the Functional Consequences Using Structural Protein Homology Modelling’, *Journal of Molecular Biology*, 426(7), pp. 1428–1438. Available at: https://doi.org/10.1016/j.jmb.2013.12.028.

Isas, J.M., Langen, R. and Siemer, A.B. (2015) ‘Solid-State Nuclear Magnetic Resonance on the Static and Dynamic Domains of Huntingtin Exon-1 Fibrils’, *Biochemistry*, 54(25), pp. 3942–3949. Available at: https://doi.org/10.1021/acs.biochem.5b00281.

Jayaraman, M. *et al.* (2012) ‘Slow Amyloid Nucleation via α-Helix-Rich Oligomeric Intermediates in Short Polyglutamine-Containing Huntingtin Fragments’, *Journal of Molecular Biology*, 415(5), pp. 881–899. Available at: https://doi.org/10.1016/j.jmb.2011.12.010.

Jeon, I. *et al.* (2016) ‘Human-to-mouse prion-like propagation of mutant huntingtin protein’, *Acta Neuropathologica*, 132(4), pp. 577–592. Available at: https://doi.org/10.1007/s00401-016-1582-9.

Jiang, Y., Rossi, P. and Kalodimos, C.G. (2019) ‘Structural basis for client recognition and activity of Hsp40 chaperones’, *Science*, 365(6459), pp. 1313–1319. Available at: https://doi.org/10.1126/science.aax1280.

Johri, A., Chandra, A. and Flint Beal, M. (2013) 'PGC-1α, mitochondrial dysfunction, and Huntington's disease', *Free Radical Biology and Medicine*, 62, pp. 37–46. Available at: https://doi.org/10.1016/j.freeradbiomed.2013.04.016.

Ju, T.-C., Lin, Y.-S. and Chern, Y. (2012) 'Energy dysfunction in Huntington's disease: insights from PGC-1α, AMPK, and CKB', *Cellular and Molecular Life Sciences*, 69(24), pp. 4107–4120. Available at: https://doi.org/10.1007/s00018-012-1025-2.

Kakkar, V. *et al.* (2016) 'The S/T-Rich Motif in the DNAJB6 Chaperone Delays Polyglutamine Aggregation and the Onset of Disease in a Mouse Model', *Molecular Cell*, 62(2), pp. 272–283. Available at: https://doi.org/10.1016/j.molcel.2016.03.017.

Kaminski Schierle, G.S. *et al.* (2011) 'A FRET Sensor for Non-Invasive Imaging of Amyloid Formation in Vivo', *ChemPhysChem*, 12(3), pp. 673–680. Available at: https://doi.org/10.1002/cphc.201000996.

Kampinga, H.H. and Craig, E.A. (2010) 'The Hsp70 chaperone machinery: J-proteins as drivers of functional specificity', *Nature reviews. Molecular cell biology*, 11(8), pp. 579–592. Available at: https://doi.org/10.1038/nrm2941.

Kanaan, N.M. *et al.* (2020) 'Liquid-liquid phase separation induces pathogenic tau conformations in vitro', *Nature Communications*, 11(1), p. 2809. Available at: https://doi.org/10.1038/s41467-020-16580-3.

Kang, H. *et al.* (2017) 'Emerging β-Sheet Rich Conformations in Supercompact Huntingtin Exon-1 Mutant Structures', *Journal of the American Chemical Society*, 139(26), pp. 8820–8827. Available at: https://doi.org/10.1021/jacs.7b00838.

Kar, K. *et al.* (2011) 'Critical nucleus size for disease-related polyglutamine aggregation is repeat-length dependent', *Nature Structural & Molecular Biology*, 18(3), pp. 328–336. Available at: https://doi.org/10.1038/nsmb.1992.

Kaushik, S. and Cuervo, A.M. (2015) 'Proteostasis and aging', *Nature Medicine*, 21(12), pp. 1406–1415. Available at: https://doi.org/10.1038/nm.4001.

Kay, C., Hayden, M.R. and Leavitt, B.R. (2017) 'Epidemiology of Huntington disease', in *Handbook of Clinical Neurology*. Elsevier, pp. 31–46. Available at: https://doi.org/10.1016/B978-0-12-801893-4.00003-1.

Kim, M. *et al.* (1999) 'Mutant Huntingtin Expression in Clonal Striatal Cells: Dissociation of Inclusion Formation and Neuronal Survival by Caspase Inhibition', *The Journal of Neuroscience*, 19(3), pp. 964–973. Available at: https://doi.org/10.1523/JNEUROSCI.19-03-00964.1999.

Kim, M.W. *et al.* (2009) 'Secondary Structure of Huntingtin Amino-Terminal Region', *Structure*, 17(9), pp. 1205–1212. Available at: https://doi.org/10.1016/j.str.2009.08.002.

Kim, Y.E. *et al.* (2013) 'Molecular Chaperone Functions in Protein Folding and Proteostasis', *Annual Review of Biochemistry*, 82(1), pp. 323–355. Available at: https://doi.org/10.1146/annurev-biochem-060208-092442.

Kirstein, J. *et al.* (2009) 'Adapting the machine: adaptor proteins for Hsp100/Clp and AAA+ proteases', *Nature Reviews Microbiology*, 7(8), pp. 589–599. Available at: https://doi.org/10.1038/nrmicro2185.

Kirstein, J. *et al.* (2017) '*In vivo* properties of the disaggregase function of J-proteins and Hsc70 in *Caenorhabditis elegans* stress and aging', *Aging Cell*, 16(6), pp. 1414–1424. Available at: https://doi.org/10.1111/acel.12686.

Kityk, R. *et al.* (2015) 'Pathways of allosteric regulation in Hsp70 chaperones', *Nature Communications*, 6(1), p. 8308. Available at: https://doi.org/10.1038/ncomms9308.

Kityk, R., Kopp, J. and Mayer, M.P. (2018) 'Molecular Mechanism of J-Domain-Triggered ATP Hydrolysis by Hsp70 Chaperones', *Molecular Cell*, 69(2), pp. 227-237.e4. Available at: https://doi.org/10.1016/j.molcel.2017.12.003.

Klaips, C.L., Jayaraj, G.G. and Hartl, F.U. (2018) 'Pathways of cellular proteostasis in aging and disease', *Journal of Cell Biology*, 217(1), pp. 51–63. Available at: https://doi.org/10.1083/jcb.201709072.

Knowles, T.P.J. *et al.* (2009) 'An Analytical Solution to the Kinetics of Breakable Filament Assembly', *Science*, 326(5959), pp. 1533–1537. Available at: https://doi.org/10.1126/science.1178250.

Kodali, R. *et al.* (2010) 'Aβ(1–40) Forms Five Distinct Amyloid Structures whose β-Sheet Contents and Fibril Stabilities Are Correlated', *Journal of Molecular Biology*, 401(3), pp. 503–517. Available at: https://doi.org/10.1016/j.jmb.2010.06.023.

Kokona, B., Rosenthal, Z.P. and Fairman, R. (2014) 'Role of the Coiled-Coil Structural Motif in Polyglutamine Aggregation', *Biochemistry*, 53(43), pp. 6738–6746. Available at: https://doi.org/10.1021/bi500449a.

Krach, F. *et al.* (2022) 'An alternative splicing modulator decreases mutant HTT and improves the molecular fingerprint in Huntington's disease patient neurons', *Nature Communications*, 13(1), p. 6797. Available at: https://doi.org/10.1038/s41467-022-34419-x.

Kumar, D.P. *et al.* (2011) 'The Four Hydrophobic Residues on the Hsp70 Inter-Domain Linker Have Two Distinct Roles', *Journal of Molecular Biology*, 411(5), pp. 1099–1113. Available at: https://doi.org/10.1016/j.jmb.2011.07.001.

Labbadia, J. and Morimoto, Richard I. (2015) 'Repression of the Heat Shock Response Is a Programmed Event at the Onset of Reproduction', *Molecular Cell*, 59(4), pp. 639–650. Available at: https://doi.org/10.1016/j.molcel.2015.06.027.

Labbadia, J. and Morimoto, Richard I (2015) 'The Biology of Proteostasis in Aging and Disease', *Annual Review of Biochemistry*, 84(1), pp. 435–464. Available at: https://doi.org/10.1146/annurev-biochem-060614-033955.

Lai, C.-H. *et al.* (2000) 'Identification of Novel Human Genes Evolutionarily Conserved in *Caenorhabditis elegans* by Comparative Proteomics', *Genome Research*, 10(5), pp. 703–713. Available at: https://doi.org/10.1101/gr.10.5.703.

Laine, R.F. *et al.* (2019) 'Fast Fluorescence Lifetime Imaging Reveals the Aggregation Processes of α-Synuclein and Polyglutamine in Aging *Caenorhabditis elegans*', *ACS Chemical Biology*, 14(7), pp. 1628–1636. Available at: https://doi.org/10.1021/acschembio.9b00354.

Laufen, T. *et al.* (1999) 'Mechanism of regulation of Hsp70 chaperones by DnaJ cochaperones', *Proceedings of the National Academy of Sciences*, 96(10), pp. 5452–5457. Available at: https://doi.org/10.1073/pnas.96.10.5452.

Lee, C.C., Walters, R.H. and Murphy, R.M. (2007) 'Reconsidering the Mechanism of Polyglutamine Peptide Aggregation', *Biochemistry*, 46(44), pp. 12810–12820. Available at: https://doi.org/10.1021/bi700806c.

Lee, J.-M. *et al.* (2012) 'CAG repeat expansion in Huntington disease determines age at onset in a fully dominant fashion', *Neurology*, 78(10), pp. 690–695. Available at: https://doi.org/10.1212/WNL.0b013e318249f683.

Legleiter, J. *et al.* (2010) 'Mutant Huntingtin Fragments Form Oligomers in a Polyglutamine Length-dependent Manner in Vitro and in Vivo', *Journal of Biological Chemistry*, 285(19), pp. 14777–14790. Available at: https://doi.org/10.1074/jbc.M109.093708.

Li, H. *et al.* (2000) 'Amino-terminal fragments of mutant huntingtin show selective accumulation in striatal neurons and synaptic toxicity', *Nature Genetics*, 25(4), pp. 385–389. Available at: https://doi.org/10.1038/78054.

Lin, H.-K. *et al.* (2017) 'Fibril polymorphism affects immobilized non-amyloid flanking domains of huntingtin exon1 rather than its polyglutamine core', *Nature Communications*, 8(1), p. 15462. Available at: https://doi.org/10.1038/ncomms15462.

Liu, J.-P. and Zeitlin, S.O. (2017) 'Is Huntingtin Dispensable in the Adult Brain?', *Journal of Huntington's Disease*, 6(1), pp. 1–17. Available at: https://doi.org/10.3233/JHD-170235.

Lu, J.-X. *et al.* (2013) 'Molecular Structure of β-Amyloid Fibrils in Alzheimer's Disease Brain Tissue', *Cell*, 154(6), pp. 1257–1268. Available at: https://doi.org/10.1016/j.cell.2013.08.035.

Macdonald, M. (1993) 'A novel gene containing a trinucleotide repeat that is expanded and unstable on Huntington's disease chromosomes', *Cell*, 72(6), pp. 971–983. Available at: https://doi.org/10.1016/0092-8674(93)90585-E.

Maiuri, T. *et al.* (2013) 'The huntingtin N17 domain is a multifunctional CRM1 and Ran-dependent nuclear and cilial export signal', *Human Molecular Genetics*, 22(7), pp. 1383–1394. Available at: https://doi.org/10.1093/hmg/dds554.

Mario Isas, J. *et al.* (2021) 'Huntingtin fibrils with different toxicity, structure, and seeding potential can be interconverted', *Nature Communications*, 12(1), p. 4272. Available at: https://doi.org/10.1038/s41467-021-24411-2.

Markaki, M. and Tavernarakis, N. (2010) ‘Modeling human diseases in Caenorhabditis elegans’, *Biotechnology Journal*, 5(12), pp. 1261–1276. Available at: https://doi.org/10.1002/biot.201000183.

Marques Sousa, C. and Humbert, S. (2013) ‘Huntingtin: Here, There, Everywhere!’, *Journal of Huntington’s Disease*, 2(4), pp. 395–403. Available at: https://doi.org/10.3233/JHD-130082.

Martin, E.W. and Mittag, T. (2018) ‘Relationship of Sequence and Phase Separation in Protein Low-Complexity Regions’, *Biochemistry*, 57(17), pp. 2478–2487. Available at: https://doi.org/10.1021/acs.biochem.8b00008.

Mayer, M.P. (2013) ‘Hsp70 chaperone dynamics and molecular mechanism’, *Trends in Biochemical Sciences*, 38(10), pp. 507–514. Available at: https://doi.org/10.1016/j.tibs.2013.08.001.

Mayer, M.P. and Gierasch, L.M. (2019) ‘Recent advances in the structural and mechanistic aspects of Hsp70 molecular chaperones’, *Journal of Biological Chemistry*, 294(6), pp. 2085–2097. Available at: https://doi.org/10.1074/jbc.REV118.002810.

McKinstry, S.U. *et al.* (2014) ‘Huntingtin Is Required for Normal Excitatory Synapse Development in Cortical and Striatal Circuits’, *Journal of Neuroscience*, 34(28), pp. 9455–9472. Available at: https://doi.org/10.1523/JNEUROSCI.4699-13.2014.

Meisl, G. *et al.* (2016) ‘Molecular mechanisms of protein aggregation from global fitting of kinetic models’, *Nature Protocols*, 11(2), pp. 252–272. Available at: https://doi.org/10.1038/nprot.2016.010.

Michels, A.A. *et al.* (1999) ‘Heat Shock Protein (Hsp) 40 Mutants Inhibit Hsp70 in Mammalian Cells’, *Journal of Biological Chemistry*, 274(51), pp. 36757–36763. Available at: https://doi.org/10.1074/jbc.274.51.36757.

Miller, J., Rutenber, E. and Muchowski, P.J. (2009) ‘Polyglutamine Dances the Conformational Cha-Cha-Cha’, *Structure*, 17(9), pp. 1151–1153. Available at: https://doi.org/10.1016/j.str.2009.08.004.

Min, J.-N. *et al.* (2008) ‘CHIP Deficiency Decreases Longevity, with Accelerated Aging Phenotypes Accompanied by Altered Protein Quality Control’, *Molecular and Cellular Biology*, 28(12), pp. 4018–4025. Available at: https://doi.org/10.1128/MCB.00296-08.

Mishra, R. *et al.* (2012) ‘Inhibiting the Nucleation of Amyloid Structure in a Huntingtin Fragment by Targeting α-Helix-Rich Oligomeric Intermediates’, *Journal of Molecular Biology*, 415(5), pp. 900–917. Available at: https://doi.org/10.1016/j.jmb.2011.12.011.

Mogk, A. (1999) ‘Identification of thermolabile Escherichia coli proteins: prevention and reversion of aggregation by DnaK and ClpB’, *The EMBO Journal*, 18(24), pp. 6934–6949. Available at: https://doi.org/10.1093/emboj/18.24.6934.

Monsellier, E. *et al.* (2015) ‘Molecular Interaction between the Chaperone Hsc70 and the N-terminal Flank of Huntingtin Exon 1 Modulates Aggregation’, *Journal of*

Biological Chemistry, 290(5), pp. 2560–2576. Available at: https://doi.org/10.1074/jbc.M114.603332.

Morley, J.F. *et al.* (2002) 'The threshold for polyglutamine-expansion protein aggregation and cellular toxicity is dynamic and influenced by aging in *Caenorhabditis elegans*', *Proceedings of the National Academy of Sciences*, 99(16), pp. 10417–10422. Available at: https://doi.org/10.1073/pnas.152161099.

Morris, A.M., Watzky, M.A. and Finke, R.G. (2009) 'Protein aggregation kinetics, mechanism, and curve-fitting: A review of the literature', *Biochimica et Biophysica Acta (BBA) - Proteins and Proteomics*, 1794(3), pp. 375–397. Available at: https://doi.org/10.1016/j.bbapap.2008.10.016.

Nachman, E. *et al.* (2020) 'Disassembly of Tau fibrils by the human Hsp70 disaggregation machinery generates small seeding-competent species', *Journal of Biological Chemistry*, 295(28), pp. 9676–9690. Available at: https://doi.org/10.1074/jbc.RA120.013478.

Nasir, J. *et al.* (1995) 'Targeted disruption of the Huntington's disease gene results in embryonic lethality and behavioral and morphological changes in heterozygotes', *Cell*, 81(5), pp. 811–823. Available at: https://doi.org/10.1016/0092-8674(95)90542-1.

Nekooki-Machida, Y. *et al.* (2009) 'Distinct conformations of in vitro and in vivo amyloids of huntingtin-exon1 show different cytotoxicity', *Proceedings of the National Academy of Sciences*, 106(24), pp. 9679–9684. Available at: https://doi.org/10.1073/pnas.0812083106.

Neueder, A. *et al.* (2017) 'The pathogenic exon 1 HTT protein is produced by incomplete splicing in Huntington's disease patients', *Scientific Reports*, 7(1), p. 1307. Available at: https://doi.org/10.1038/s41598-017-01510-z.

Nillegoda, N.B. *et al.* (2015) 'Crucial HSP70 co-chaperone complex unlocks metazoan protein disaggregation', *Nature*, 524(7564), pp. 247–251. Available at: https://doi.org/10.1038/nature14884.

Nillegoda, N.B. *et al.* (2017) 'Evolution of an intricate J-protein network driving protein disaggregation in eukaryotes', *eLife*, 6, p. e24560. Available at: https://doi.org/10.7554/eLife.24560.

Nithianantharajah, J. and Hannan, A.J. (2013) 'Dysregulation of synaptic proteins, dendritic spine abnormalities and pathological plasticity of synapses as experience-dependent mediators of cognitive and psychiatric symptoms in Huntington's disease', *Neuroscience*, 251, pp. 66–74. Available at: https://doi.org/10.1016/j.neuroscience.2012.05.043.

Nussbaum, R.L. and Ellis, C.E. (2003) 'Alzheimer's Disease and Parkinson's Disease', *New England Journal of Medicine*. Edited by A.E. Guttmacher and F.S. Collins, 348(14), pp. 1356–1364. Available at: https://doi.org/10.1056/NEJM2003ra020003.

Palidwor, G.A. *et al.* (2009) 'Detection of Alpha-Rod Protein Repeats Using a Neural Network and Application to Huntingtin', *PLoS Computational Biology*. Edited by P.E. Bourne, 5(3), p. e1000304. Available at: https://doi.org/10.1371/journal.pcbi.1000304.

Pandey, N.K. *et al.* (2018) 'The 17-residue-long N terminus in huntingtin controls stepwise aggregation in solution and on membranes via different mechanisms', *Journal of Biological Chemistry*, 293(7), pp. 2597–2605. Available at: https://doi.org/10.1074/jbc.M117.813667.

Papsdorf, K., Sacherl, J. and Richter, K. (2014) 'The Balanced Regulation of Hsc70 by DNJ-13 and UNC-23 Is Required for Muscle Functionality', *The Journal of Biological Chemistry*, 289(36), pp. 25250–25261. Available at: https://doi.org/10.1074/jbc.M114.565234.

Parsell, D.A. *et al.* (1994) 'Protein disaggregation mediated by heat-shock protein Hspl04', *Nature*, 372(6505), pp. 475–478. Available at: https://doi.org/10.1038/372475a0.

Patel, A. *et al.* (2015) 'A Liquid-to-Solid Phase Transition of the ALS Protein FUS Accelerated by Disease Mutation', *Cell*, 162(5), pp. 1066–1077. Available at: https://doi.org/10.1016/j.cell.2015.07.047.

Pearce, M.M.P. *et al.* (2015) 'Prion-like transmission of neuronal huntingtin aggregates to phagocytic glia in the Drosophila brain', *Nature Communications*, 6(1), p. 6768. Available at: https://doi.org/10.1038/ncomms7768.

Pecho-Vrieseling, E. *et al.* (2014) 'Transneuronal propagation of mutant huntingtin contributes to non–cell autonomous pathology in neurons', *Nature Neuroscience*, 17(8), pp. 1064–1072. Available at: https://doi.org/10.1038/nn.3761.

Peskett, T.R. *et al.* (2018) 'A Liquid to Solid Phase Transition Underlying Pathological Huntingtin Exon1 Aggregation', *Molecular Cell*, 70(4), pp. 588-601.e6. Available at: https://doi.org/10.1016/j.molcel.2018.04.007.

Pieri, L. *et al.* (2012) 'Fibrillar α-Synuclein and Huntingtin Exon 1 Assemblies Are Toxic to the Cells', *Biophysical Journal*, 102(12), pp. 2894–2905. Available at: https://doi.org/10.1016/j.bpj.2012.04.050.

Pigazzini, M.L. *et al.* (2021) 'An Expanded Polyproline Domain Maintains Mutant Huntingtin Soluble in vivo and During Aging', *Frontiers in Molecular Neuroscience*, 14. Available at: https://www.frontiersin.org/articles/10.3389/fnmol.2021.721749 (Accessed: 12 October 2022).

Poirier, M.A. *et al.* (2002) 'Huntingtin Spheroids and Protofibrils as Precursors in Polyglutamine Fibrilization', *Journal of Biological Chemistry*, 277(43), pp. 41032–41037. Available at: https://doi.org/10.1074/jbc.M205809200.

Qian, Y.Q. *et al.* (1996) 'Nuclear Magnetic Resonance Solution Structure of the Human Hsp40 (HDJ-1) J-domain', *Journal of Molecular Biology*, 260(2), pp. 224–235. Available at: https://doi.org/10.1006/jmbi.1996.0394.

Rampelt, H. *et al.* (2012) ‘Metazoan Hsp70 machines use Hsp110 to power protein disaggregation: Disaggregation by animal Hsp110-Hsp70-Hsp40’, *The EMBO Journal*, 31(21), pp. 4221–4235. Available at: https://doi.org/10.1038/emboj.2012.264.

Ratovitski, T. *et al.* (2007) ‘N-Terminal Proteolysis of Full-Length Mutant Huntingtin in an Inducible PC12 Cell Model of Huntington’s Disease’, *Cell Cycle*, 6(23), pp. 2970–2981. Available at: https://doi.org/10.4161/cc.6.23.4992.

Raviol, H. *et al.* (2006) ‘Chaperone network in the yeast cytosol: Hsp110 is revealed as an Hsp70 nucleotide exchange factor’, *The EMBO Journal*, 25(11), pp. 2510–2518. Available at: https://doi.org/10.1038/sj.emboj.7601139.

Ray, S. *et al.* (2020) ‘α-Synuclein aggregation nucleates through liquid–liquid phase separation’, *Nature Chemistry*, 12(8), pp. 705–716. Available at: https://doi.org/10.1038/s41557-020-0465-9.

Reddy, P.H. and Shirendeb, U.P. (2012) ‘Mutant huntingtin, abnormal mitochondrial dynamics, defective axonal transport of mitochondria, and selective synaptic degeneration in Huntington’s disease’, *Biochimica et Biophysica Acta (BBA) - Molecular Basis of Disease*, 1822(2), pp. 101–110. Available at: https://doi.org/10.1016/j.bbadis.2011.10.016.

Riguet, N. *et al.* (2021) ‘Nuclear and cytoplasmic huntingtin inclusions exhibit distinct biochemical composition, interactome and ultrastructural properties’, *Nature Communications*, 12(1), p. 6579. Available at: https://doi.org/10.1038/s41467-021-26684-z.

Rochet, J.-C. and Lansbury, P.T. (2000) ‘Amyloid fibrillogenesis: themes and variations’, *Current Opinion in Structural Biology*, 10(1), pp. 60–68. Available at: https://doi.org/10.1016/S0959-440X(99)00049-4.

Roos, R.A. (2010) ‘Huntington’s disease: a clinical review’, *Orphanet Journal of Rare Diseases*, 5(1), p. 40. Available at: https://doi.org/10.1186/1750-1172-5-40.

Rosenzweig, R. *et al.* (2019) ‘The Hsp70 chaperone network’, *Nature Reviews Molecular Cell Biology*, 20(11), pp. 665–680. Available at: https://doi.org/10.1038/s41580-019-0133-3.

Ross, C.A. and Poirier, M.A. (2004) ‘Protein aggregation and neurodegenerative disease’, *Nature Medicine*, 10(S7), pp. S10–S17. Available at: https://doi.org/10.1038/nm1066.

Ross, C.A. and Tabrizi, S.J. (2011) ‘Huntington’s disease: from molecular pathogenesis to clinical treatment’, *The Lancet Neurology*, 10(1), pp. 83–98. Available at: https://doi.org/10.1016/S1474-4422(10)70245-3.

Rubinsztein, D.C., Mariño, G. and Kroemer, G. (2011) ‘Autophagy and Aging’, *Cell*, 146(5), pp. 682–695. Available at: https://doi.org/10.1016/j.cell.2011.07.030.

Rüdiger, S., Buchberger, A. and Bukau, B. (1997) 'Interaction of Hsp70 chaperones with substrates', *Nature Structural & Molecular Biology*, 4(5), pp. 342–349. Available at: https://doi.org/10.1038/nsb0597-342.

Ruzo, A. *et al.* (2015) 'Discovery of Novel Isoforms of Huntingtin Reveals a New Hominid-Specific Exon', *PLOS ONE*. Edited by S. Humbert, 10(5), p. e0127687. Available at: https://doi.org/10.1371/journal.pone.0127687.

Sahoo, B. *et al.* (2016) 'Folding Landscape of Mutant Huntingtin Exon1: Diffusible Multimers, Oligomers and Fibrils, and No Detectable Monomer', *PLOS ONE*. Edited by D.R. Borchelt, 11(6), p. e0155747. Available at: https://doi.org/10.1371/journal.pone.0155747.

Sala, A.J., Bott, L.C. and Morimoto, R.I. (2017) 'Shaping proteostasis at the cellular, tissue, and organismal level', *Journal of Cell Biology*, 216(5), pp. 1231–1241. Available at: https://doi.org/10.1083/jcb.201612111.

Sathasivam, K. *et al.* (2013) 'Aberrant splicing of *HTT* generates the pathogenic exon 1 protein in Huntington disease', *Proceedings of the National Academy of Sciences*, 110(6), pp. 2366–2370. Available at: https://doi.org/10.1073/pnas.1221891110.

Saudou, F. and Humbert, S. (2016) 'The Biology of Huntingtin', *Neuron*, 89(5), pp. 910–926. Available at: https://doi.org/10.1016/j.neuron.2016.02.003.

Scherzinger, E. *et al.* (1997) 'Huntingtin-Encoded Polyglutamine Expansions Form Amyloid-like Protein Aggregates In Vitro and In Vivo', *Cell*, 90(3), pp. 549–558. Available at: https://doi.org/10.1016/S0092-8674(00)80514-0.

Scherzinger, E. *et al.* (1999) 'Self-assembly of polyglutamine-containing huntingtin fragments into amyloid-like fibrils: Implications for Huntington's disease pathology', *Proceedings of the National Academy of Sciences*, 96(8), pp. 4604–4609. Available at: https://doi.org/10.1073/pnas.96.8.4604.

Schindelin, J. *et al.* (2012) 'Fiji: an open-source platform for biological-image analysis', *Nature Methods*, 9(7), pp. 676–682. Available at: https://doi.org/10.1038/nmeth.2019.

Scior, A. *et al.* (2018) 'Complete suppression of Htt fibrilization and disaggregation of Htt fibrils by a trimeric chaperone complex', *The EMBO Journal*, 37(2), pp. 282–299. Available at: https://doi.org/10.15252/embj.201797212.

Sengupta, P. and Samuel, A.D. (2009) 'Caenorhabditis elegans: a model system for systems neuroscience', *Current Opinion in Neurobiology*, 19(6), pp. 637–643. Available at: https://doi.org/10.1016/j.conb.2009.09.009.

Seredenina, T. and Luthi-Carter, R. (2012) 'What have we learned from gene expression profiles in Huntington's disease?', *Neurobiology of Disease*, 45(1), pp. 83–98. Available at: https://doi.org/10.1016/j.nbd.2011.07.001.

Shen, K. *et al.* (2019) 'Dual Role of Ribosome-Binding Domain of NAC as a Potent Suppressor of Protein Aggregation and Aging-Related Proteinopathies', *Molecular*

Cell, 74(4), pp. 729-741.e7. Available at: https://doi.org/10.1016/j.molcel.2019.03.012.

Shorter, J. (2011) 'The Mammalian Disaggregase Machinery: Hsp110 Synergizes with Hsp70 and Hsp40 to Catalyze Protein Disaggregation and Reactivation in a Cell-Free System', *PLoS ONE*. Edited by K.M. Iijima, 6(10), p. e26319. Available at: https://doi.org/10.1371/journal.pone.0026319.

Sivanandam, V.N. *et al.* (2011) 'The Aggregation-Enhancing Huntingtin N-Terminus Is Helical in Amyloid Fibrils', *Journal of the American Chemical Society*, 133(12), pp. 4558–4566. Available at: https://doi.org/10.1021/ja110715f.

Sulston, J.E. and Horvitz, H.R. (1977) 'Post-embryonic cell lineages of the nematode, Caenorhabditis elegans', *Developmental Biology*, 56(1), pp. 110–156. Available at: https://doi.org/10.1016/0012-1606(77)90158-0.

Sunde, M. and Blake, C. (1997) 'The Structure of Amyloid Fibrils by Electron Microscopy and X-Ray Diffraction', in *Advances in Protein Chemistry*. Elsevier, pp. 123–159. Available at: https://doi.org/10.1016/S0065-3233(08)60320-4.

Taguchi, Y.V. *et al.* (2019) 'Hsp110 mitigates α-synuclein pathology in vivo', *Proceedings of the National Academy of Sciences*, 116(48), pp. 24310–24316. Available at: https://doi.org/10.1073/pnas.1903268116.

Tam, S. *et al.* (2006) 'The chaperonin TRiC controls polyglutamine aggregation and toxicity through subunit-specific interactions', *Nature Cell Biology*, 8(10), pp. 1155–1162. Available at: https://doi.org/10.1038/ncb1477.

Taylor, J.P., Hardy, J. and Fischbeck, K.H. (2002) 'Toxic Proteins in Neurodegenerative Disease', *Science*, 296(5575), pp. 1991–1995. Available at: https://doi.org/10.1126/science.1067122.

Taylor, R.C. and Dillin, A. (2011) 'Aging as an Event of Proteostasis Collapse', *Cold Spring Harbor Perspectives in Biology*, 3(5), pp. a004440–a004440. Available at: https://doi.org/10.1101/cshperspect.a004440.

Thakur, A.K. *et al.* (2009) 'Polyglutamine disruption of the huntingtin exon 1 N terminus triggers a complex aggregation mechanism', *Nature Structural & Molecular Biology*, 16(4), pp. 380–389. Available at: https://doi.org/10.1038/nsmb.1570.

The C. elegans Sequencing Consortium* (1998) 'Genome Sequence of the Nematode *C. elegans* : A Platform for Investigating Biology', *Science*, 282(5396), pp. 2012–2018. Available at: https://doi.org/10.1126/science.282.5396.2012.

Tsai, J. and Douglas, M.G. (1996) 'A Conserved HPD Sequence of the J-domain Is Necessary for YDJ1 Stimulation of Hsp70 ATPase Activity at a Site Distinct from Substrate Binding', *Journal of Biological Chemistry*, 271(16), pp. 9347–9354. Available at: https://doi.org/10.1074/jbc.271.16.9347.

Vale, T.C. and Cardoso, F. (2015) 'Chorea: A Journey through History', *Tremor and Other Hyperkinetic Movements*, 5(0), p. 5. Available at: https://doi.org/10.5334/tohm.275.

Vieweg, S. *et al.* (2016) ‘An Intein-based Strategy for the Production of Tag-free Huntingtin Exon 1 Proteins Enables New Insights into the Polyglutamine Dependence of Httex1 Aggregation and Fibril Formation’, *Journal of Biological Chemistry*, 291(23), pp. 12074–12086. Available at: https://doi.org/10.1074/jbc.M116.713982.

Vieweg, S. *et al.* (2021) ‘The Nt17 Domain and its Helical Conformation Regulate the Aggregation, Cellular Properties and Neurotoxicity of Mutant Huntingtin Exon 1’, *Journal of Molecular Biology*, 433(21), p. 167222. Available at: https://doi.org/10.1016/j.jmb.2021.167222.

Vitalis, A. and Pappu, R.V. (2011) ‘Assessing the contribution of heterogeneous distributions of oligomers to aggregation mechanisms of polyglutamine peptides’, *Biophysical Chemistry*, 159(1), pp. 14–23. Available at: https://doi.org/10.1016/j.bpc.2011.04.006.

Vitet, H., Brandt, V. and Saudou, F. (2020) ‘Traffic signaling: new functions of huntingtin and axonal transport in neurological disease’, *Current Opinion in Neurobiology*, 63, pp. 122–130. Available at: https://doi.org/10.1016/j.conb.2020.04.001.

Wagner, A.S. *et al.* (2018) ‘Self-assembly of Mutant Huntingtin Exon-1 Fragments into Large Complex Fibrillar Structures Involves Nucleated Branching’, *Journal of Molecular Biology*, 430(12), pp. 1725–1744. Available at: https://doi.org/10.1016/j.jmb.2018.03.017.

Walker, F.O. (2007) ‘Huntington’s disease’, *The Lancet*, 369(9557), pp. 218–228. Available at: https://doi.org/10.1016/S0140-6736(07)60111-1.

Wetzel, R. (2012) ‘Physical Chemistry of Polyglutamine: Intriguing Tales of a Monotonous Sequence’, *Journal of Molecular Biology*, 421(4–5), pp. 466–490. Available at: https://doi.org/10.1016/j.jmb.2012.01.030.

Wilson, D.M. *et al.* (2023) ‘Hallmarks of neurodegenerative diseases’, *Cell*, 186(4), pp. 693–714. Available at: https://doi.org/10.1016/j.cell.2022.12.032.

Wolff, S., Weissman, J.S. and Dillin, A. (2014) ‘Differential Scales of Protein Quality Control’, *Cell*, 157(1), pp. 52–64. Available at: https://doi.org/10.1016/j.cell.2014.03.007.

Xue, W.-F., Homans, S.W. and Radford, S.E. (2008) ‘Systematic analysis of nucleation-dependent polymerization reveals new insights into the mechanism of amyloid self-assembly’, *Proceedings of the National Academy of Sciences*, 105(26), pp. 8926–8931. Available at: https://doi.org/10.1073/pnas.0711664105.

Zhang, L. *et al.* (2017) ‘Molecular Mechanism of Stabilizing the Helical Structure of Huntingtin N17 in a Micellar Environment’, *The Journal of Physical Chemistry B*, 121(18), pp. 4713–4721. Available at: https://doi.org/10.1021/acs.jpcb.7b01476.

Zhou, H. *et al.* (2003) ‘Huntingtin forms toxic NH2-terminal fragment complexes that are promoted by the age-dependent decrease in proteasome activity’, *The Journal of*

Cell Biology, 163(1), pp. 109–118. Available at: https://doi.org/10.1083/jcb.200306038.

Zuccato, C., Valenza, M. and Cattaneo, E. (2010) 'Molecular Mechanisms and Potential Therapeutical Targets in Huntington's Disease', *Physiological Reviews*, 90(3), pp. 905–981. Available at: https://doi.org/10.1152/physrev.00041.2009.

8. List of tables and figures

Introduction:

Results:

9. List of abbreviations

ADP	Adenosine diphosphate
APS	Ammoniumperoxodisulfat
ATP	Adenosine triphosphate
BAG	Bcl-2 associated anthanogene
BSA	Bovine serum albumin
°C	Degree Celsius
CD	Circular dichroism
C. elegans	*Caenorhabditis elegans*
CTD	C-terminal domain
DD	Dimerization domain
DMEM	Dulbecco's Modified Eagle's Medium
DNA	Deoxyribonucleic acid
DPBS	Dulbecco's Balanced Salt Solution
DTT	Dithiothreitol
ECL	enhanced chemiluminescence
E. coli	*Escherichia coli*
EDTA	Ethylenediaminetetraacetic acid
EGFP	Enhanced green fluorescent protein
FCS	Fetal calf serum
FLIM	Fluorescence-lifetime imaging microscopy
FRAP	fluorescence recovery after photobleaching
FRET	Förster resonance energy transfer
Fw	Forward
g (µg, mg)	gram (microgram, milligram)
GFP	Green fluorescent protein
GST	Glutathione-S-transferase
h	Hour

HD	Hintington´s disease
HEK	Human Embryonic Kidney
HEPES	4-(2hydroxyethyl)-1-piperazineethanesulfonic acid
HTT	Huntingtin
HTTEx1	Huntingtin Exon1
hsp	Heat shock protein (gene), protein: HSP
IPTG	Isopropyl b-D-1-thiogalactopyranoside
IRES	Internal ribosome entry site
kb	Kilobase
kDa	Kilodalton
l, (µl, ml)	Liter (microliter, milliliter)
LB	Luria broth
LLPS	Liquid-liquid phase separation
L1 – L4	Nematode larval stages 1 to 4
M (pM, nM, µM, mM)	Molar (picomolar, nanomolar, micromolar, millimolar)
MD	Molecular dynamics
MWCO	Molecular weight cut-off
NBM	Nucleotide binding domain
NEF	Nucleotide exchange factor
NGM	Nematode growth media
n.s.	Non significant
PBS	Phosphate buffered saline
PCR	Polymerase chain reaction
PEI	Polyethylenimin
PMSF	Phenylmethylsulfonyl fluoride
PPII	Poly-L-proline type II

PRD	Proline rich domain
PVDF	Polyvinylidene fluoride
rgef-1	Rap Guanine nucleotide Exchange Factor homolog (gene)
RA	acceptor background (RA)
RD	donor bleed through (RD)
RNA	Ribonucleic acid
rpm	Revolutions per minute
RT	Room temperature (approx. 20°C)
s / sec	second
SD	Standard diviation
SDS	Sodium dodecyl sulphate
SDS-PAGE	SDS-polyacrylamide gel electrophoresis
SE	Sensitized emission
siRNA	Small interfering RNA
TBS-(T)	Tris buffered saline (with Tween 20)
TEM	Transmission Electron Microscopy
TEMED	T etramethylethylenediamine
Tm	Melting temperature
Tris	Tris(hydroxymethyl)aminomethane
$T_{1/2}$	Half-life time
UTR	Untranslated region
V	Volt
v/v	Volume per volume
WB	Western blot
wt	Wild type
w/v	Weight per volume
YFP	yellow fluorescent protein

10. Declaration

11. Acknowledgement

First I would like to thank my supervisor Prof. Dr. Janine Kirstein for giving me the opportunity to work as a PhD student in her lab and for her support and guidance during that time. Also, I would like to thank her for giving me the opportunity to make new experiences by supporting research stays in the lab of Dr. Jakob J. Metzger in Berlin and Prof. Dr. Stefan Rüdiger in Utrecht as well as attending an international conference.

I would also like to thank Prof. Dr. Olivia Masseck and Prof. Dr. Mark Hipp for accepting to review this work.

Furthermore, I would like to thank the working group of Prof. Dr. Lucio Colombi Ciacchi for collaborating with us and especially Susan Köppen and Isabell Louise Grothaus from his group who performed all the *in silico* analysis presented in this thesis.

A big thanks also to all the members of the Kirstein lab, who were always supporting me by discussing my experiments and results as well as creating a great work environment. Special thanks to Merve Özel who I worked closely together with and to Dr. Sara Ayala Mariscal who in the beginning of my PhD taught me a lot of methods and always offered advice regarding my experiments.

Finally, I would like to thank my family especially my parents and siblings for supporting my choice to study biology as well as my boyfriend Nils Clamor and my friends Shruti Naik and Johanna Heinz.

Thank you.